MEASURING GALACTIC CHEMICAL ABUNDANCE TRENDS IN OPEN AND GLOBULAR CLUSTERS USING SDSS/APOGEE

by

NATALIE MYERS

Bachelor of Science, 2020
University of St.Thomas
St.Paul, MN

Submitted to the Graduate Faculty of the
College of Science and Engineering
Texas Christian University
in partial fulfillment of the requirements
for the degree of

Master of Science

December 2022

MEASURING GALACTIC CHEMICAL ABUNDANCE TRENDS IN OPEN AND GLOBULAR CLUSTERS USING SDSS/APOGEE

by

Natalie Myers

Dissertation Approved:

Peter M. Frinchaboy III

Kat Barger

Mia Bovill

Richard Bonde

For The College of Science and Engineering

ACKNOWLEDGEMENTS

I would like to acknowledge support for this research from the National Science Foundation (AST-1715662).

Funding for the Sloan Digital Sky Survey IV has been provided by the Alfred P. Sloan Foundation, the U.S. Department of Energy Office of Science, and the Participating Institutions. SDSS-IV acknowledges support and resources from the Center for High-Performance Computing at the University of Utah. The SDSS web site is www.sdss.org.

SDSS-IV is managed by the Astrophysical Research Consortium for the Participating Institutions of the SDSS Collaboration including the Brazilian Participation Group, the Carnegie Institution for Science, Carnegie Mellon University, the Chilean Participation Group, the French Participation Group, Harvard-Smithsonian Center for Astrophysics, Instituto de Astrofísica de Canarias, The Johns Hopkins University, Kavli Institute for the Physics and Mathematics of the Universe (IPMU)/University of Tokyo, Lawrence Berkeley National Laboratory, Leibniz Institut für Astrophysik Potsdam (AIP), Max-Planck-Institut für Astronomie (MPIA Heidelberg), Max- Planck-Institut für Astrophysik (MPA Garching), Max-Planck- Institut für Extraterrestrische Physik (MPE), National Astronomical Observatories of China, New Mexico State University, New York University, University of Notre Dame, Observatário Nacional/MCTI, The Ohio State University, Pennsylvania State University, Shanghai Astronomical Observatory, United Kingdom Participation Group, Universidad Nacional Autónoma de México, University of Arizona, University of Colorado Boulder, University of Oxford, University of Portsmouth, University of Utah, University of Virginia, University of Washington, University of Wisconsin, Vanderbilt University, and Yale University.

Contents

List of Common Acronyms and Terms in Astronomy **vii**

1 Introduction **1**
1.1 The Milky Way . . . 2
1.1.1 Milky Way Structure . . . 2
1.1.2 Galactic Gradients and Chemical Enrichment . . . 3
1.2 Star Clusters . . . 4
1.3 Stellar Spectroscopy and Stellar parameters . . . 6
1.4 Using Star Clusters to Map Chemical Gradients within the Milky Way . 8
1.4.1 The LAMOST Survey . . . 9
1.4.2 The HERMES/GALAH Survey . . . 10
1.4.3 The Gaia-ESO Survey . . . 10
1.4.4 The Open Cluster Study in Netopil et al. (2022) . . . 11
1.4.5 The OCCASO Survey . . . 11
1.4.6 The OCCAM Survey . . . 12

2 Data **14**
2.1 SDSS/APOGEE DR17 . . . 15
2.1.1 Pipeline Changes from APOGEE DR16 to DR17 . . . 18
2.2 Gaia EDR3 . . . 18
2.2.1 Pipeline Changes from Gaia DR2 to EDR3 . . . 19

3 Methods **20**
3.1 Methodology Changes from Donor et al. (2020) . . . 24
3.2 Computing Guiding Center Radii R_{guide} . . . 25
3.3 Membership Comparison to Cantat-Gaudin et al. (2018) . . . 26
3.4 Methodology Changes for Globular Clusters . . . 29

4 Open Cluster Chemical Abundance and Mapping Survey **31**
4.1 The OCCAM DR17 Sample . . . 32
4.1.1 Data Access - SDSS Value Added Catalog . . . 36
4.2 Results . . . 38
4.2.1 The Galactic Metallicity Gradient . . . 38
4.2.2 Galactic Trends for Other Elements . . . 41
4.2.3 The Evolution of Galactic Abundance Gradients . . . 46

4.3 Discussion 50
4.3.1 Comparison to OCCAM-IV sample 50
4.3.2 Comparison to other surveys 52
4.3.3 Comparison of Galactic Abundance Trends 53
4.3.4 Evolution of Galactic Abundance Gradients 58

5 APOGEE Globular Clusters **63**
5.1 The APOGEE Globular Cluster Sample 64

6 Conclusions and Future Work **67**
6.1 The Milky Way Disk Abundance Gradients 68
6.2 Future Work 70

A The OCCAM DR17 Open Cluster Sample **71**

B The APOGEE DR17 Globular Cluster Sample **86**

Vita

Abstract

List of Figures

2.1 APOGEE Spectrum 17

3.1 Old vs New data - Color Magnitude Diagrams 21
3.2 Testing OCCAM Quality 26

4.1 Cluster Sample in the Galactic Plane 33
4.2 Metallicity vs. Radius 38
4.3 Alpha elements vs Radius 42
4.4 Iron Peak Elements vs Radius 44
4.5 Odd-Z elements vs Radius 45
4.6 Cerium vs Radius 46
4.7 Age Bins for Iron 47
4.8 Age Bins Other Elements 49
4.9 Comparing APOGEE metallicity Between DR17 and DR16 52
4.10 Comparing APOGEE Abundances for DR17 vs DR16 54
4.11 Compare to other works 59
4.12 Comparing Against Models 61

5.1 Globular Cluster Metallicity Gradient 66

List of Tables

4.1 Cluster Parameters - High Quality Sample 34
4.2 Cluster Chemistry - High Quality Sample 35
4.3 OCCAM Value Added Catalog 37
4.4 Metallicity Gradients 40
4.5 Abundance Gradients 43

A.1 Open Cluster Parameters - High Quality Sample 72
A.2 Open Cluster Chemistry - High Quality Sample 77

B.1 Globular Cluster Parameters - High Quality Sample 87
B.2 Globular Cluster Chemistry - High Quality Sample 90

List of Acronyms and Terms

- Metals – All elements heavier than hydrogen and helium
- Metallicity – The mass fraction of metals in a star with respect to hydrogen
- [A/B] – Standard notation for an abundance ratio in $\log_{10}$ solar units, where N_A and N_B represent the number densities of elements A and B
  - [Fe/H] – Often used as a proxy for metallicity in stellar spectroscopic studies
- dex – Decimal exponent (deprecated)
  - Unit used for abundance value (e.g. [Fe/H] = 0.06 dex)
- Å – Angstrom; 10^{-10} m
- λ – Wavelength, usually in Å
- R – spectral resolution, $\lambda/\Delta\lambda$
- Gyr – Gigayear; 10^9 years
- Myr – Megayear; 10^6 years
- ly – 1 lightyear = 9.46 x 10^{12} km
- kpc – 1000 parsecs; 1 parsec (pc) = 3.262 ly
- Main Sequence star – Star fusing hydrogen (H) to helium (He) in its core
- 2MASS – Two Micron All Sky Survey
- SDSS – Sloan Digital Sky Survey
- APOGEE – Apache Point Observatory Galactic Evolution Experiment
- LAMOST – Large Sky Area Multi-Object Fiber Spectroscopic Telescope
- GALAH – Galactic Archaeology with HERMES
- Gaia – Global Astrometric Interferometer for Astrophysics

- ESO – European Southern Observatory
- OCCASO - Open Cluster Chemical Abundances from Spanish Observatories
- OCCAM - Open Cluster Chemical Abundance and Mapping survey
- ASPCAP – The APOGEE Stellar Parameters and Chemical Abundances Pipeline
- m_v or V – Apparent magnitude (or brightness) of a star in the visual band
- M_v – Absolute magnitude in the visual band, or intrinsic brightness of a star as if it were at a distance of 10 pc (parsecs)
- J, K_s – The near-infrared magnitudes taken from APOGEE
- $J - K_s$ – Difference between magnitudes, also known as the color index

Chapter 1

Introduction

1.1 The Milky Way

1.1.1 Milky Way Structure

Our insider-perspective of our home Galaxy, the Milky Way, makes it difficult to observe its overall structure. However, from observations of other galaxies and the copious amounts of data from various works, including H I surveys (e.g., Burton 1976), the *Spizter*/GLIMPSE survey (Benjamin et al. 2003), and the high-precision *Gaia* survey (Gaia Collaboration et al. 2016), we have been able to form a tentative picture of the morphology of the Milky Way. The Milky Way consists of three major parts: the Disk, the Bulge/Bar, and the Halo. The disk of the Milky Way refers to the flat plane of stars, gas, and dust, which spans roughly 25 kpc from its center (for reference, the Sun is located at roughly 8 kpc from the Galactic center (Gravity Collaboration et al. 2021)) and can be further split into the thin and thick disks. The thin disk includes stars which are less than $\simeq$ 350 pc above the plane of the Milky Way, tends to include cooler gas, and is where the majority of the star formation in the Galaxy is located. The thick disk, however, extends out to $\simeq$ 1000 pc above the Milky Way's plane and tends to include hotter gas and older stars (Binney & Merrifield 1998). The bulge of the Milky Way contains some of the older stars and is found near its center, as well as a bar. The bar is a dense region of stars, gas, and dust, which can have orbits that differ from the orbits in the disk. Due to the large amount of gas and dust in this region, it is subject to high extinction, and therefore requires infrared (IR)-based data to probe. Finally, the Halo of the Milky Way includes the high-velocity stars and gas which extend beyond the disk

of the Galaxy. Material which is ejected out of the Milky Way's plane, or objects which have been accreted throughout the Milky Way's life span, are located here.

1.1.2 Galactic Gradients and Chemical Enrichment

As a galaxy evolves it is subjected to a cycle of star formation and stellar deaths. Gas within the galaxy condenses and forms stars, these stars live on the main sequence until they eventually exhaust their supply of hydrogen, they turnoff the main sequence and, after some amount time (dependent on the initial mass of the star), they expel their gas into the surrounding medium through processes such as supernovae or planetary nebulae. Since stars form elements heavier than hydrogen in their cores throughout their lifetime, these ejecta are thoroughly enriched with heavier elements or "metals" which pollutes the gas that forms the next generation of stars. Therefore a galaxy, such as the Milky Way, will become more and more metal-enhanced over time. However, it is additionally complicated by the star formation rate at various regions of the Galaxy. Due to the surplus of star formation happening in the bulge there is additional enrichment occurring towards the center of the Galaxy as compared to the outer edges, which leads to a gradient in the metallicity as a function of Galactic radius.

The fraction of elements produced from different types of stellar deaths, results in differing amounts of various elements enriching the Galaxy. For instance, core-collapse supernovae produce more alpha elements (e.g., Na, Mg, Si, S, Ar) than iron-peak elements (V, Cr, Mn, Fe, Co, Ni, Cu, Zn), whereas Type Ia supernovae produce more iron-peak elements than alpha elements. Largely, the difference in yields is because alpha elements

are primarily concentrated within the outer layers of a star, and iron-peak elements are concentrated within the core. Type II supernovae occur with stars that have both their core and their atmosphere, whereas Type Ia supernovae happen with white dwarf stars that have already shed their alpha-rich atmospheres (e.g., Kobayashi et al. 2020, Andrews et al. 2020, and references therein). Therefore, we need to measure a range of elements from different chemical families (e.g., alpha, odd-Z, and iron peak) with tracer objects that have a wide range of ages to accurately explore the enrichment history of the Milky Way. The ideal tracer to use for this is star clusters, as both age and chemical make-up of the stars can be reliably determined.

1.2 Star Clusters

Stars are formed when small overdensities within large gas clouds undergo gravitational collapse and get hot and dense enough to begin fusion. This process is not isolated and often many stars, ranging from tens to thousands, are formed within a very limited time frame; creating a stellar association. The densest regions of a stellar association can create a gravitationally bound group of stars, which is then known as a star cluster. Consequently, as star cluster members form from the same gas cloud they all have essentially the same metallicity ([Fe/H]), distance from Earth, velocity, and age. The age especially is incredibly important for Galactic evolution studies, because deriving reliable stellar ages for isolated stars cannot be done without having access to a previously calibrated relationship. Moreover, open clusters are often used as the calibrators for these relationships because of the age range (from currently forming to $\sim 8-9$ Gyr old), reliability, and

relative ease with which we can determine their ages. While there are efforts to determine reliable ages for field stars through thoroughly calibrated relationships (e.g., Spoo et al. 2022, Viscasillas Vázquez et al. 2022, Casali et al. 2020), clusters remain the most reliable way to measure age in populations of stars and are essential for calibrating these methods. Also, star clusters are powerful tracers for studying chemical and dynamical evolution in the Milky Way and can be used to observationally constrain the Galactic abundance and metallicity gradients, which provide needed constraints to simulations that model the evolution of Milky Way-like galaxies. The term "star clusters" can also be further broken down into two main subcategories: open clusters and globular clusters.

Open clusters are found throughout the Milky Way's disk and are composed of stars that are typically relatively loosely bound together. Historically, the latter characteristic earned them the name "open" to indicate that they are open systems and are more likely to be broken apart by interactions with other systems in the Milky Way (e.g., interactions with spiral arms, or stars within the cluster going supernova). Nonetheless, open clusters have long been used as tracers to identify and study chemical trends within the Milky Way's disk, due to the wide ranges in both Galactic radii (4 kpc $< R_{GC} <$ 20+ kpc) and ages (5 Myr – 9 Gyr).

Milky Way halo globular clusters have many similarities to their "open" counterparts, but trace a distinctly different part of the Galaxy: the Galactic halo. In general, globular clusters are typically (1) more metal poor, (2) more massive (can contain hundreds of thousands of stars), (3) are old (10+ Gyr), and (4) located in the halo of the Milky Way. Due to their significantly higher masses and increased star formation efficiency, they are better able to retain their stars despite the stellar end-of-life events (e.g., supernovae)

and interactions with other objects which may occur throughout the cluster's lifetime. Consequently, this allows the cluster to have multiple generations of stars (e.g, Piotto (2009) and references therein), where gas within the cluster will re-coalesce and create new stars, which have a different age and metallicity from the original population of stars.

In both cases, the standard methods of measuring ages are the same. First, their member stars are plotted on a Color-Magnitude Diagram (CMD). For example, one type of CMD, based on photometry available from the ESA *Gaia* mission, is a plot of the stars' overall G-band magnitude (or brightness) versus its $bp - rp$ color-index, the later of which is a proxy for the temperature of the star. As a consequence of stellar evolution, lower-mass stars fuse hydrogen to helium on the main sequence for longer periods of time than the higher-mass stars in the cluster. This means that as time progresses more and more stars "turn off" the main sequence and begin their journey up the Red Giant Branch (RGB) and beyond. By using stellar evolution models with a range of masses (known as isochrones), which provide a model of what the cluster would look like at specific ages, calibrated to key benchmark clusters, we can then use these CMDs to identify likely ages for other clusters.

1.3 Stellar Spectroscopy and Stellar parameters

While much information can be gleaned from a star through photometric observations, a whole plethora of information is hidden within its spectrum. A spectrum is created by spreading out the light into a range of colors which can be seen as a plot of intensity versus, for example, wavelength. If there were no atoms within the stars atmosphere,

this spectrum would take the shape of a blackbody (a continuous function of wavelength dependent on only temperature). However, with the addition of a transparent stellar atmosphere, the spectrum displays various absorption features due to the presence of atoms in various states of excitation or ionization.

The spectrum of a star is strongly impacted by its fundamental stellar parameters (e.g., temperature, density, metal content, etc...). From quantum mechanics, it is well known that atoms will absorb photons at specific wavelengths and emit those photons some time later. In stars, the atoms in the atmosphere absorb the photons coming from within a stars' interior, and the strengths of the produced spectral lines are determined primarily by the temperature of the star. A stars temperature determines (1) whether certain atoms will be ionized or trapped in molecules and (2) what energy level(s) the electrons of an atom will primarily inhabit. Both of these factors directly determine which spectral lines will be more or less prevalent within the stars spectrum. Therefore, by looking at the depth and width of the spectral lines, it is possible to derive the stars temperature.

The width of the spectral lines can also indicate another fundamental parameter: surface density (also known as surface gravity). Stars which are on the main sequence have a stronger surface gravity than those which have evolved off since the evolved stars have an increased radiation pressure, which causes their radius to increase and therefore the density at the surface of the star to decrease. In terms of spectra, a star with strong surface gravity will have more collisions between atoms in the atmosphere of the star, which in turn broadens the width of the spectral lines. Finally, another fundamental parameter which can be estimated based on a stars spectrum is its Doppler or radial

velocity (RV). The RV of a star is its velocity along to the line of sight from Earth and can be derived by measuring the difference between a spectral line's known rest wavelength and the apparent line wavelength in the star.

Once the fundamental stellar parameters of a star have been accurately estimated, the individual abundances of elements within the star can be derived. In the case of large scale surveys, like that used in this work (described in detail in §2.1), models provide a multidimensional grid of stellar atmospheres to compare the star to and the best chi-squared χ^2 goodness of fit test is used to determine each individual stars' parameters and then abundances.

1.4 Using Star Clusters to Map Chemical Gradients within the Milky Way

Open clusters are key, age-datable tracers that have long been used to explore chemical trends in the Galactic disk. Since the early work of Janes (1979), numerous studies have advanced the field, particularly over the past 15 years (e.g., Sestito et al. 2008, Bragaglia et al. 2008, Friel et al. 2010, Carrera & Pancino 2011, Yong et al. 2012, Frinchaboy et al. 2013, Reddy et al. 2016, Cunha et al. 2016a, Netopil et al. 2016, Magrini et al. 2017, Donor et al. 2020, Spina et al. 2021, Netopil et al. 2022), with progress driven by the availability of larger telescopes, the expansion of multi-fiber spectroscopic capabilities, and, more recently, by large-scale high-resolution spectroscopic surveys. A few of these surveys are, the Large Sky Area Multi-Object fiber Spectroscopic Telescope (LAMOST; Luo

et al. 2015), GALactic Archeology with HERMES (GALAH; Martell et al. 2017), Gaia-ESO (Gilmore et al. 2012), Netopil et al. (2022), Open Cluster Chemical Abundances from Spanish Observatories (OCCASO; Casamiquela et al. 2017), and the Open Cluster Chemical Abundance and Mapping survey (OCCAM; Frinchaboy et al. 2013). These surveys and studies are briefly summarized in the following subsections.

1.4.1 The LAMOST Survey

The Large Sky Area Multi-Object Fiber Spectroscopic Telescope (LAMOST; Zhao et al. 2012), is a low-resolution (R $\sim$ 1800) spectroscopic survey which has observed 6,478,063 stars. Multiple studies (e.g., Zhang et al. 2021, Fu et al. 2022) have used LAMOST as the basis for an open cluster study. Zhang et al. (2021) compiles a sample of 225 open clusters with additional data from APOGEE and other observations to constrain the metallicity gradient, with a focus on young open clusters. Fu et al. (2022) compiles a homogeneous sample of 386 open clusters, with astrometric parameters cross-matched with Cantat-Gaudin et al. (2020) to investigate the metallicity gradient as a function of time as well as the orbital parameters of the clusters. However, while this provides a large sample of clusters, the low-resolution of LAMOST makes it difficult to measure individual elemental abundances reliably, so LAMOST can only provide a general [Fe/H] and [α/Fe] for its chemistry.

1.4.2 The HERMES/GALAH Survey

The GALactic Archeology with HERMES (GALAH; Martell et al. 2017) survey uses the High Efficiency and Resolution Multi-Element Spectrograph (HERMES, R $\sim 28,000$) at the Anglo-Austrailian telescope to measure up to 21 different elemental abundances, ranging from carbon to europium, for open cluster stars. In Spina et al. (2021), they homogenize the GALAH data with that from SDSS/APOGEE DR16 (Ahumada et al. 2020) to procure a reliable sample of 134 open clusters. However, of these clusters only 37 have data from GALAH and the homogenization of the two datasets risks inducing systemic offsets in the sample.

1.4.3 The Gaia-ESO Survey

Gaia-ESO (Gilmore et al. 2012) is a publicly available survey that provides high-quality spectra from the Very Large Telescope (VLT) FLAMES instrument, which uses the GIRAFFE (R $\sim 20,000$) and UVES (R $\sim 47,000$) spectrometers to acquire spectra for roughly 100,000 stars in the Galaxy, both in the field and in open clusters. The FLAMES instrument can measure 12+ elements in observed stars. The Gaia-ESO sample probes into $\sim$ 100 open clusters, spanning a wide range of ages and masses, but until very recently only a limited number of open cluster parameters had been published (Jackson et al. 2021, with results for 63 open clusters).

1.4.4 The Open Cluster Study in Netopil et al. (2022)

Netopil et al. (2022) used spectroscopic metallicities from literature studies plus data from the APOGEE survey to compile a sample of 136 open clusters, with Gaia DR2 membership. They use the combined sample of 136 open clusters to explore the Galactic metallicity gradient as well as the evolution of the metallicity gradient using eight different age bins. While this work provides a large sample of clusters, their compiled catalog has the potential for significant systematic effects due to their use of different telescopes and surveys which not only utilize different instruments, but can also have differing analysis pipelines, line lists, stellar models, and analysis / reduction methods. As shown in Figure 3 of Donor et al. (2018), the abundances derived in different studies can be significantly different, which can increase the amount of scattering within measured Galactic abundance gradients.

1.4.5 The OCCASO Survey

The Open Cluster Chemical Abundances from Spanish Observatories (OCCASO) survey (Casamiquela et al. 2019) provides results from 81 nights of observations. They use three high-resolution echelle spectrographs: (1) the Calar Alto Fiber-fed Echelle spectrograph (CAFE) on the Centro Astronómico Hispano en Analucía 2.2m telescope, (2) the FIber-fed Echelle Spectrograph (FIES) spectrograph on the 2.5m Nordic Optical Telescope, and (3) HERMES on the 1.2 m Mercator telescope. Both FIES and HERMES are at the Observatorio del Roque de los Muchachos. All of the above spectrographs are high-resolution ($R \geq 65000$) which allows the authors to create a sample of 18 open

clusters. They use these open clusters to investigate the abundance gradients for 10 different elements (including [Fe/H]). While their sample covers a wide range of radii ($6.6 \leq R < 11$ kpc) and age (0.5 Gyr to 2 Gyr), they also bolster their sample with data from GALAH and APOGEE to provide a more robust sample, again introducing potential systematics by combining data from differing sources.

1.4.6 The OCCAM Survey

The goal of the Open Cluster Abundance and Mapping Survey (OCCAM ; Frinchaboy et al. 2013, Cunha et al. 2016b, Donor et al. 2018; 2020, Ray et al. 2022, Spoo et al. 2022) is to produce a comprehensive, *uniformly measured*, infrared-based spectroscopic data set for stars in hundreds of open clusters, and to constrain key Galactic dynamical and chemical parameters. This work aims to extend the OCCAM survey. The primary data for the OCCAM survey come from the Sloan Digital Sky Survey III (SDSS III; Eisenstein et al. 2011) and SDSS IV (Blanton et al. 2017) / Apache Point Observatory Galactic Evolution Experiment (APOGEE; Majewski et al. 2017) that is described in more detail in §2.1. In the previous OCCAM iteration based-on APOGEE DR16, Donor et al. (2020) (hereafter, OCCAM-IV), they obtained a sample of 128 open clusters, 71 of which were designated to be high-quality, to investigate the metallicity and abundance gradients of the Milky Way. They included 16 different elements, and found evidence that the Galactic gradients in Fe, Mn, and Al do seem to change as a function of time. In addition, they also used their sample to further constrain the metallicity gradient by fitting it with a break in the slope.

In this work, we present the complete OCCAM APOGEE sample, which is based on the SDSS-IV Data Release 17 (DR17) (Blanton et al. 2017, Abdurro'uf et al. 2022), the most recent and final release of data products from APOGEE-2 (Majewski et al. 2017, Holtzman et al., *in prep*). We will analyze Galactic gradient trends in metallicity ([Fe/H]), α elements (O, Mg, Si, S, Ca, Ti), iron-peak elements (V, Cr, Mn, Co, Ni), and other elements (Na, Al, K, Ce) represented in the APOGEE DR17 database, and explore the evolution of these gradients as a function of age. We also calculate the trends with Galactocentric guiding center radius (R_{guide}) to investigate the potential biases that may affect the analysis by using the current cluster locations. The guiding center radius of a given general, eccentric orbit is the radius of a circular orbit with the same angular momentum as the generic orbit. It will be described in more detail in §3.2. Finally, we discuss this sample in comparison to other recent literature studies of open clusters.

Chapter 2

Data

As discussed in 1.4, one of the challenges for Galactic abundance gradient studies is acquiring a large enough *uniform* sample of clusters to thoroughly sample the Milky Way's disk and robustly fit the chemical trends. Until recently, studies had to combine data from multiple sources in order to bolster their samples, which inherently introduced systemic offsets into the data. To avoid these systemic offsets, this work utilizes data from only two sources: SDSS/APOGEE (Majewski et al. 2017), for spectroscopic data, and *Gaia* (Gaia Collaboration et al. 2016), for photometric data.

2.1 SDSS/APOGEE DR17

The seventeenth data release of SDSS-IV/APOGEE survey (Abdurro'uf et al. 2022) provides the chemical abundances and radial velocities for the cluster samples. This final data release for the APOGEE survey provides high-resolution ($R \simeq 22,500$), near-infrared ($1.51\mu m \leq \lambda \leq 1.70\mu m$) spectra taken with the APOGEE spectrographs (Wilson et al. 2019), which includes spectra for over 650,000 stars, to derive stellar parameters and chemical abundances.

These data were taken using the Sloan Foundation telescope at the Apache Point Observatory (New Mexico, APO; Gunn et al. 2006) in the Northern Hemisphere and the Du Pont telescope at the Las Campanas Observatory (Chile, LCO; Bowen & Vaughan 1973) in the Southern Hemisphere. The observations for APOGEE-1, which only included the northern hemisphere, ran from September 2011 - July 2014, and those for APOGEE-2, which covered both hemispheres, ran from August 2014 - January 2021. The data from APOGEE-1 and APOGEE-2 are included in the seventeenth data release

of SDSS/APOGEE. Targeting for the APOGEE survey, including details from this program, are described in Frinchaboy et al. (2010), Zasowski et al. (2013), Zasowski et al. (2017), Beaton et al. (2021), and Santana et al. (2021).

APOGEE data are reduced using the APOGEE data reduction pipeline (Nidever et al. 2015) and the APOGEE Stellar Parameters and Chemical Abundances Pipeline (ASPCAP García Pérez et al. 2016). By comparing and finding the best χ^2 match between the reduced APOGEE data and a library of synthesized stellar spectra, generated by the synspec code (Hubeny & Lanz 2017, Hubeny et al. 2021), ASPCAP estimates the atmospheric parameters of the star. These parameters include: effective temperature (T_{eff}), surface gravity ($\log(g)$), microturbulance at the surface of the star (v_{micro}), stellar rotation ($v \sin(i)$) or macroturbulance at the surface of the star (v_{macro}), overall abundance of metals ([M/H]), relative α-element abundance ([α/M]), as well as the carbon and nitrogen abundances ([C/M] and [N/M], respectively), which are estimated from molecular bands (CH, CN, CO) within the spectra. Once those parameters are estimated, ASPCAP then measures the desired chemical abundances by narrowing the focus to specific regions of the spectrum with the necessary spectral features. For a visual, see Figure 2.1, which is Figure 4 in García Pérez et al. (2016), to show the molecular bands in the APOGEE wavelength regime and the windows which are used to derive abundances for each element. More in depth descriptions of the extraction of chemical abundances are provided in Holtzman et al. (2015; 2018), Jönsson et al. (2020) and Holtzman et al., *in prep*[1]

[1]Description of DR17 and the actual data can be found at www.sdss.org/dr17/.

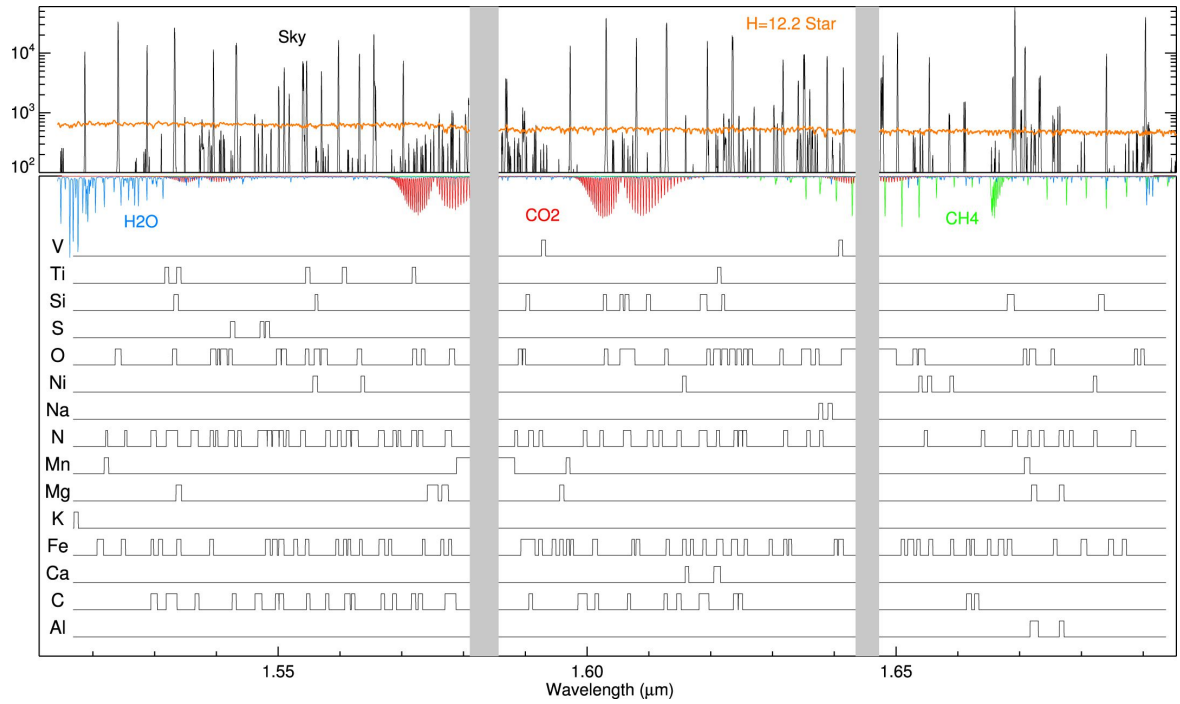

Figure 2.1: A reproduced Figure 4 from García Pérez et al. (2016) that illustrates the available wavelength range covered in APOGEE spectra. At the top of the Figure, it includes a stellar spectrum (orange), the molecular bands (red, green, blue) and the emission lines (black) present due to the Earth's atmosphere. Below, it provides the windows used to derive the abundances for the 15 different elements available in APOGEE. In this figure, each window is broadened by 30km/s to make it easier to see.

This project uses the data derived by the standard SDSS/APOGEE pipelines. For more information regarding the APOGEE data products or the pipelines, see Abdurro'uf et al. (2022) and Holtzmann et al. (*in prep*).

2.1.1 Pipeline Changes from APOGEE DR16 to DR17

Between the latest APOGEE data release used for this work and the previous one used in Donor et al. (2018; 2020), some significant changes were made to the APOGEE pipeline. First, new synthetic spectral libraries were created using the Synspec code (Hubeny & Lanz 2017, Hubeny et al. 2021). These libraries include new Non-LTE corrections and inter-element effects to the abundances analysis of sodium, magnesium, potassium, and calcium with the computations in Osorio et al. (2020), improving the abundance derivations for these elements. Second, the APOGEE line list used for DR17 was updated from Shetrone et al. (2015) to Smith et al. (2021). While a schematic description of the DR17 pipeline is given in Abdurro'uf et al. (2022), further specifics about updates to the APOGEE pipeline will be discussed in Holtzman et al. (*in prep*). The changes to the pipeline were applied to all data taken before and after the sixteenth data release. The consequences of these changes can be seen in the comparisons between Donor et al. (2020) and Myers et al. (2022), found in Chapter 4.3.1

2.2 Gaia EDR3

To supplement the SDSS/APOGEE data and provide astrometric and photometric parameters for our analysis we use data from *Gaia* Early Data Release 3 (EDR3 Gaia

Collaboration et al. 2021). The data for the *Gaia* survey is provided by the *Gaia* space telescope (Gaia Collaboration et al. 2016), which orbits at the L2 Lagrange point approximately 1.5 million km from the Earth. This location provides an unobstructed view of the entire sky, and allows *Gaia* to repeatedly measure the positions and velocities of stars once a year. The *Gaia* EDR3 release includes the data collected between July 2014 to May 2017 and proceeds the release of *Gaia* DR3. In total, we analyzed proper motions and parallaxes for $3,720,692$ stars out of the ~ 1.8 billion sources included in *Gaia* EDR3, and we use *Gaia* radial velocities for $38,667$ stars of the available ~ 7 million RVs (Seabroke et al. 2021). Additionally, we check the offset between Gaia EDR3 RVs and APOGEE DR17 RVs and find the median offset to be roughly -0.14 km/s with a standard deviation of approximately 2.80 km/s.

2.2.1 Pipeline Changes from Gaia DR2 to EDR3

On top of the additional data provided in *Gaia* EDR3, it also presents more precise proper motion and parallax values, as well as more precise and accurate photometry than was included in *Gaia* DR2. While the RV values are carried from *Gaia* DR2 to *Gaia* EDR3, they were additionally cleaned before being added to *Gaia* EDR3. The RV sources from *Gaia* DR2 which were not included in *Gaia* EDR3 were either excluded because they could not be matched to *Gaia* DR3 sources or were compared to the initial RV calculations in *Gaia* DR3 and were deemed to be unreliable (Seabroke et al. 2021). The consequences of these changes are also discussed in more context in §4.3.1.

Chapter 3

Methods

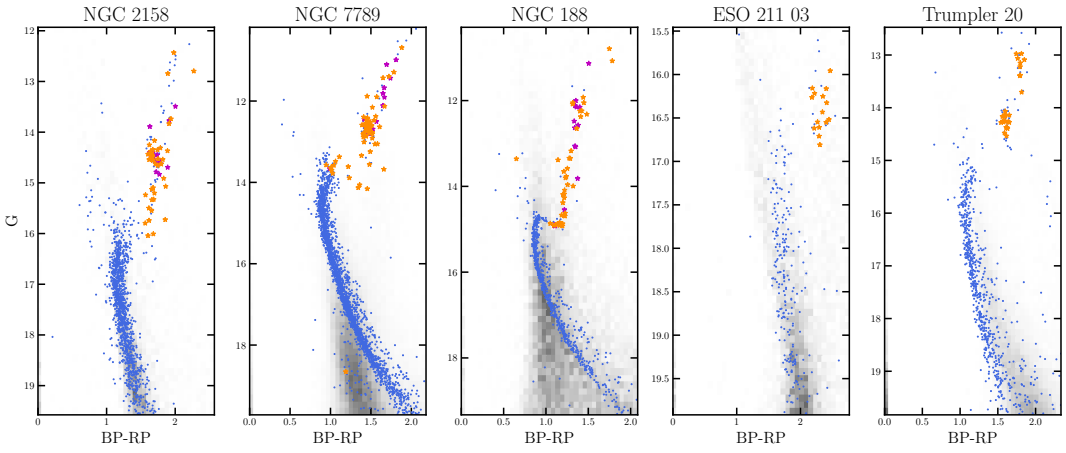

Figure 3.1: Five example color-magnitude diagrams of open clusters analyzed in this study (Table A.1). Stars from *Gaia* EDR3 within twice the cluster radius, as defined in Cantat-Gaudin et al. 2020, are included; stars identified as PM members and inside the cluster radius are blue. Non-member stars are shown as a Hess diagram in grey. The OCCAM pipeline-identified APOGEE members from DR16 (Donor et al. 2020) are shown in purple. New DR17 OCCAM pipeline-identified APOGEE member stars are shown as orange stars.

In order to study the stars within a cluster, we must first isolate cluster member stars from the "field" stars, random Milky Way stars in the foreground and background along the same line of sight but not a part of the cluster. To identify stars which are more likely to be a part of the cluster, we employ the analysis described in Frinchaboy & Majewski (2008) and Donor et al. (2018; 2020) which primarily boils down to two techniques: The Rayleigh-Jeans Color Excess (RJCE) method (Majewski et al. 2011, Frinchaboy et al. 2010), used to select likely target stars, and a tiered kernel-based smoothing routine after the data was collected.

The RJCE method utilizes photometric near IR data from the 2 Micron All Sky Survey (2MASS; Cutri et al. 2003) and mid-IR data from the Wide-field Infrared Survey Explorer (WISE; Wright et al. 2010) to estimate the extinction of individual stars within twice the clusters radius. This is possible because the intrinsic shape of a stars spectral

energy distribution in the long wavelength regime is a constant for the large majority of stars, the "Rayleigh-Jeans tail". Thus by measuring the difference between the near-IR H band (1.6 μm) filter of the 2MASS survey and the mid-IR $W2$ (4.5 μm) filter from the WISE mission we can determine the reddening of the stars. Once the reddening is determined, we furthermore split the sky into five extinction-based bins, subtract the mean field star numbers from the region associated with the cluster, and find the extinction bin with the largest concentration of stars within the cluster radius (see Frinchaboy & Majewski 2008, Donor et al. 2018, for more details). By identifying the extinction of the cluster, it is easier to eliminate stars which have extinctions that are significantly larger and smaller than the clusters (stars that are too close and too far away to be in the cluster), thus allowing for the identification and elimination of field stars lying along the line-of-sight.

Afterwards, we utilize APOGEE data to further clean the cluster members from the field stars by employing a kernel-based Gaussian smoothing routine to isolate member stars. This routine takes both the probable cluster stars and those that are outside the cluster radius, and convolves each of their proper motion (PM), radial velocity (RV), and metallicity measurements with a Gaussian distribution such that each stars value is the Gaussian's peak. After, these Gaussians are added together for all the stars, and the distribution of the field stars are subtracted from the total distribution to leave only the cluster. This is first done in PM space, then the PM-cleaned sample is used to repeat the process and estimate the cluster's RV, then finally the process is repeated once again in metallicity space to estimate the clusters final metallicity.

The star's position relative to the normalized, fitted Gaussians are used to determine the membership probabilities of each star based upon their PM, RV, and metallicity measurements independently, where a reported probability greater than 0.01 is within 3σ of the cluster mean. In practice, these fit distributions are fairly tight (see Figure 2 in Donor et al. 2018 for a figure set showing distributions for [Fe/H], PM, and RV for 19 clusters), therefore a star falling within 3σ of the cluster mean in all 3 parameter spaces is deemed likely to be a cluster member for the purposes of this work.

As in Donor et al. (2020), we also use visual quality checks of both the color magnitude diagrams (CMDs) and Kiel diagrams (T_{eff} vs $log(g)$) for the APOGEE stars in each cluster to distinguish between high quality clusters, where the OCCAM pipeline-identified member stars are located on a verifiable main sequence, horizontal branch, or red giant branch within the clusters CMD (given a quality flag of 1 or 2)[1]; and potentially unreliable clusters, where the clusters structure is either too sparse or too obscured to be fully reliable (given a quality flag of 0). As an example of both the CMDs used and the difference between APOGEE DR16 and DR17, we show five example clusters in Figure 3.1, all with a quality flag of 1 or 2. This figure, shows that the addition of APOGEE DR17 not only expands the number of stars that are identified to be likely cluster members in previously known clusters, but it also expands the number of clusters that can be added to this sample.

[1]The quality flag of 2 denotes a cluster used in the calibration sample from Donor et al. (2018).

3.1 Methodology Changes from Donor et al. (2020)

The present analysis adopts several changes in methodology from that employed in Donor et al. (2020). In addition to using the latest stellar parameters and abundances from the greatly expanded APOGEE DR17 sample, we also use the latest data from the Gaia Collaboration et al. (2016), EDR3, to take advantage of the extended baseline and expanded astrometric catalog. We also use the open cluster parameters from Cantat-Gaudin et al. (2020), which exclusively uses *Gaia* DR2 to compile a catalog that provides uniform measurements of age and distance (among other parameters) for roughly 2,000 open clusters. This catalog includes all the open clusters used here for analysis of the Galactic chemical gradients.

Another change in methodology applied to our analysis is the addition of the guiding center radius, R_{guide}, which is now used along with galactocentric radius, R_{GC}, to compute the Galactic abundance gradients. Methods for the calculation of R_{guide} are further discussed in §3.2.[2] Finally, because more Ce II lines were used in DR17 to determine the abundance of Ce in ASPCAP, the cerium abundance measurements have significantly improved over those in DR16; as a result, we are able to explore the Galactic trends in cerium here.

[2]For two clusters (FSR 0542 and NGC 2232) that were not initially recovered using the OCCAM pipeline, we implemented a parallax cut for stars greater than twice the reported distance to the cluster (Cantat-Gaudin et al. 2020) and those less than half the distance to the cluster.

3.2 Computing Guiding Center Radii R_{guide}

For each cluster in the sample, we compute its guiding-center radius, R_{guide} , using the circular velocity rotation curve from the best-fitting Milky Way model described in Price-Whelan et al. (2021). We compute the approximate guiding center radii for the OCCAM clusters by first transforming their heliocentric position and velocity data (sky position, distance, proper motions, and radial velocity) into Galactocentric Cartesian coordinates, assuming solar parameters: for the Sun–Galactic center distance we adopt $R_{\odot} = 8.275$ kpc (Gravity Collaboration et al. 2021), a solar height above the Galactic midplane of $z_{\odot} = 20.8$ pc (Bennett & Bovy 2019), and a solar velocity with respect to the Galactic center $\boldsymbol{v}_{\odot} = (8.42, 250.2, 7.90)$ km s^{-1} (Drimmel & Poggio 2018, Gravity Collaboration et al. 2018, Reid & Brunthaler 2004). We then compute the z-component of the angular momentum vector, L_z, for each cluster in the Galactocentric frame and estimate the guiding center radii as $R_{guide} = L_z/v_c(R)$, where R is the present-day cylindrical radius of each cluster and $v_c(r)$ is the circular velocity curve evaluated at the radius of each cluster.

The use of the guiding center radius of a cluster, rather than its present galactocentric radius, has the advantage of correcting for orbital blurring effects in the metallicity gradients due to the inherent ellipticity of orbits (e.g., Netopil et al. 2022, Zhang et al. 2021, Spina et al. 2021). To illustrate and explore the differences between R_{guide} and R_{GC}, we calculate R_{guide} and discuss both radii in §4.2 and §4.3.

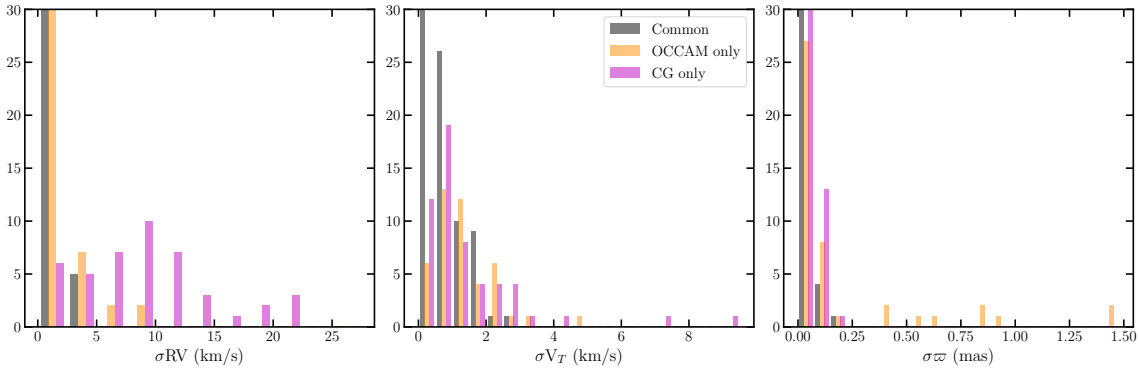

Figure 3.2: We present the measured standard deviations of three key cluster properties (radial velocity, transverse velocity, and parallax) using three different membership sub-samples: 1) includes member stars common to both our OCCAM analysis and Cantat-Gaudin et al. (2018), 2) OCCAM members that are not Cantat-Gaudin et al. (2018) members (OCCAM only), and 3) Cantat-Gaudin et al. (2018) only member stars (CG only). NOTE: the histogram are artificially cut-off at 30 to show relevant detail.

3.3 Membership Comparison to Cantat-Gaudin et al. (2018)

Cantat-Gaudin et al. (2018) performed a fundamentally different membership analysis than presented here and previously by OCCAM (Donor et al. 2018; 2020). Whereas our analysis relies on kernel convolution and Gaussian fitting to define a rigid boundary for what constitutes "the cluster", Cantat-Gaudin et al. (2018) performed a clustering search in the 5 dimensional *Gaia* phase space (RA, dec, proper motion, and parallax [ϖ]), requiring no fitting or boundary setting. Furthermore, while Cantat-Gaudin et al. (2018) uses parallax along with proper motion, this work uses RV and [Fe/H] along with proper motion, which causes generally small but occasionally significant differences between the two membership analyses.

In order to compare the results from the two methods, we divide stars into three categories: common (stars considered cluster members in both the OCCAM and the Cantat-Gaudin et al. (2018) samples), OCCAM only (stars that are included in the present sample but not in Cantat-Gaudin et al. 2018), and CG only (stars rejected from the present sample but included in Cantat-Gaudin et al. 2018). We create a statistic that accentuates differences between these three samples in RV, transverse velocity (V_T, calculated using the cluster distance measured by Cantat-Gaudin et al. 2020), and parallax (ϖ). To compute this statistic, we first measure the mean cluster value for stars in the common sample ($\bar{x}_{common}$). We then compute the average deviation of the OCCAM only and the CG only samples ($x_{single\ sample}$) from $\bar{x}_{common}$, shown in Eq. 3.1.

$$\sigma_{mod} = \frac{1}{n} \sum \left(\bar{x}_{common} - x_{single\ sample} \right) \tag{3.1}$$

In Figure 3.2, we plot a histogram of RV, V_T, and ϖ with (1) the 1-σ standard deviation of the common sample within each cluster in gray, (2) σ_{mod} for OCCAM only in orange, and (3) σ_{mod} for CG only in purple. There are 92 clusters in our sample where the results of our membership analysis differ from Cantat-Gaudin et al. (2018); we omit the remaining clusters from this analysis as it is designed to show differences. To show relevant detail we artificially cut off each histogram at 30; in all 3 panels the lowest bin is populated beyond what is shown. Since the common sample is more restrictive than either individual sample it is not surprising that we measure a small standard deviation for the common sample of stars in most clusters. We note the scale difference between

the RV and V_T histograms: the first 5 bins in the V_T plot span 0–2.5 km/s, which is the size of the first bin in the RV plot.

For the common sample, 67 of 92 clusters for which we measure RV dispersion have measured dispersions below 1 km/s, and in V_T we find 71 of 92 clusters showing a dispersion below 1 km/s, in good agreement with typical cluster dispersions (e.g., Cantat-Gaudin & Anders 2020) and despite not explicitly removing binary stars. For ϖ the majority of the OCCAM only clusters show low dispersions, comparable to the common sample and CG only sample, with 83 of 92 clusters having dispersions < 0.25 mas, despite the fact we have not used ϖ in our selection. For the remaining nine clusters, five are in our low quality sample. Of the four in our high quality sample two are very nearby, Melotte 22 (The Pleiades) and Ruprecht 147, so some dispersion in ϖ is expected. The remaining two clusters, FSR 0496 and NGC 7789, each have one star with negative ϖ reported, significantly affecting the measured dispersion.

This analysis shows that despite different selection criteria, the reliability of our sample is comparable to Cantat-Gaudin et al. (2018), where we can compare directly. We find inconsistencies in ϖ in our sample, which is not surprising since ϖ is not accounted for in our analysis. Similarly, we show there is significant RV variation in the Cantat-Gaudin et al. (2018) sample since RV was not accounted for in that analysis. A union of the two samples is straightforward to create using the VAC discussed in §4.1.1. Combining the 5 dimensional *Gaia* phase space with RV and [Fe/H] would produce a purer sample, but in the present work we have chosen to continue using the (Donor et al. 2020) (hereafter, OCCAM-IV) membership selection pipeline for consistency.

3.4 Methodology Changes for Globular Clusters

In addition to the open clusters sample, this work also includes globular clusters, providing a sample of clusters that probes the Galactic halo instead of the Galactic disk. As globular clusters are studied by different groups/analysis (e.g., *Gaia* catalogs), a few adjustments were made to enable the globular clusters to be processed through the OCCAM pipeline. First, the catalogs used for initial guesses and overall cluster values needed to be changed. Therefore, we drew from the list of possible Milky Way globular clusters from the Harris Catalog (Harris 1996, 2010 version), which provides a compiled list of 153 globular clusters with their IDs, positions, metallicities, magnitudes, colors, RVs, velocity dispersions, and structural parameters from other studies. We specifically use the celestial coordinates (RA/Dec) and the reported half light radius ($3 \times r_h$) as inputs to the OCCAM pipeline. Ages for the globular cluster sample comes from Wagner-Kaiser et al. (2017), which uses data from the HST and a Baysian analysis technique to estimate fundamental parameters of each cluster, including the age. Additionally, initial guesses for the cluster's overall proper motion value are provided by the *Gaia* EDR3 based study, Vasiliev & Baumgardt (2021). This study also provides the membership probabilities for each cluster, therefore we include the membership probabilities from the Vasiliev & Baumgardt (2021) catalog to check and compare the results from the OCCAM pipeline.

Second, the RV and metallicity fitting routines also changed. Most notably, globular clusters can have a much larger dispersion in both RV and in metallicity than open clusters do, therefore, the maximum sigma value in each parameter was widened to not cut out valid cluster members. Additionally, an issue with the *Gaia* RVs meant that

for large clusters (e.g., 47 Tuc) the RV distribution was skewed, most likely due to systematics between the derived RVs and stars with extreme temperatures. As such, we fit the RV distribution excluding the available *Gaia* RV values, which were included in the RV fitting of the open cluster sample.

Chapter 4

Open Cluster Chemical Abundance and Mapping Survey

4.1 The OCCAM DR17 Sample

Our SDSS/APOGEE observed sample consists of 150 open clusters with 2061 member stars, out of $\sim 26,700$ stars in the vicinity of a known open cluster considered in this analysis. The final sample of clusters is shown in Figure 4.1. After a visual CMD inspection (described further in §3 and in OCCAM-IV), we designate 94 clusters as "high quality". All clusters analyzed are presented in Table 4.1 and Table 4.2 (with full version of the tables provided in the Appendix, Table A.1 and Table A.2). Where Table 4.1 (A.1) includes bulk cluster parameters derived or adopted for this study, and Table 4.2 (A.2) includes bulk cluster abundances, which are averaged over the stellar members.

For all Galactic abundance analysis in this study, we choose to use only clusters flagged as high quality and that have distances available from Cantat-Gaudin et al. (2020). Additionally, we also cut out two clusters with an age less than 50 Myrs (NGC 7058 and Teutsch 1), due to previous studies suggesting the young star pipeline results from APOGEE may be unreliable. Since young stars have an increased amount of chromospheric activity, it is difficult for the ASPCAP pipeline to estimate fundamental parameters, such as RV and $\log(g)$, which are needed for a reliable abundance determination (e.g., Kounkel et al. 2018, Olney et al. 2020). This results in a final sample of 85 clusters, which will be used to study the Galactic abundance gradients.

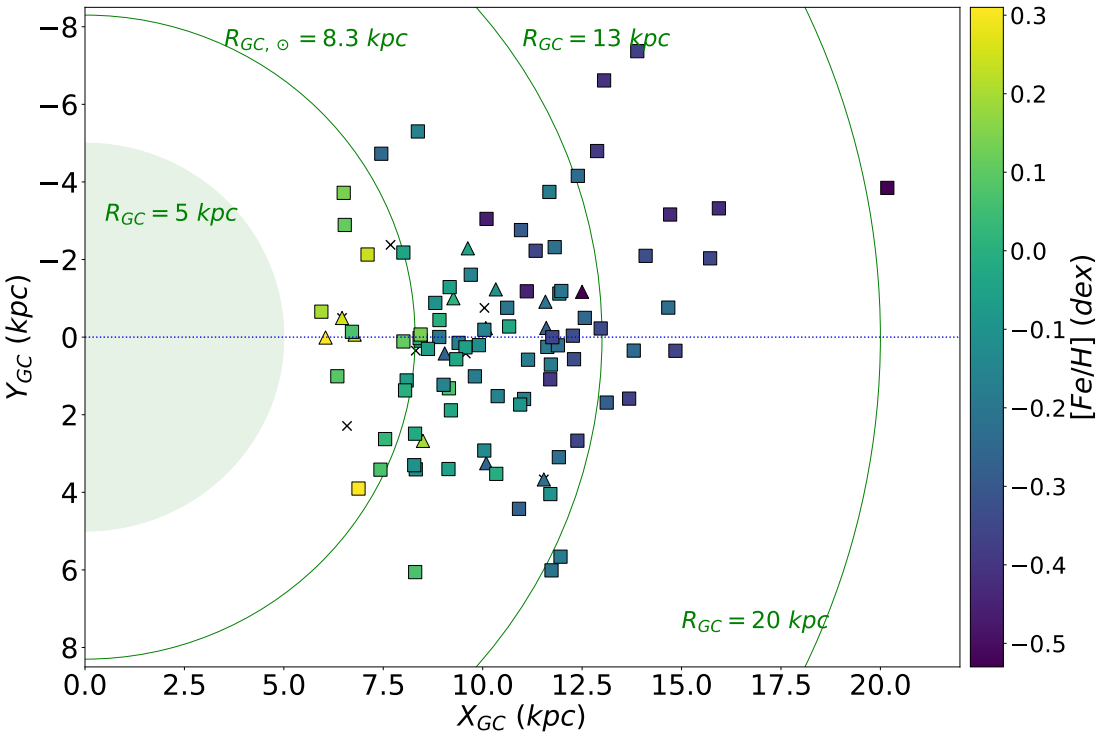

Figure 4.1: The OCCAM DR17 sample in common with Cantat-Gaudin et al. (2020) plotted in the Galactic plane, color-coded by [Fe/H]. Square points are "high quality" clusters, triangles are the lower quality clusters, and crosses denote clusters which were in the "high quality" sample of OCCAM-IV but are now in the "low quality" sample.

Table 4.1: OCCAM DR17 "High Quality" Sample Basic Parameters

Cluster	Qual	l	b	R [a]	Age [a]	R_{GC} [b]	R_{Guide} [b]	μ_α [c]	μ_δ [c]	RV	[Fe/H]	Num
name	flag	(deg)	(deg)	(′)	Gyr	(kpc)	(kpc)	(mas yr^{-1})	(mas yr^{-1})	(km s^{-1})	(dex)	stars
Ruprecht 147	1	20.9297	−12.7606	78.2	3.020	7.98	8.01	-0.89 ± 0.09	-26.73 ± 0.08	$+42.1 \pm 0.9$	$+0.11 \pm 0.03$	35
NGC 6705	1	27.3031	−2.7726	8.9	0.309	6.40	6.40	-1.50 ± 0.03	-4.21 ± 0.02	$+35.1 \pm 1.0$	$+0.09 \pm 0.04$	12
Berkeley 43	1	45.6820	−0.1347	5.8	nan	39.00	nan	-0.95 ± 0.02	-3.55 ± 0.02	$+30.1 \pm 0.0$	-0.01 ± 0.01	1
NGC 6791	2	69.9644	+10.9065	8.2	6.310	7.89	6.47	-0.40 ± 0.01	-2.26 ± 0.02	-46.9 ± 1.2	$+0.31 \pm 0.04$	66
NGC 6819	2	73.9815	+8.4811	11.4	2.239	7.97	8.53	-2.87 ± 0.01	-3.93 ± 0.01	$+2.6 \pm 1.3$	$+0.03 \pm 0.04$	46
Berkeley 85	1	75.6967	+0.9969	6.8	0.417	8.15	7.67	-2.91 ± 0.03	-4.67 ± 0.02	-33.7 ± 1.4	$+0.07 \pm 0.06$	12
Dolidze 41	1	75.7070	+0.9923	5.5	nan	nan	nan	-2.91 ± 0.03	-4.66 ± 0.02	-33.9 ± 1.1	$+0.06 \pm 0.06$	11
NGC 6811	2	79.2072	+11.9983	22.8	1.072	8.14	9.11	-3.24 ± 0.02	-8.83 ± 0.03	$+7.5 \pm 0.3$	-0.06 ± 0.01	7
NGC 6866	1	79.5615	+6.8368	12.5	0.646	8.14	9.36	-1.28 ± 0.03	-5.82 ± 0.04	$+13.1 \pm 0.8$	$+0.00 \pm 0.02$	4
IC 1369	1	89.6059	−0.3978	5.2	0.288	8.89	9.11	-4.58 ± 0.01	-5.71 ± 0.03	-48.7 ± 0.1	-0.11 ± 0.03	3

Table A.1 is published in its entirety in Appendix A

[a] Cluster Radius and age from Cantat-Gaudin et al. (2020)

[b] Calculated with distances from Cantat-Gaudin et al. (2020), recomputed to a solar radius of $R_0 = 8.274$ kpc.

[c] μ_α and μ_δ and their 1σ uncertainties are those of the 2D Gaussian fit, as in OCCAMII.

Table 4.2: OCCAM DR17 Sample - Detailed Chemistry

Cluster name	[Fe/H] (dex)	[O/Fe] (dex)	[Na/Fe] (dex)	[Mg/Fe] (dex)	[Al/Fe] (dex)	[Si/Fe] (dex)	[S/Fe] (dex)	[K/Fe] (dex)
	[Ca/Fe] (dex)	[Ti/Fe] (dex)	[V/Fe] (dex)	[Cr/Fe] (dex)	[Mn/Fe] (dex)	[Co/Fe] (dex)	[Ni/Fe] (dex)	[Ce/Fe] (dex)
Ruprecht 147	0.11 ± 0.03	0.01 ± 0.07	0.01 ± 0.20	-0.03 ± 0.04	0.11 ± 0.07	0.05 ± 0.05	-0.01 ± 0.05	0.04 ± 0.16
	-0.03 ± 0.05	-0.20 ± 0.24	-0.07 ± 0.16	-0.14 ± 0.21	0.05 ± 0.03	-0.33 ± 0.53	0.01 ± 0.02	-0.43 ± 0.72
NGC 6705	0.09 ± 0.04	-0.06 ± 0.02	0.25 ± 0.06	-0.04 ± 0.02	-0.09 ± 0.04	0.01 ± 0.01	0.04 ± 0.03	-0.14 ± 0.04
	-0.04 ± 0.02	-0.01 ± 0.02	-0.21 ± 0.07	0.00 ± 0.04	0.10 ± 0.02	0.06 ± 0.04	0.03 ± 0.02	0.13 ± 0.10
Berkeley 43	-0.01 ± 0.01	-0.04 ± 0.01	0.15 ± 0.05	-0.05 ± 0.01	-0.17 ± 0.02	0.02 ± 0.01	0.13 ± 0.03	-0.17 ± 0.03
	-0.05 ± 0.01	-0.03 ± 0.02	-0.40 ± 0.06	-0.09 ± 0.03	0.11 ± 0.01	-0.02 ± 0.04	0.04 ± 0.01	0.30 ± 0.06
NGC 6791	0.31 ± 0.04	0.05 ± 0.02	0.17 ± 0.05	0.08 ± 0.02	0.02 ± 0.05	0.01 ± 0.03	-0.01 ± 0.07	0.09 ± 0.09
	-0.04 ± 0.04	0.15 ± 0.10	-0.20 ± 0.20	0.04 ± 0.06	0.05 ± 0.11	0.14 ± 0.06	0.02 ± 0.04	-0.14 ± 0.10
NGC 6819	0.03 ± 0.04	-0.00 ± 0.03	0.09 ± 0.09	0.02 ± 0.01	0.01 ± 0.04	0.01 ± 0.02	-0.01 ± 0.04	-0.03 ± 0.07
	0.00 ± 0.02	0.03 ± 0.03	-0.13 ± 0.14	0.01 ± 0.03	0.02 ± 0.03	0.04 ± 0.06	0.00 ± 0.02	-0.03 ± 0.10
Berkeley 85	0.07 ± 0.06	-0.06 ± 0.05	0.20 ± 0.12	-0.05 ± 0.03	-0.10 ± 0.06	-0.02 ± 0.03	0.05 ± 0.08	-0.02 ± 0.06
	-0.08 ± 0.04	0.02 ± 0.05	-0.22 ± 0.08	-0.09 ± 0.17	0.10 ± 0.06	-0.04 ± 0.36	0.02 ± 0.04	0.09 ± 0.43
Dolidze 41	0.06 ± 0.06	-0.04 ± 0.04	0.22 ± 0.10	-0.05 ± 0.02	-0.10 ± 0.06	-0.01 ± 0.03	0.03 ± 0.07	-0.03 ± 0.07
	-0.07 ± 0.02	0.01 ± 0.05	-0.21 ± 0.07	-0.09 ± 0.17	0.12 ± 0.03	0.07 ± 0.05	0.02 ± 0.03	0.19 ± 0.27
NGC 6811	-0.06 ± 0.01	-0.03 ± 0.04	0.08 ± 0.07	0.00 ± 0.01	-0.02 ± 0.02	0.00 ± 0.01	0.02 ± 0.03	-0.05 ± 0.04
	0.02 ± 0.02	-0.01 ± 0.03	0.12 ± 0.09	0.04 ± 0.04	-0.02 ± 0.01	-0.08 ± 0.11	-0.03 ± 0.01	0.13 ± 0.09
NGC 6866	0.00 ± 0.02	-0.06 ± 0.02	0.04 ± 0.10	0.00 ± 0.01	-0.03 ± 0.02	-0.01 ± 0.01	0.06 ± 0.03	-0.03 ± 0.03
	0.01 ± 0.02	-0.01 ± 0.02	0.14 ± 0.09	0.03 ± 0.04	0.01 ± 0.01	-0.09 ± 0.07	-0.03 ± 0.02	0.09 ± 0.09
IC 1369	-0.11 ± 0.03	-0.03 ± 0.02	0.12 ± 0.06	-0.02 ± 0.01	-0.05 ± 0.03	-0.01 ± 0.01	0.09 ± 0.08	-0.01 ± 0.04
	0.01 ± 0.02	-0.06 ± 0.02	0.17 ± 0.09	-0.01 ± 0.04	0.01 ± 0.01	-0.03 ± 0.06	-0.06 ± 0.01	0.21 ± 0.09

Table A.2 is published in its entirety in Appendix A

4.1.1 Data Access - SDSS Value Added Catalog

The VAC consists of two FITS tables. The first, `occam_cluster-DR17.fits`, is a combination of Table A.1 and Table A.2, providing bulk cluster parameters derived here, PM from *Gaia*, as well as RVs and average abundances for 16 reliable chemical species available in APOGEE DR17. The second table, `occam_member-DR17.fits`, contains all of the APOGEE stars considered in this analysis (all of the stars that fall within two radii of the cluster center given by Cantat-Gaudin et al. (2020); $2 \times Radius_{CG}$) and reports the membership probabilities determined by the OCCAM pipelines (for [Fe/H], RV, and PM) as well as the membership probability from Cantat-Gaudin et al. (2020) for convenience. These four probabilities reported reflect how far a given stellar parameter is from the fit cluster mean, where a reported probability of > 0.01 is within 3σ of the cluster mean. We also note that within the VAC, R_{GC} was calculated with an $R_{\odot}$ of 8 kpc, whereas for this work, we recalculated R_{GC} with a solar radius of 8.275 kpc to be consistent with Gravity Collaboration et al. (2021). Table 4.3 shows all columns available in the occam_member table. The catalog is available from sdss.org.[1]

[1]The full url is `https://www.sdss.org/dr17/data_access/value-added-catalogs/?vac_id=open-cluster-chemical-abundances-and-mapping-catalog`

Table 4.3: A summary of the individual stellar data included in the DR17 OCCAM VAC

Label	Description
CLUSTER	The associated open cluster
2MASS ID	Star ID from 2MASS survey
LOCATION_ID[a]	From APOGEE DR16
GLAT	Galactic latitude
GLON	Galactic longitude
FE_H[a]	[Fe/H]
FE_H_ERR[a]	Uncertainty in FE_H
VHELIO_AVG[a]	Heliocentric radial velocity
VSCATTER[a]	Scatter in APOGEE RV measurements
PMRA[b]	Proper motion in right ascension
PMDEC[b]	Proper motion in declination
PMRA_ERR[b]	Uncertainty in PMRA
PMDEC_ERR[b]	Uncertainty in PMDEC
RV_PROB	Membership probability based on RV (This study)
FEH_PROB	Membership probability based on FE_H (This study)
PM_PROB[c]	Membership probability based on PM (This study)
CG_PROB	Membership probability from Cantat-Gaudin et al. (2018)

[a] Taken directly from APOGEE DR17.

[b] From *Gaia* EDR3.

[c] Negative values indicate the star is outside the adopted cluster radius, while '2' indicates the star failed our PM membership analysis, but is a member in Cantat-Gaudin et al. (2020).

4.2 Results

4.2.1 The Galactic Metallicity Gradient

With the large, uniform sample of open cluster data from APOGEE DR17, we are well positioned to more reliably characterize and report Galactic abundance gradients for 16 chemical species. Figure 4.2 shows [Fe/H] versus both R_{guide} (top panel) and R_{GC} (bottom panel) for our final sample of 85 open clusters. In both cases we use a two-function gradient, where the gradient is described with two linear functions and where

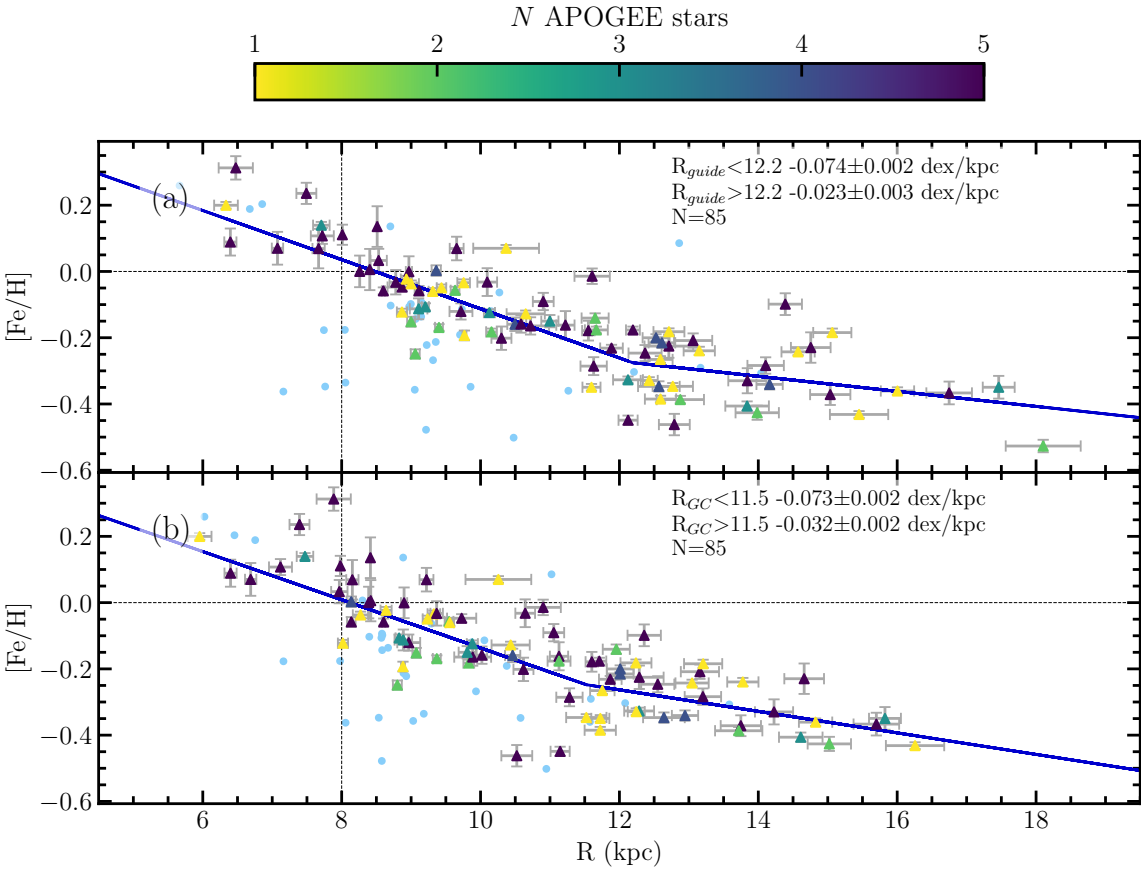

Figure 4.2: Metallicity ([Fe/H]) gradients from the full high quality sample mapped as a function of guiding radius (R_{guide} ; *top panel*) and current radius (R_{GC}; *bottom panel*), along with a bilinear fit as in Donor et al. (2020). Clusters flagged as potentially unreliable are shown as light blue circles. The color bar indicates the number of OCCAM member stars per cluster, saturating at five.

the intersection point of the two lines is also allowed to be a free parameter. We use the fitting procedures described in OCCAM-IV, which uses a maximum likelihood method to fit the data, and the *emcee* python package (Foreman-Mackey et al. 2013) to estimate the fit errors. We assume a 5% error on the distance to each cluster, as (Cantat-Gaudin et al. 2020) did not include distance errors, and these are taken into account in the fitting procedure. We denote the gradient with radius less than the intersection point (hereafter known as the "knee") as the inner gradient and the gradient with radius greater than the knee as the outer gradient. This knee is likely a product of interactions between open clusters and the Galactic disk, where those which are pushed outward are more likely to survive than those which move inward. The Milky Way disk is a dynamic environment, therefore an open cluster which interacts more frequently with the Milky Way structures, e.g., spiral arms or Giant Molecular clouds, will have a higher likelihood to be broken apart than those which are pushed into orbits which spend more time in the outer edges of the Milky Way. We find an inner gradient of -0.074 ± 0.002 dex/kpc for R_{guide}, and a nearly identical inner gradient of -0.073 ± 0.002 for R_{GC}. Meanwhile, the outer gradients for the two cases are: d[Fe/H]/$R_{guide} = -0.023 \pm 0.003$ dex/kpc and d[Fe/H]/$R_{GC} = -0.032 \pm 0.002$ dex/kpc, with the knee located at 12.2 ± 0.12 kpc and 11.5 ± 0.09 kpc, respectively. For completeness, we also fit the open cluster data from Figure 4.2 with a single linear function, which is recorded in Table 4.4, along with the two-function fit and the number of clusters used to calculate both fits (N).

Table 4.4: OCCAM DR17 [Fe/H] Gradients

Selection	Type	Gradient (dex kpc^{-1})	Knee (kpc)	N
d[Fe/H]/dR_{GC}				
Inner	Knee	-0.073 ± 0.002	11.5 ± 0.09	85
Outer	Knee	-0.032 ± 0.002	11.5 ± 0.09	85
All	Linear	-0.055 ± 0.001		85
Age ≤ 0.4	Linear	-0.052 ± 0.003		15
$0.4 <$ Age ≤ 0.8	Linear	-0.059 ± 0.003		17
$0.8 <$ Age ≤ 2.0	Linear	-0.059 ± 0.002		29
Age > 2.0	Linear	-0.052 ± 0.002		22
d[Fe/H]/dR_{Guide}				
Inner	Knee	-0.074 ± 0.002	12.2 ± 0.12	85
Outer	Knee	-0.023 ± 0.003	12.2 ± 0.12	85
All	Linear	-0.056 ± 0.001		85
Age ≤ 0.4	Linear	-0.045 ± 0.003		15
$0.4 <$ Age ≤ 0.8	Linear	-0.058 ± 0.003		17
$0.8 <$ Age ≤ 2.0	Linear	-0.065 ± 0.002		27
Age > 2.0	Linear	-0.049 ± 0.002		22

4.2.2 Galactic Trends for Other Elements

4.2.2.1 $\alpha-$Elements – O, Mg, Si, S, Ca, Ti

The Galactic abundance ratio trends for six α-elements (O, Mg, Si, S, Ca, and Ti) over iron versus R_{guide} are shown in Figure 4.3, these slopes are also reported in Table 4.5, along with the slopes calculated with R_{GC}. We find positive slopes for all studied [α/Fe] abundances but note a significant scatter among the [S/Fe] values and the large uncertainty in the cluster [Ti/Fe] values. The positive trend with respect to [Fe/H] is an indication of the types of enrichment processes that have dominated in different regions of the Milky Way. Evidently, the interior regions of the Milky Way have had more enrichment from Fe-peak dominated events (Type 1a SN) than regions which are farther out. Since Type 1a and Type II supernovae occur on different time scales this implies that the interior of the Milky Way has existed long enough to be enriched by both types of supernovae whereas the outer regions have primarily only been enriched by alpha-enriched ejecta (Type II SN). There are no significant differences between the best fit slopes calculated using either R_{guide} or R_{GC}.

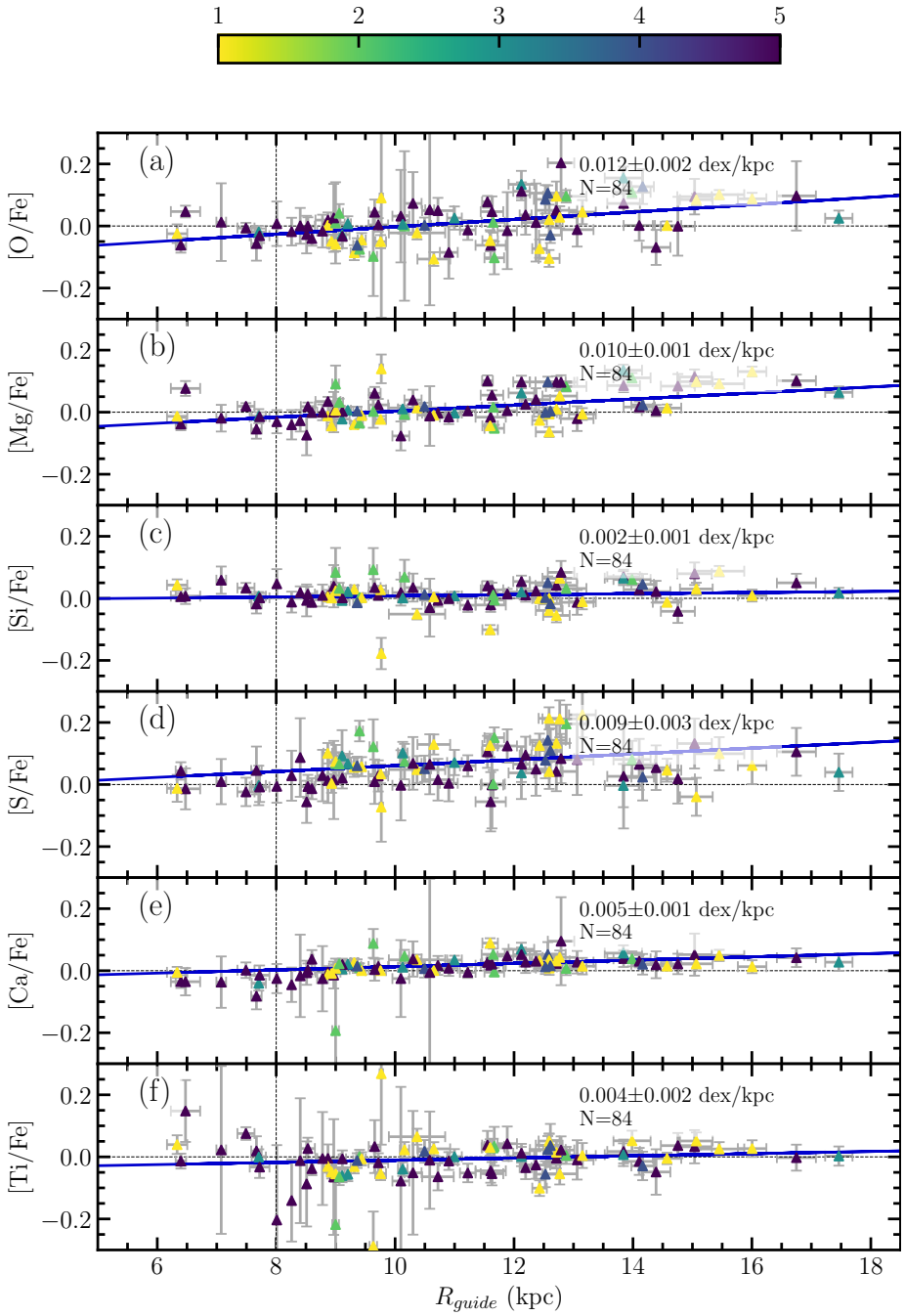

Figure 4.3: The [X/Fe] versus R_{guide} trend for the α-elements. As before the color bar indicates number of member stars, saturating at five, and light blue circles represent clusters with high uncertainty in that element.

Table 4.5: OCCAM DR17 Abundance Gradients

Age range	All Clusters	N	All Clusters[a]	N	Age ≤ 0.4	N	$0.4 <$ Age ≤ 0.8	N	$0.8 <$ Age ≤ 2.0	N	Age > 2.0	N
R range	All R		R < 14 kpc		R < 16 kpc		R < 16 kpc		R < 16 kpc		R < 16 kpc	
Gradient	(dex kpc^{-1})		(dex kpc^{-1})		(dex kpc^{-1})		(dex kpc^{-1})		(dex kpc^{-1})		(dex kpc^{-1})	
Gradients for R_{GC}												
d[O/Fe]/dR_{GC}	$+0.014 \pm 0.002$	84	$+0.015 \pm 0.002$	73	-0.000 ± 0.004	15	$+0.014 \pm 0.007$	17	$+0.009 \pm 0.004$	29	$+0.010 \pm 0.004$	22
d[Mg/Fe]/dR_{GC}	$+0.011 \pm 0.001$	84	$+0.008 \pm 0.001$	73	$+0.001 \pm 0.003$	15	$+0.002 \pm 0.003$	17	$+0.007 \pm 0.002$	29	$+0.012 \pm 0.003$	22
d[Si/Fe]/dR_{GC}	$+0.002 \pm 0.001$	84	$+0.001 \pm 0.001$	73	-0.003 ± 0.003	15	-0.013 ± 0.004	17	$+0.001 \pm 0.002$	29	$+0.002 \pm 0.003$	22
d[S/Fe]/dR_{GC}	$+0.010 \pm 0.003$	84	$+0.017 \pm 0.004$	73	$+0.012 \pm 0.007$	15	$+0.014 \pm 0.011$	17	$+0.010 \pm 0.006$	29	$+0.013 \pm 0.008$	22
d[Ca/Fe]/dR_{GC}	$+0.005 \pm 0.001$	84	$+0.007 \pm 0.002$	73	$+0.006 \pm 0.003$	15	$+0.011 \pm 0.004$	17	$+0.004 \pm 0.003$	29	$+0.005 \pm 0.004$	22
d[Ti/Fe]/dR_{GC}	$+0.004 \pm 0.002$	84	$+0.003 \pm 0.003$	73	$+0.002 \pm 0.005$	15	$+0.015 \pm 0.008$	17	-0.003 ± 0.004	29	$+0.005 \pm 0.006$	22
d[V/Fe]/dR_{GC}	-0.012 ± 0.008	64	$+0.028 \pm 0.011$	58	$+0.037 \pm 0.016$	14	$+0.014 \pm 0.031$	17	$+0.009 \pm 0.017$	29	-0.024 ± 0.020	22
d[Cr/Fe]/dR_{GC}	-0.003 ± 0.004	76	-0.002 ± 0.005	65	$+0.000 \pm 0.008$	15	$+0.006 \pm 0.012$	17	-0.009 ± 0.006	29	-0.008 ± 0.008	22
d[Mn/Fe]/dR_{GC}	-0.007 ± 0.002	82	-0.019 ± 0.002	71	-0.009 ± 0.004	14	$+0.002 \pm 0.004$	17	-0.008 ± 0.003	29	-0.008 ± 0.004	22
d[Co/Fe]/dR_{GC}	-0.006 ± 0.005	62	-0.015 ± 0.007	56	-0.014 ± 0.011	12	-0.040 ± 0.027	14	-0.014 ± 0.011	29	-0.004 ± 0.011	22
d[Ni/Fe]/dR_{GC}	-0.000 ± 0.001	84	-0.003 ± 0.002	73	-0.007 ± 0.003	15	$+0.004 \pm 0.004$	17	-0.003 ± 0.002	29	-0.002 ± 0.003	22
d[Na/Fe]/dR_{GC}	-0.021 ± 0.006	66	-0.031 ± 0.008	56	-0.040 ± 0.014	15	-0.021 ± 0.022	17	-0.025 ± 0.011	29	-0.014 ± 0.013	22
d[Al/Fe]/dR_{GC}	$+0.009 \pm 0.002$	82	$+0.005 \pm 0.003$	71	-0.001 ± 0.005	15	-0.005 ± 0.005	17	$+0.008 \pm 0.004$	29	$+0.008 \pm 0.006$	22
d[K/Fe]/dR_{GC}	$+0.017 \pm 0.003$	80	$+0.017 \pm 0.004$	69	$+0.003 \pm 0.008$	14	$+0.027 \pm 0.011$	17	$+0.015 \pm 0.006$	29	$+0.003 \pm 0.009$	22
d[Ce/Fe]/dR_{GC}	$+0.022 \pm 0.006$	69	$+0.044 \pm 0.009$	60	$+0.034 \pm 0.016$	12	$+0.045 \pm 0.027$	14	$+0.035 \pm 0.012$	29	$+0.056 \pm 0.014$	21
Gradients for R_{guide}												
d[O/Fe]/dR_{guide}	$+0.012 \pm 0.002$	84	$+0.013 \pm 0.002$	73	$+0.002 \pm 0.003$	15	$+0.016 \pm 0.008$	17	$+0.011 \pm 0.005$	27	$+0.008 \pm 0.003$	22
d[Mg/Fe]/dR_{guide}	$+0.010 \pm 0.001$	84	$+0.008 \pm 0.001$	73	$+0.002 \pm 0.003$	15	$+0.005 \pm 0.003$	17	$+0.003 \pm 0.002$	27	$+0.010 \pm 0.002$	22
d[Si/Fe]/dR_{guide}	$+0.002 \pm 0.001$	84	$+0.000 \pm 0.002$	73	-0.002 ± 0.002	15	-0.013 ± 0.004	17	-0.000 ± 0.003	27	$+0.007 \pm 0.003$	22
d[S/Fe]/dR_{guide}	$+0.009 \pm 0.003$	84	$+0.018 \pm 0.004$	73	$+0.009 \pm 0.006$	15	$+0.016 \pm 0.012$	17	$+0.013 \pm 0.007$	27	$+0.013 \pm 0.007$	22
d[Ca/Fe]/dR_{guide}	$+0.005 \pm 0.001$	84	$+0.008 \pm 0.002$	73	$+0.005 \pm 0.003$	15	$+0.009 \pm 0.004$	17	$+0.005 \pm 0.003$	27	$+0.007 \pm 0.003$	22
d[Ti/Fe]/dR_{guide}	$+0.004 \pm 0.002$	84	$+0.002 \pm 0.003$	73	$+0.003 \pm 0.004$	15	$+0.014 \pm 0.008$	17	-0.006 ± 0.005	27	$+0.004 \pm 0.006$	22
d[V/Fe]/dR_{guide}	-0.011 ± 0.008	64	$+0.038 \pm 0.011$	58	$+0.024 \pm 0.014$	14	$+0.037 \pm 0.031$	17	$+0.013 \pm 0.018$	27	-0.016 ± 0.018	22
d[Cr/Fe]/dR_{guide}	-0.003 ± 0.003	76	-0.001 ± 0.005	65	-0.000 ± 0.007	15	$+0.008 \pm 0.013$	17	-0.006 ± 0.008	27	-0.007 ± 0.008	22
d[Mn/Fe]/dR_{guide}	-0.007 ± 0.002	82	-0.011 ± 0.002	71	-0.007 ± 0.003	14	$+0.002 \pm 0.005$	17	-0.012 ± 0.003	27	-0.008 ± 0.004	22
d[Co/Fe]/dR_{guide}	-0.007 ± 0.005	62	-0.023 ± 0.007	56	-0.010 ± 0.009	12	-0.069 ± 0.033	14	-0.038 ± 0.014	27	-0.008 ± 0.009	22
d[Ni/Fe]/dR_{guide}	-0.001 ± 0.001	84	-0.004 ± 0.002	73	-0.006 ± 0.002	15	$+0.003 \pm 0.004$	17	-0.006 ± 0.003	27	$+0.001 \pm 0.003$	22
d[Na/Fe]/dR_{guide}	-0.020 ± 0.006	66	-0.035 ± 0.008	56	-0.030 ± 0.012	15	-0.022 ± 0.022	17	-0.032 ± 0.013	27	-0.013 ± 0.010	22
d[Al/Fe]/dR_{guide}	$+0.009 \pm 0.002$	82	$+0.005 \pm 0.003$	71	$+0.001 \pm 0.004$	15	-0.001 ± 0.006	17	$+0.008 \pm 0.004$	27	$+0.008 \pm 0.005$	22
d[K/Fe]/dR_{guide}	$+0.016 \pm 0.003$	80	$+0.017 \pm 0.004$	69	$+0.004 \pm 0.007$	14	$+0.029 \pm 0.011$	17	$+0.014 \pm 0.008$	27	$+0.007 \pm 0.008$	22
d[Ce/Fe]/dR_{guide}	$+0.024 \pm 0.006$	69	$+0.051 \pm 0.010$	60	$+0.029 \pm 0.013$	12	$+0.047 \pm 0.027$	14	$+0.050 \pm 0.014$	27	$+0.028 \pm 0.012$	21

[a]While not explicitly discussed in text we report the gradient cut at 14kpc in order to easily compare to previous work.

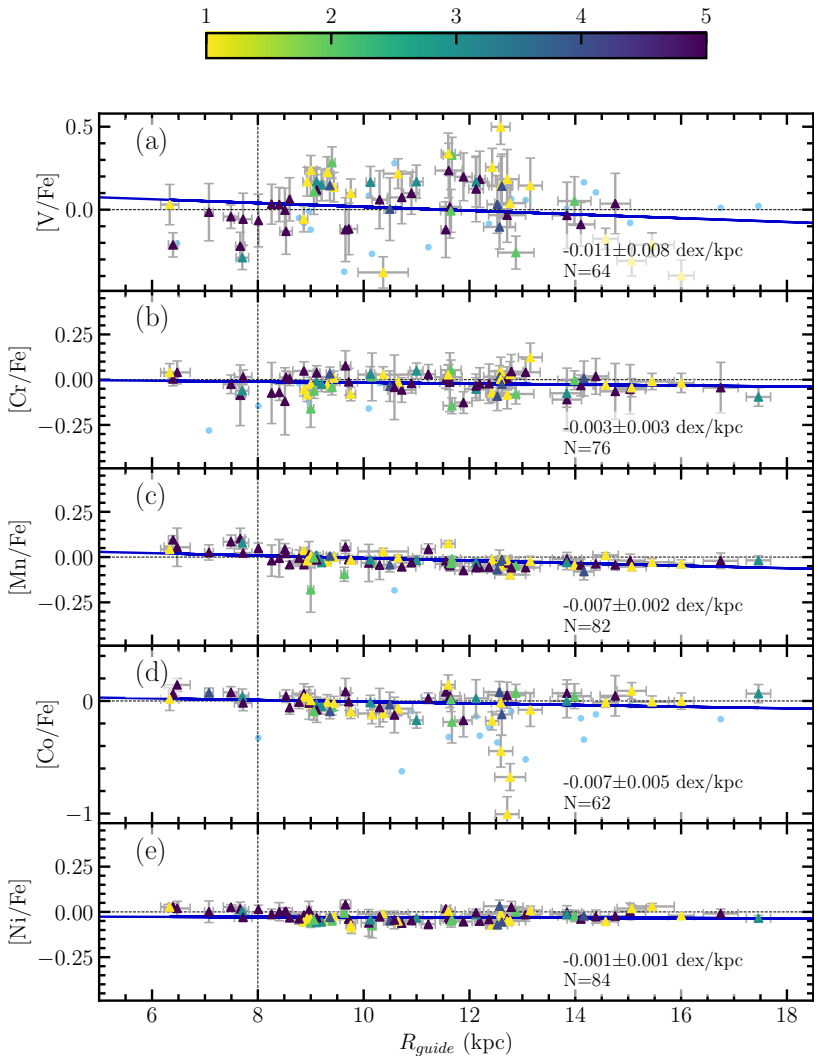

Figure 4.4: Same as Figure 4.3, but for the iron-peak elements.

4.2.2.2 Iron-Peak Elements – V, Cr, Mn, Co, Ni

In Figure 4.4, we investigate the Galactic trends versus R_{guide} of the iron-peak element ratios included in DR17 (V, Cr, Mn, Co, and Ni).[2] The gradients for iron-peak elements over iron all show negative, shallow trends (Table 4.5) with vanadium having the steepest gradient value of all at -0.012 ± 0.008 dex/kpc, although this is still relatively flat. The

[2]As discussed in Abdurro'uf et al. (2022) and Holtzman et al. (*in prep*), the APOGEE DR17 pipeline analysis did not yield sufficiently reliable abundance measurements for the element copper.

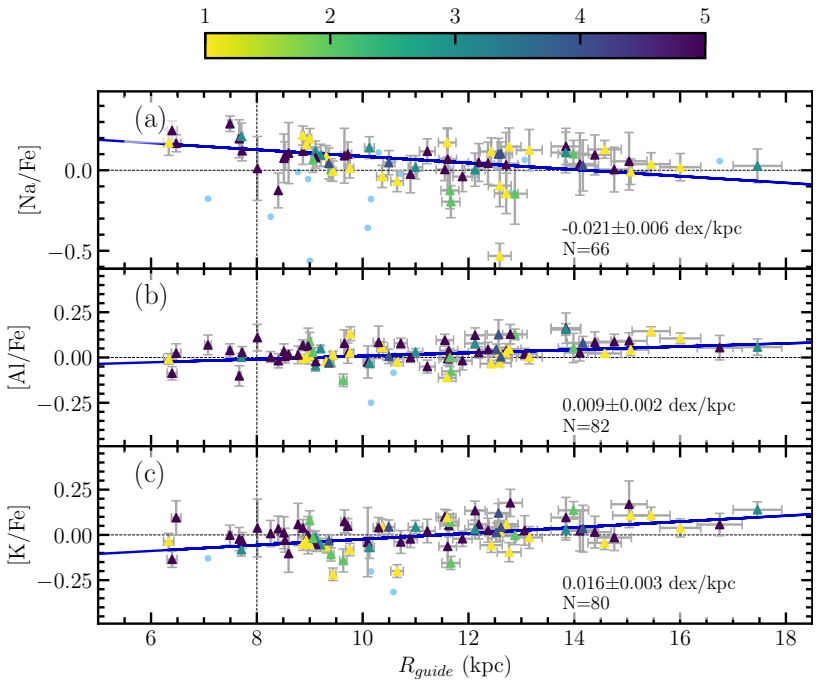

Figure 4.5: Same as Figure 4.3 but for the "odd-z" elements.

cluster values for [V/Fe] also have the largest scatter of the iron-peak elements, however, [Co/Fe] also has three significant outliers: the clusters FSR 0716 ([Co/Fe] = −0.45 dex), FSR 1113 ([Co/Fe] = −0.68 dex) and Haffner 4 ([Co/Fe] = −1.01 dex), which all only have one stellar member in our sample.

4.2.2.3 Odd-Z Elements – Na, Al, K

The abundance gradients with respect to R_{guide} for the three "odd-z" elements: Na, Al, and K are plotted in Figure 4.5, and recorded in Table 4.5 for both R_{guide} and R_{GC}. We report similar positive trends for Al and K, but a steep negative gradient for Na. The single one-star outlier for [Na/Fe] corresponds to the open cluster NGC 136.

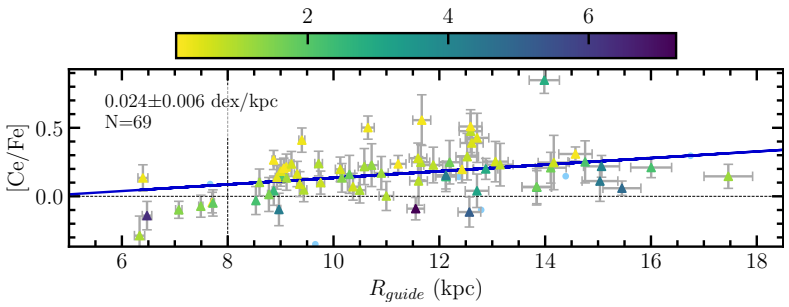

Figure 4.6: The Galactic abundance trend for cerium. The points are colored by their age in Gyrs.

4.2.2.4 The Neutron Capture Element Ce

With the availability of reliable abundances for the s-process element Ce, obtained automatically by the ASPCAP pipeline in DR17, we are now able to investigate the abundance gradient of Ce with 69 open clusters in our sample. In Figure 4.6, we fit [Ce/Fe] abundance versus R_{guide} and find a positive gradient of 0.024 ± 0.006 dex/kpc. In Table 4.5, we also report the slope with respect to R_{GC} and find a value of 0.022 ± 0.006 dex/kpc.

4.2.3 The Evolution of Galactic Abundance Gradients

4.2.3.1 Iron

One of the important questions in chemical evolution models is how the Galactic metallicity gradients have evolved over time. Fortunately, the size of our sample lends itself to investigating this question. The open cluster sample studied here can be split into four age bins, divided at 400 Myrs, 800 Myrs, and 2 Gyrs, identical to the bins chosen in OCCAM-IV, although in this study we use the open cluster ages derived in Cantat-Gaudin et al. (2020).

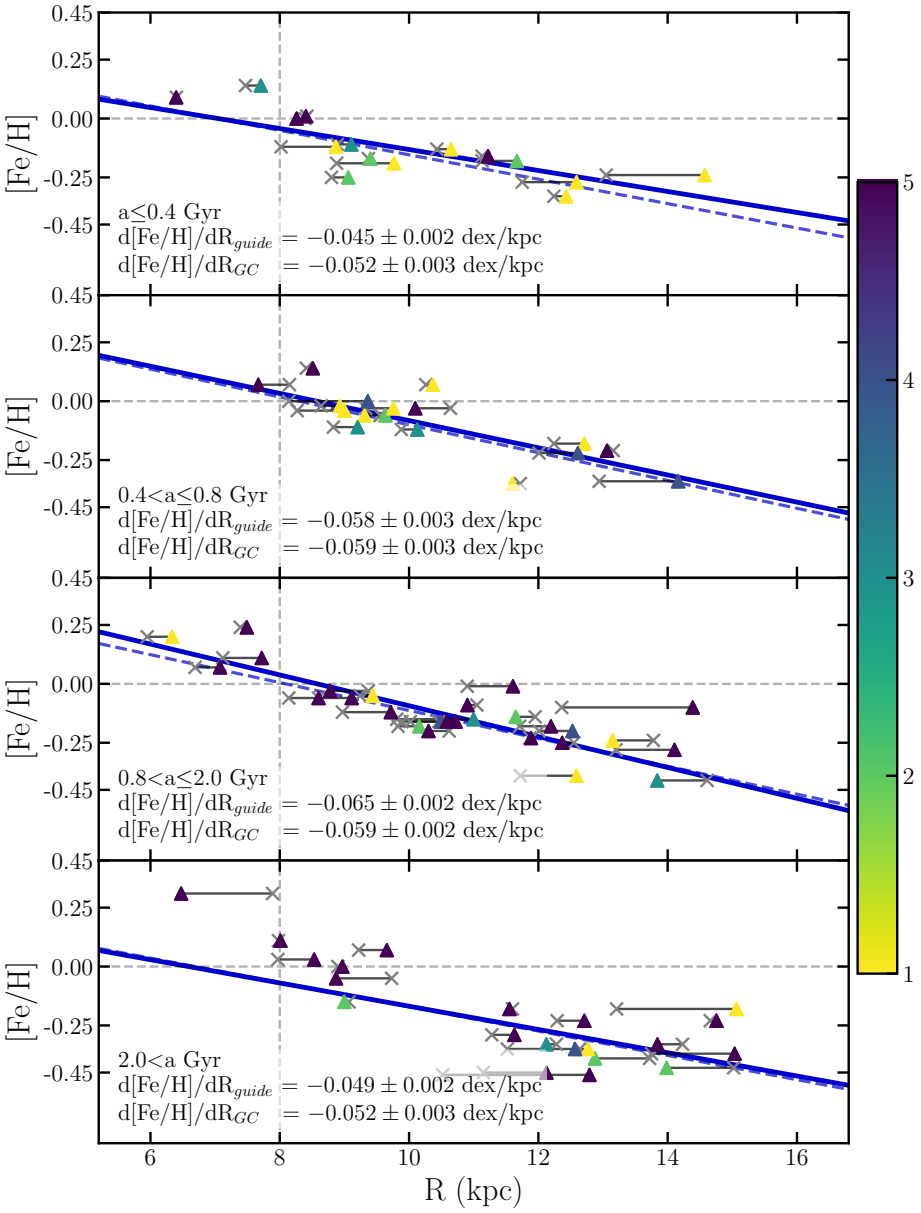

Figure 4.7: The Galactic [Fe/H] versus radius trend in four age bins. Gray 'X's represent the R_{GC} of the cluster, while the colored triangles show R_{guide}, both of these values are connected with a thin grey line for each cluster. The solid line shows the [Fe/H] versus R_{guide} trend, and the dashed line is the trend for R_{GC}.

In Figure 4.7, we plot R_{guide} and R_{GC} versus metallicity for each age bin, showing only clusters with both R_{GC} and $R_{guide} < 16$ kpc. The gradients shown in the figure, however, are calculated with all clusters located within that region (thus the number of

clusters changes between the R_{GC} and R_{guide} fits). This gives a sample of 73 clusters for the R_{guide} plots and a sample of 76 clusters for the R_{GC}. Two sets of symbols are used in Figure 4.7: colored triangles denote guiding center radii while galactocentric radii are marked with gray $\times$; horizontal bars connect the two radii values for the same cluster. The slope of the gradient calculated with respect to R_{guide} is shown as a solid line, and the slope calculated with R_{GC} is represented as a dashed line. The slopes calculated for each age bin and the number of clusters used for each fit are recorded in Table 4.4.

As can be seen in Figure 4.7, the gradients calculated with R_{GC} appear to remain relatively constant between the four age bins, with the first and the fourth bins showing relatively shallow slopes and the two middle bins having identical slopes. The gradients calculated with R_{guide} seem to show a more constant transition from young to old clusters up until the final age bin, wherein the slope becomes significantly shallower. Additionally, we can see in the last two panels of Figure 4.7 (i.e,. the two older age bins), that on average the difference between a cluster's R_{GC} and R_{guide} is larger than in the first two age bins (i.e., the younger two age bins). This suggests that as the clusters have had more time to be affected by interactions in the Galaxy, e.g asymmetric drift, their orbits have become more elliptical. Plus, a potential survivor bias in the older cluster samples (clusters which move inward are significantly more likely to be broken apart by interactions with the Milky Way than those which move outward) and/or possible radial migration of clusters could have affected the gradients.

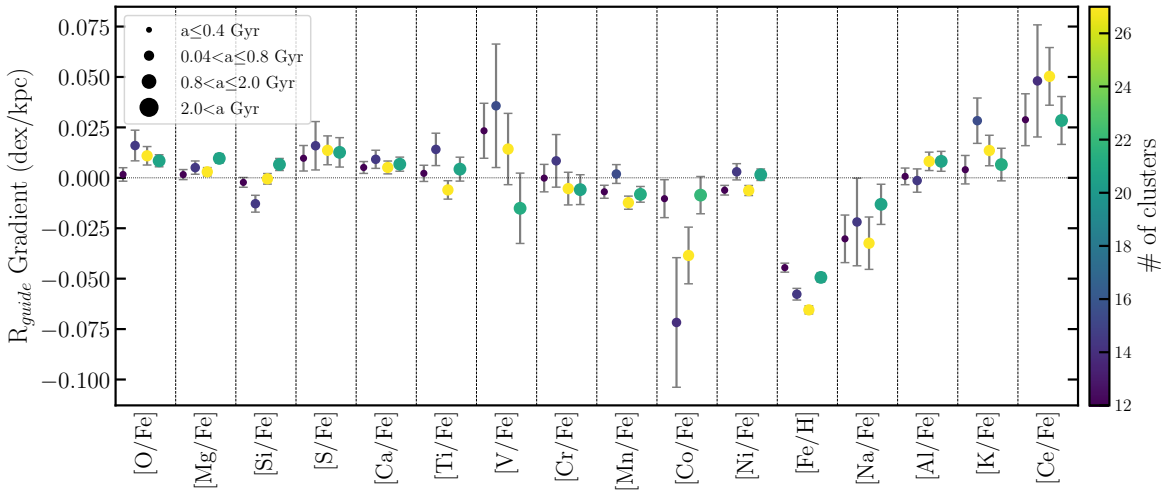

Figure 4.8: The slopes of each elemental gradient in four age bins (as in Figure 4.7), for R_{guide}. Point size increases with age, and the color indicates the number of clusters included in the gradient measurement.

4.2.3.2 [X/Fe]

To understand the evolution in the radial gradients of elements other than iron, we split the cluster sample into the same four age bins as in §4.3.4.1 and fit each gradient as in Figure 4.7. Fit parameters for all elements measured both with R_{guide} and with R_{GC} are reported in Table 4.5. In Figure 4.8, we also show the slopes (d[X/Fe]/dR_{guide}) for all four age bins and each of the 16 elements (where, for iron, we show the abundance ratio [Fe/H]); this figure is comparable to Figure 14 in OCCAM-IV. We note that, as explained in §4.3.4.1, all clusters used in the fit have a radius (R_{guide} or R_{GC}) less than 16 kpc.

We find no convincing trends through the four age bins in α elements. While there could be a slight trend in [Mg/Fe], with oldest clusters perhaps showing a steeper slope than younger clusters, the changes between samples are roughly as significant as the uncertainties.

Both [Cr/Fe] and [Ni/Fe] hover around a flat gradient throughout all four age bins, and the gradients of [V/Fe] and [Cr/Fe] both have large uncertainties in their measurements, which makes it difficult to determine any evolutionary trends. Additionally, we do not find a significant trend for [Mn/Fe], which breaks with previous APOGEE-based DR16 results presented in OCCAM-IV.

In the odd-Z elements, the gradient for [Na/Fe] seems to have an increasingly negative trend in R_{guide} as clusters get younger, though within the sizeable uncertainty the trend may be less significant. Finally for cerium, the uncertainties in the DR17 measurements are still too large to measure a significant trend over time.

4.3 Discussion

4.3.1 Comparison to OCCAM-IV sample

Between this sample and OCCAM-IV, 111 clusters can be found in both samples, 42 new clusters were added to this sample, and 17 clusters were not recovered, including two "high quality" clusters: Berkeley 44 and NGC 2355. With updated *Gaia* EDR3 data, the 2D Gaussian fit to the kernel convolution in proper motion space was narrower by enough that the APOGEE star now fell further than 3σ from the distribution. For Berkeley 44, the star that was included in OCCAM-IV is now slightly outside of the 2D Gaussian fit to the *Gaia* EDR3 proper motions. It is also not reported as a member in CG18. For NGC 2355, the star that was included in OCCAM-IV is considered a member

in CG18 with a membership probability of 70%, but using updated EDR3 proper motions, the 2D Gaussian fit was more narrow and thus this star was rejected by our pipeline.

Additionally, there were three "high-quality" clusters in OCCAM-IV which were demoted to being flagged as "potentially unreliable" in this sample (SAI 16, BH 211, and Basel 11b). BH 211 failed the visual quality check, and both Basel 11b and SAI 16 had only two potential members with conflicting [Fe/H] values. However, there are seven clusters (Berkeley 91, FSR 0496, King 8, NGC 136, NGC 2202, Saurer 1, and Teutsch 10) which were previously marked "0" or "potentially unreliable" that are now included in the "high quality" sample due to the addition of new data.

For designated "high quality" clusters in common between this sample and OCCAM-IV, a total of 66 clusters, Figure 4.9 shows the change in [Fe/H] between APOGEE DR16 and DR17. The median change, measured to be -0.020, is well within the measured scatter of 0.033, although this scatter seems to be due mostly to the lowest metallicity clusters ([Fe/H] $\lesssim -0.4$). A visual inspection of the plot suggests that closer to Solar [Fe/H] there may be a real, albeit slight offset from DR16. However, this small offset is easily explainable by the significant changes to the APOGEE pipeline. The single outlier in Figure 4.9 with a Δ[Fe/H]= 0.18 is NGC 752.

Figure 4.10 shows the change in OCCAM measured cluster abundances for 14 elements from APOGEE DR16 to DR17, plotted as a function of their reported DR17 abundance. These differences are due to pipeline and membership changes. Copper and phosphorus are not included because of unsuccessful measurements in DR17 (Abdurro'uf et al. 2022, Holtzman et. al, *in prep*). Cerium is also not included in Figure 4.10 because the values reported in DR16 were not considered particularly reliable (Jönsson et al.

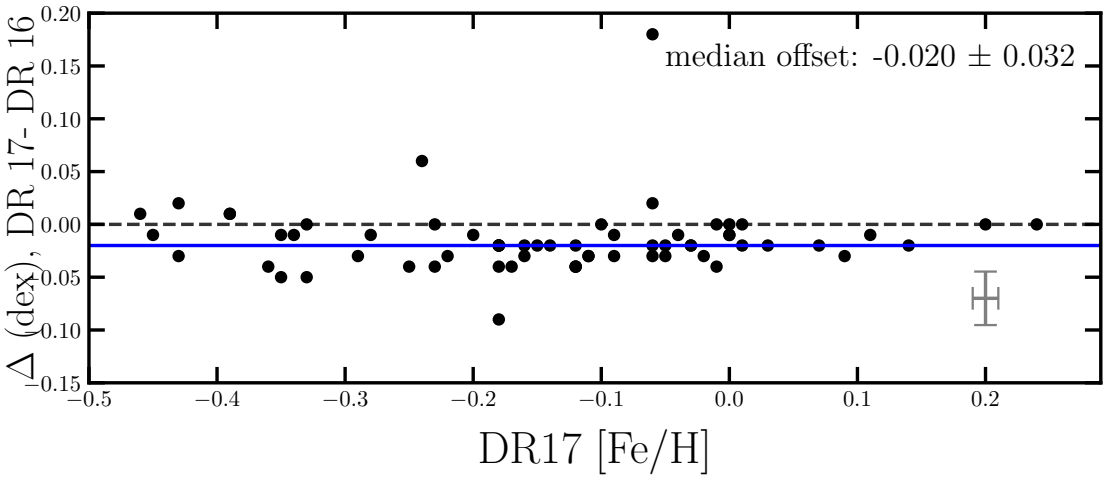

Figure 4.9: Comparing the DR17 and DR16 [Fe/H] abundances. The measured median offset is shown as a solid blue line. A characteristic error bar is shown for reference.

2020). The measured median offset is within the measured scatter for all 14 abundances investigated. It is worth commenting on the particularly large scatter, and potential trend, for vanadium and sodium. Vanadium is considered less reliable in both DR16 and DR17; sodium is considered reliable in DR17 but less so in DR16 (Jönsson et al. 2020).

4.3.2 Comparison to other surveys

Spina et al. (2021) use data from GALAH+, APOGEE DR16, and *Gaia* to compile a list of 226 open clusters, 134 of which have high-quality spectroscopic data for up to 21 elements. Of these clusters 85 are in common with our sample. We compare our sample to the GALAH sample, much like Figure 4.9, and measure a median offset, (Δ dex, DR17-GALAH) of -0.018 ± 0.046, with two major outliers: King 2 at +0.18 and Berkeley 18 at +0.25, which both only have one member in the GALAH catalog.

In a recent APOGEE study, Sales-Silva et al. (2022) investigated the abundance gradient for the s-process element, Ce, with a detailed abundance analysis of several Ce

II lines from Cunha et al. (2017). They use 218 stellar members of 42 open clusters from the OCCAM-IV sample. In a manner identical to the comparisons above for the OCCAM-IV and GALAH surveys, we compare the [Ce/Fe] abundances for all clusters in common between this sample and the one reported in Sales-Silva et al. (2022). We find not only a systematic shift, but also a sub-solar offset for the cerium abundances between the two samples, both between the open clusters and individual stellar abundances. This shift may be due to BACCHUS, as used by Sales-Silva et al. (2022), not properly excluding CNO blending from targeted lines. We additionally compared to the high-resolution optical follow-up analysis of APOGEE stars in clusters from O'Connell (2017) and O'Connell et al., *in prep*, which gives similar results to (Sales-Silva et al. 2022). Given the possible uncertainties with cerium, we present the DR17 OCCAM results here, but suggest further work is needed to settle this discrepancy.

4.3.3 Comparison of Galactic Abundance Trends

In order to evaluate our reported gradients, we compare them against previous studies in this section. For our metallicity gradient comparisons, we use our full sample of open clusters. However, for the individual abundance gradient comparisons in §4.3.3.2– 4.3.3.5, we use gradients with a cut in radius at 14 kpc (Table 4.5), as the other studies do not have significant clusters beyond 14 kpc.

4.3.3.1 Galactic Metallicity Gradient

Our derived metallicity trend — namely an inner gradient of -0.073 ± 0.002 dex/kpc, outer gradient of -0.032 ± 0.002 dex/kpc, and break at 11.5 kpc for R_{GC} — shows

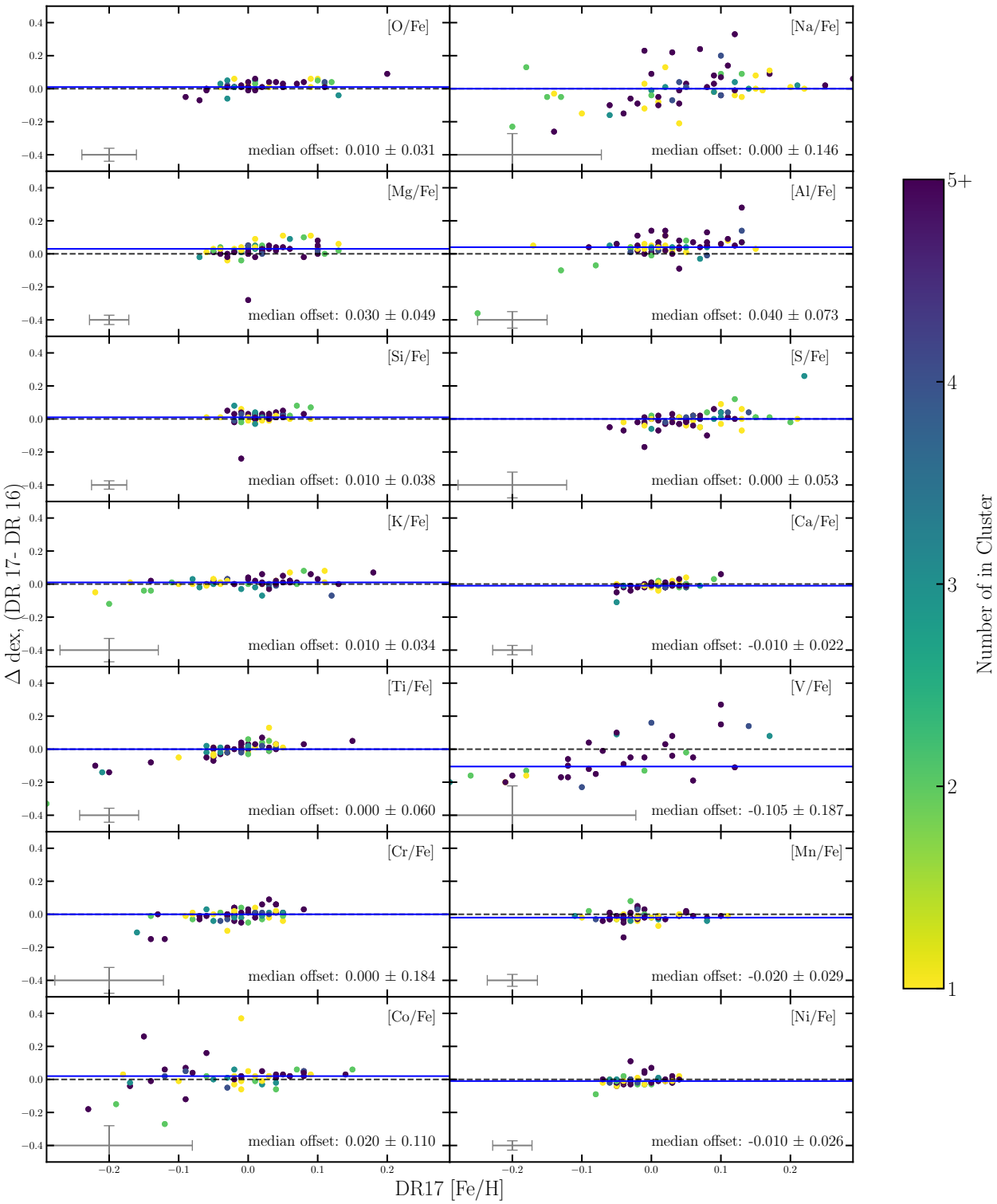

Figure 4.10: A comparison of DR17 versus DR16 for each chemical element in our study. Characteristic error bars, calculated identically to those in Figure 4.9, are indicated in each panel. Median offsets between the DR17 and DR16 values for clusters in common are shown by a blue line, while datapoints are colored by the number of stars in the DR17 cluster.

a very similar inner gradient to that reported in OCCAM-IV (theirs being -0.068 ± 0.004 dex/kpc). However, our measured outer gradient is significantly steeper than the OCCAM-IV value of -0.009 ± 0.011 dex/kpc, and the knee measured here is farther inwards than theirs (13.9kpc). These discrepancies are most likely due to poor coverage of clusters at $R_{GC} > 14$ kpcs in the OCCAM-IV sample, as noted in that study.

The Netopil et al. (2022) study finds an overall linear gradient of -0.058 ± 0.004 dex/kpc, which is only slightly steeper than our measured single linear slope of -0.056 ± 0.001 dex/kpc. They also measure an inner disk ($R_{GC} < 12$ kpc) gradient of -0.058 ± 0.005 dex/kpc which is significantly shallower than our reported values.

Similarly, Spina et al. (2021) measure a linear trend for their sample of open clusters of d[Fe/H]$/R_{GC} = -0.076 \pm 0.009$ dex/kpc and d[Fe/H]$/R_{guide} = -0.073 \pm 0.008$ dex/kpc, for clusters between roughly $6 \leq R \leq 14$ kpc. Both of these slopes are consistent with the present inner gradients of -0.073 ± 0.002 dex/kpc and -0.074 ± 0.002 dex/kpc respectively, however with the additional clusters beyond ~ 14 kpc in this sample, we find a much shallower linear gradient in both R_{GC} and R_{guide} .

4.3.3.2 $\alpha-$Elements – O, Mg, Si, S, Ca, Ti

Our results for the $\alpha-$elements are largely in agreement with those of OCCAM-IV, with an exception for the gradient in [Ca/Fe] which, in the DR17 sample is significantly flatter (0.007 ± 0.002 dex/kpc) than was reported with the DR16 sample (0.012 ± 0.001 dex/kpc). Our gradients for silicon and titanium (d[Si/Fe]$/dR_{GC} = +0.001 \pm 0.001$ dex/kpc and d[Ti/Fe]$/dR_{GC} = 0.003 \pm 0.003$ dex/kpc) are also slightly steeper than those

reported in OCCAM-IV (d[Si/Fe]$/dR_{GC} = -0.001 \pm 0.001$ dex/kpc and d[Ti/Fe]$/dR_{GC} = 0.000 \pm 0.002$ dex/kpc), but they are nearly the same within the measured uncertainties.

Spina et al. (2021) find a comparatively steep gradient in [O/Fe] vs R_{guide} of 0.032 ± 0.01 dex/kpc, significantly different from the present measurement of $+0.013 \pm 0.002$ dex/kpc. The steep [O/Fe] vs R_{guide} gradient stands out from other gradients in α elements in Spina et al. (2021), and the reported uncertainty, is larger as well. While Casamiquela et al. (2019) reports a steep gradient for [Si/Fe] versus R_{GC} of 0.022 ± 0.007, similar to the steep [O/Fe] versus R_{GC} gradient from Spina et al. (2021), steep gradients in α-elements are not commonly reported. Indeed, gradients measured for other α-elements (Mg, Si, Ca, and Ti) by Spina et al. (2021) are nearly flat. This also stands in some contrast to the present work as we consistently measure mildly positive gradients in the same elements. This general trend of mildly positive gradients in α-elements is consistent with OCCAM-IV, and previous literature (e.g., Carrera & Pancino 2011, Yong et al. 2012, Reddy et al. 2016) as discussed in OCCAM-IV.

4.3.3.3 Iron-Peak Elements – V, Cr, Mn, Co, Ni

The gradients we reported in Table 4.5 for nickel, cobalt, manganese, and vanadium are in good agreement with those in OCCAM-IV. However, the gradient for [Cr/Fe] measured here (-0.002 ± 0.005 dex/kpc) does deviates slightly from that measured in OCCAM-IV (0.010 ± 0.004 dex/kpc). This seems to be due to minute changes in abundances, particularly in those clusters at radii less than ~ 7 kpc, which affects the gradient and accounts for the discrepancy.

The slopes measured for [Cr/Fe] (-0.003 ± 0.004 dex/kpc) is consistent with the compiled gradient from the OCCASO (Casamiquela et al. 2019), -0.005 ± 0.003 dex/kpc. However, the measured slope for [V/Fe], 0.028 ± 0.011 dex/kpc, is inconsistent with that measured in OCCASO. This discrepancy can easily be accounted for due to the large scatter present in both gradients. Both this study and the OCCASO study also measure a very flat gradient for [Ni/Fe], however the final values (-0.003 ± 0.002 dex/kpc in this sample and 0.002 ± 0.001 dex/kpc in the OCCASO sample) are just outside of the uncertainties.

Finally, the slope from this sample for [Mn/Fe] (-0.011 ± 0.002 dex/kpc) is consistent with that reported in Spina et al. (2021) (-0.012 ± 0.004 dex/kpc). However, the slope reported in this study for the [Ni/Fe] gradient (-0.004 ± 0.002 dex/kpc) is significantly shallower and for the [Co/Fe] gradient (-0.023 ± 0.007 dex/kpc) is significantly steeper than the gradients reported in Spina et al. (2021) (-0.022 ± 0.006 dex/kpc and -0.007 ± 0.007 dex/kpc, respectively).

4.3.3.4 Odd-Z Elements – Na, Al, K

The gradient calculated for [Na/Fe] and [K/Fe] (-0.031 ± 0.006 dex/kpc and 0.017 ± 0.003 dex/kpc) is consistent with those reported in OCCAM-IV. However, the slope of the [Al/Fe] gradient, 0.005 ± 0.003 dex/kpc, is significantly shallower than the slope reported in OCCAM-IV (0.018 ± 0.002 dex/kpc) and entirely inconsistent with the value reported in Spina et al. (2021) (-0.013 ± 0.007 dex/kpc). Additionally, the measured gradient, $d[\mathrm{Na/Fe}]/dR_{guide} = -0.035 \pm 0.008$ dex/kpc, is inconsistent with that measured in Spina et al. (2021) (-0.008 ± 0.010 dex/kpc). However, we note that this sample has a greater

number of clusters at larger distances than the Spina et al. (2021) sample, which acts to flatten the gradient because of the change in slope for clusters beyond the knee. Additionally, the gradient measured by Spina et al. (2021) seems to be dominated by a few [Al/Fe] enhanced clusters in the inner galaxy, which we do not see in our sample. Finally, the OCCAM-IV [Al/Fe] gradient includes a few single-star clusters at low [Al/Fe] which resulted in a steeper measured gradient.

4.3.3.5 The Neutron Capture Element Ce

Shown in Figure 4.6, and reported in Table 4.5, we find a positive cerium abundance gradient of d[Ce/Fe]$/dR_{guide} = 0.024 \pm 0.006$ dex/kpc and d[Ce/Fe]$/dR_{GC} = 0.022 \pm 0.006$ dex/kpc. Comparing these slopes to the gradients calculated in Sales-Silva et al. (2022), their value for d[Ce/Fe]$/dR_{GC}$ of 0.014 ± 0.007 dex/kpc is shallower than the value found here, though much of this discrepancy may be explained by the measurement differences as described in §4.3.2.

4.3.4 Evolution of Galactic Abundance Gradients

4.3.4.1 Iron

One of the key goals of the OCCAM project is to explore the evolution of abundance gradients in the Milky Way. To this end, we find significant evolution in the d[Fe/H]$/dR$ gradients as presented in §4.2.1. This same trend has also been shown in OCCAM-IV, Spina et al. (2021), Sales-Silva et al. (2022), Netopil et al. (2022) and Zhang et al. (2021).

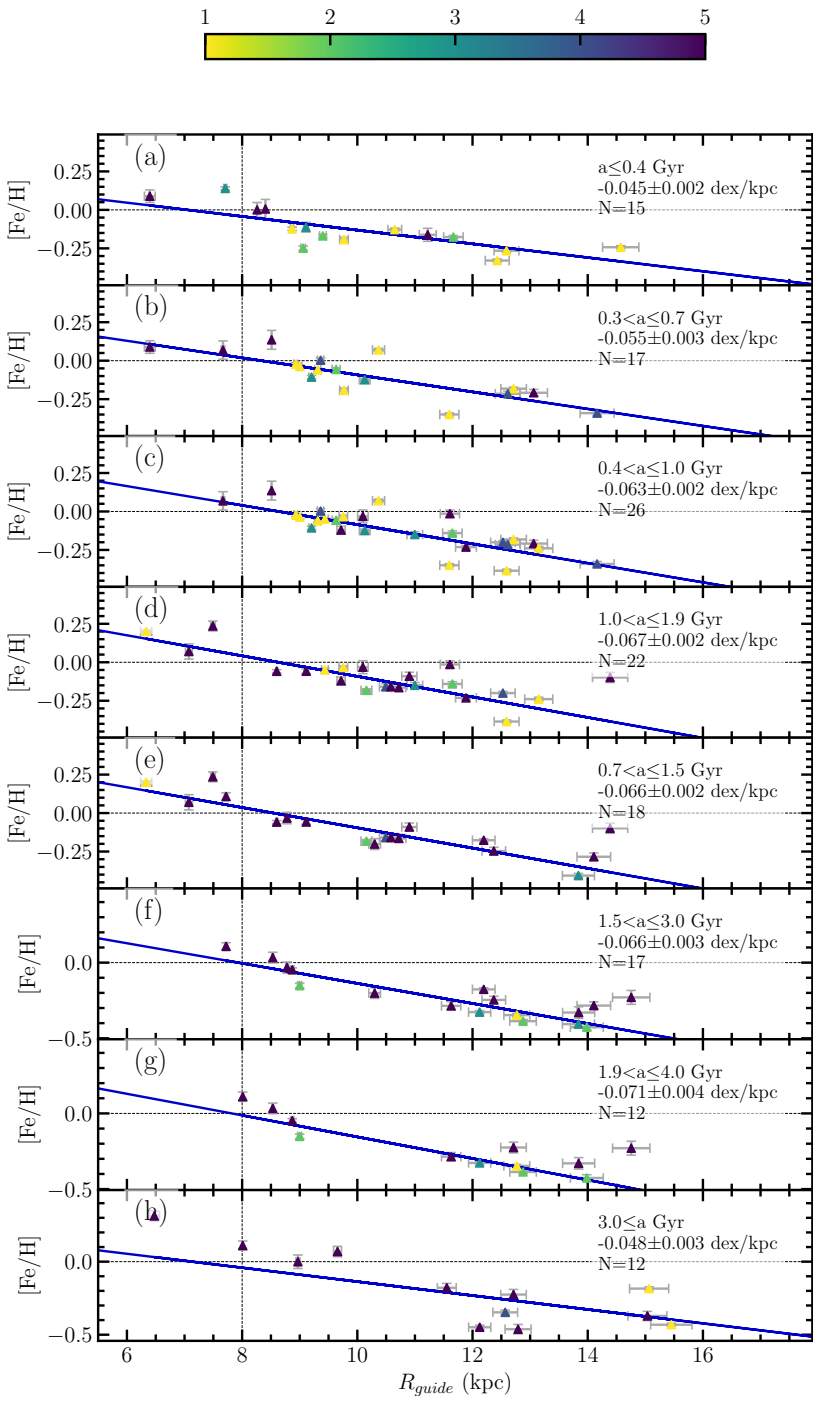

Figure 4.11: The age slopes measured if the age bins used in (Netopil et al. 2022) are adopted.

Netopil et al. (2022) explored the evolution of the [Fe/H] gradient by compiling a sample of 136 open clusters from various studies, including 75 clusters with data from APOGEE DR16, 70 of which are in common with this sample. The details of the compilation are recorded in both Netopil et al. (2016) and Netopil et al. (2022). The latter used their sample to investigate radial migration in open clusters and also measure the age-metallicity gradient with eight overlapping age bins. These age bins span from the youngest clusters (age < 0.4 Gyrs) to clusters with age ≥ 5.2 Gyrs.

To better compare our results to that of Netopil et al. (2022), we divided our sample into their age bins (Fig. 4.11); however, to populate the oldest age bin with more than 10 clusters, we modified the oldest age bin from the Netopil et al. limits $3.0 \geq$ age ≥ 5.2 Gyrs to instead include all clusters with age ≥ 3.0 Gyr.

Comparing to Table 6 in Netopil et al. (2022), the gradients we measure in Figure 4.11 are in good agreement for nearly every age bin, with measurements in 6 of the 8 samples agreeing well within the reported uncertainties. However, in the first age bin, the discrepancy between the two gradients is ~ 0.004 dex/kpc; and for the final age bin the discrepancy is ~ 0.008 dex/kpc. We note that the final age bin is largely affected by two relatively metal poor clusters at $R_{guide} \simeq 12$ kpc, NGC 2243 and Trumpler 5.

Finally, we compare our [Fe/H] evolution results to the thin-disk chemical evolution model of (Chiappini 2009) and the chemo-dynamical simulation of (Minchev et al. 2013; 2014, MCM in Figure 4.12), using the same age bins as Figure 4.7. In the youngest three age bins we notice good agreement for both R_{GC} and R_{guide} trends. The third age bin also shows decent agreement, though there may be a slight offset between the R_{guide} cluster sample and the model results. In the final age bin, both the R_{GC} and R_{guide} cluster

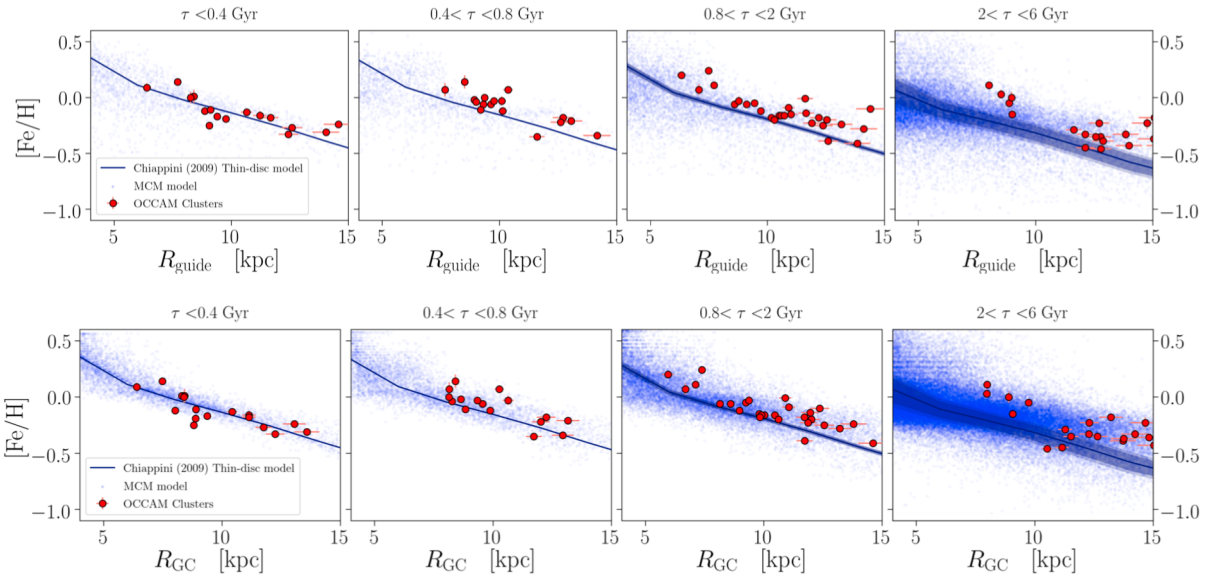

Figure 4.12: The open cluster sample from this study (red dots) overlaid on the models of (Chiappini 2009) (the blue line) and (Minchev et al. 2013; 2014) (blue dots). The plots are split into the same age bins used in Figure 4.7.

sample have a noticeable offset from the models. This could potentially suggest either a real effect that would require a change to the models or that the older open clusters are possibly a biased sample due to which clusters survive to older ages and/or that these old clusters may have undergone migration and migrated outward during their lifetimes (whereas clusters that moved inward in the Milky Way are more likely to be disrupted).

4.3.4.2 [X/Fe]

The evolution of abundance gradients for elements besides iron were explored in §4.2.2. A similar analysis in OCCAM-IV indicated no convincing trends in α elements with time. As in OCCAM-IV, it could be argued that there is a slight trend for [Mg/Fe], with older clusters perhaps showing generally steeper slopes than the younger clusters, but also as in OCCAM-IV the changes between samples are roughly as significant as the uncertainties.

There is very little evolution found for [Cr/Fe] and [Ni/Fe], which is consistent with the OCCAM-IV results. As is the case here, OCCAM-IV found significant uncertainty in the [Cr/Fe] measurements, but the [Ni/Fe] gradients were fairly well determined. OCCAM-IV found a significant trend for [Mn/Fe] with the gradient becoming more negative for younger cluster populations. With the new DR17 data, this trend is no longer present; indeed the new APOGEE results seem to indicate that the younger samples have less negative gradients.

Finally, while we do seem to see an increasingly negative trend in d[Na/Fe]/dR_{guide} as clusters get younger, the uncertainties in the gradients are large. This is roughly consistent with the slopes calculated in OCCAM-IV, though they found a flatter trend with a significantly steeper slope in the oldest age bin that we do not see here.

Chapter 5

APOGEE Globular Clusters

5.1 The APOGEE Globular Cluster Sample

While the power of APOGEE is in probing the dusty regions of the Milky Way, APOGEE has sampled all parts of the Milky Way (disk, Bar/Bulge, and Halo), including other star clusters. Given the usefulness in using open clusters to trace the Galactic disk, we decided to explore whether a more "global" picture of Galactic chemical enrichment could be made if we expanded our sample to include the globular clusters.

Of the 157 globular clusters identified in the Harris catalog, only ∼80 have data from the APOGEE survey within 3σ of the clusters half-light radius (r_h). In an aim to derive a globular cluster sample with a uniform analysis, we used the OCCAM pipeline, described in Chapter 3 with limited modification. We substituted our *Gaia* comparison studies, switching Cantat-Gaudin et al. (2018) for Baumgardt et al. (2019), and used the r_h from Harris (1996) instead of the "visual" radius from Cantat-Gaudin et al. (2020). Using the OCCAM pipeline, we analyzed 72 clusters with 8250 APOGEE stars, where we determined 43 of these clusters to be "high quality" (as described in §3 and OCCAM-IV) and 4964 of the stars are found to be probable members. The analyzed stars and bulk cluster properties can be found in the Appendix (Table B.1 and Table B.2).

For the globular cluster sample, we measure a metallicity spread between -2.29 and -0.19 dex (as compared to $-0.53 \leq [Fe/H] \leq 0.31$ dex for open clusters) and we find a range in Galactocentric radii from 1.4 kpc to 29.8 kpc. We show this sample in Figure 5.1 where, similar to Figure 4.2, we show the metallicity of the sample as a function of both R_{guide} (top) and R_{GC} (bottom). We additionally overplot the open cluster sample as black dots for reference. From Figure 5.1, it is evident that there is little to no overlap or

correlation between the open cluster sample and the globular cluster sample, especially due to the large scatter between the globular clusters. One cluster that *could* follow the open cluster sequence is Palomar 1, the light blue dot located on top of the open cluster distribution at roughly $R_{guide} = 17$ kpc. In previous studies (e.g., Jahandar et al. 2017, Sakari et al. 2011, and references therein), Palomar 1 has been found to be a peculiar globular cluster based on its age (4–6 Gyrs) and chemistry (which is not consistent with other globular clusters nor other halo features, but is consistent with it possibly being an old open cluster). Yet, it has been found to lie around 4 kpc above the Galactic plane which keeps it, precariously, classified as a globular cluster. Given the present sample, it is now possible to additionally investigate the orbital properties of Palomar 1 with new data from *Gaia*, which could be explored in future work.

While these initial results demonstrate that the stellar populations of the Milky Way's disk and halo are distinct chemical populations, and cannot be combined to shown a consistent "global" enrichment history, they still provide a "simplified" globular cluster sample. We hope to explore the individual cluster samples in more detail (e.g., explore the presence of multiple populations and chemical stellar evolution and mixing tracers like [C/N]), as well as the Galactic distributions for these globular clusters in future studies.

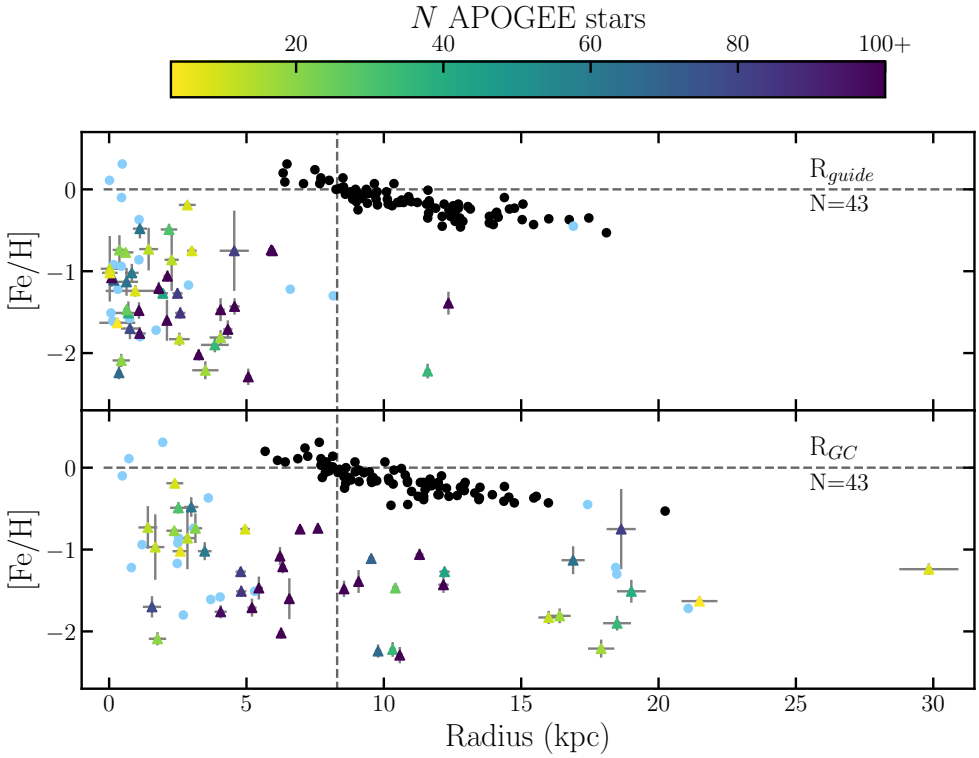

Figure 5.1: Metallicity ([Fe/H]) gradients from the high quality globular cluster sample mapped as a function of guiding radius (R_{guide} ; *top panel*) and current radius (R$_{GC}$; *bottom panel*). The black dots show the open cluster sample for comparison. Clusters flagged as potentially unreliable are shown as light blue circles. The color bar indicates the number of OCCAM member stars per cluster, saturating at 100.

Chapter 6

Conclusions and Future Work

6.1 The Milky Way Disk Abundance Gradients

We present the final APOGEE-2 DR17 OCCAM sample, which consists of 150 open clusters, and 94 that we designate as "high quality". To gain insights into the chemical enrichment history of the Milky Way, we use the high quality sample to measure Galactic abundance gradients in 16 chemical elements and investigate their evolution over four age bins. With clusters spanning roughly 6.0 to 18 kpc, we measure a two-function Galactic radial metallicity trend, with -0.073 ± 0.002 dex/kpc for the inner slope, -0.032 ± 0.002 dex/kpc for the outer slope, and a knee located at 11.5 kpc. In order to account for blurring effects in the clusters orbits, we also calculate the guiding center radii, R_{guide}, of each cluster. By using R_{guide} as the independent variable, we find an inner slope of -0.074 ± 0.002 dex/kpc, an outer slope of -0.023 ± 0.003 dex/kpc, and a knee at 12.2 kpc.

The Galactic radial gradients for the 15 elements measured in this survey are in good agreement with other recent studies (e.g., Reddy et al. 2016, Casamiquela et al. 2019, Donor et al. 2020, Spina et al. 2021). In this work, we find significant (3σ or greater) trends in 9 of the 15 elements, including four of the $\alpha-$elements (O, Mg, S, Ca), all of the odd-Z elements (Na, Al, K), and cerium. We don't find significant gradients in the iron-peak elements, except manganese. We explore the variation in the trends for all elements throughout time, by splitting the open cluster sample into four age bin. We find no significant evolution compared with solar ratios, besides two elements (V and Na) which have large uncertainty in their measurements. This lack of age variation in the gradients points to well-mixed enrichment through the age range covered (10 Myr

– 9 Gyr), which implies that chemical tagging distinct *age* populations may be difficult with these elements, but could be improved with the inclusion of C and N (e.g., Casali et al. 2019, Spoo et al. 2022) for distinct stellar evolutionary phases.

We compare this DR17-based sample to OCCAM-IV and the GALAH sample from Spina et al. (2021) and find no significant differences between the abundances in either case. Additionally, we compare against the cerium abundances derived in Sales-Silva et al. (2022) and find an abundance correlated offset for sub-solar cerium abundances between the BACCHUS analyses and the DR17 ASPCAP-derived values.

We find general agreement in the first three age-bins when we compare to the chemo-dynamical models of Chiappini (2009) and Minchev et al. (2013; 2014), however in the final age bin we do find an offset between the cluster sample and the models. This could be explained by either an offset in the models or, possibly, by a potential survivor bias in the older open cluster sample.

Also, we note that APOGEE DR17 is able to measure Galactic trends for many of the CHNOPS elements, for example, C,N,O, and S, which are important in the astrobiological study of the Galactic habitable zone. In this work, we present the gradients for oxygen and sulfur. The gradients for carbon and nitrogen are not presented here due to stellar evolutionary effects that change stellar surface chemistry due to the dredge up; however, these elements and their correlations with age are explored in Spoo et al. (2022).

6.2 Future Work

While the APOGEE survey provides numerous distinct elements for hundreds of thousands of stars within and around the Milky Way, it is limited in the elements it has available to it. Namely, APOGEE lacks heavy elements known as neutron capture elements, except for Ce, that can help trace the Type 1a and Type II supernovae enrichment history within the Galactic disk. Therefore, follow-up spectra (specifically in the optical regime, where many neutron capture abundances such as Sr, Y, Zr, Ba, La, Ce, Nd, Eu, and Yb can be derived) of known open cluster members are necessary to fully characterize and explore the evolution of abundance gradients of the Milky Way.

Additional work will also be needed to further explore the details of the globular cluster sample. While there may not be any large overlap between the open cluster sample and the globular cluster sample, there is still much to explore in the interior chemical variation *within* individual globular clusters. For example, the presence of multiple populations and identifying chemical mixing tracers (like [C/N]) in stellar populations).

Appendix A

The OCCAM DR17 Open Cluster Sample

This section contains the detailed tables for the APOGEE-based OCCAM DR17 sample of open clusters presented in Chapter 4.1 .

Table A.1: OCCAM DR17 "High Quality" Sample Basic Parameters

Cluster name	Qual flag	l (deg)	b (deg)	R [a] (′)	Age [a] Gyr	R_{GC} [b] (kpc)	R_{Guide} [b] (kpc)	μ_α [c] (mas yr^{-1})	μ_δ [c] (mas yr^{-1})	RV (km s^{-1})	[Fe/H] (dex)	Num stars
Ruprecht 147	1	20.9297	−12.7606	78.2	3.020	7.98	8.01	-0.89 ± 0.09	-26.73 ± 0.08	$+42.1 \pm 0.9$	$+0.11 \pm 0.03$	35
NGC 6705	1	27.3031	−2.7726	8.9	0.309	6.40	6.40	-1.50 ± 0.03	-4.21 ± 0.02	$+35.1 \pm 1.0$	$+0.09 \pm 0.04$	12
Berkeley 43	1	45.6820	−0.1347	5.8	nan	39.00	nan	-0.95 ± 0.02	-3.55 ± 0.02	$+30.1 \pm 0.0$	-0.01 ± 0.01	1
NGC 6791	2	69.9644	+10.9065	8.2	6.310	7.89	6.47	-0.40 ± 0.01	-2.26 ± 0.02	-46.9 ± 1.2	$+0.31 \pm 0.04$	66
NGC 6819	2	73.9815	+8.4811	11.4	2.239	7.97	8.53	-2.87 ± 0.01	-3.93 ± 0.01	$+2.6 \pm 1.3$	$+0.03 \pm 0.04$	46
Berkeley 85	1	75.6967	+0.9969	6.8	0.417	8.15	7.67	-2.91 ± 0.03	-4.67 ± 0.02	-33.7 ± 1.4	$+0.07 \pm 0.06$	12
Dolidze 41	1	75.7070	+0.9923	5.5	nan	nan	nan	-2.91 ± 0.03	-4.66 ± 0.02	-33.9 ± 1.1	$+0.06 \pm 0.06$	11
NGC 6811	2	79.2072	+11.9983	22.8	1.072	8.14	9.11	-3.24 ± 0.02	-8.83 ± 0.03	$+7.5 \pm 0.3$	-0.06 ± 0.01	7
NGC 6866	1	79.5615	+6.8368	12.5	0.646	8.14	9.36	-1.28 ± 0.03	-5.82 ± 0.04	$+13.1 \pm 0.8$	$+0.00 \pm 0.02$	4
IC 1369	1	89.6059	−0.3978	5.2	0.288	8.89	9.11	-4.58 ± 0.01	-5.71 ± 0.03	-48.7 ± 0.1	-0.11 ± 0.03	3
NGC 7062	1	89.9631	−2.7433	5.8	0.427	8.64	8.93	-1.85 ± 0.01	-4.25 ± 0.01	-22.3 ± 0.0	-0.02 ± 0.01	1
Berkeley 91	1	90.0223	+0.2879	2.8	0.631	10.26	10.37	-1.55 ± 0.04	-3.37 ± 0.04	-51.4 ± 0.1	$+0.07 \pm 0.01$	1
Berkeley 53	2	90.2998	+3.7617	10.7	0.977	8.97	9.72	-3.85 ± 0.03	-5.66 ± 0.03	-35.9 ± 0.8	-0.12 ± 0.02	6
NGC 7058	1	92.8909	+0.6026	13.1	0.041	8.30	8.39	$+7.30 \pm 0.03$	$+2.75 \pm 0.13$	-19.3 ± 0.1	$+0.01 \pm 0.01$	3
Berkeley 98	1	103.8689	−5.6327	7.4	2.455	9.73	8.87	-1.33 ± 0.03	-3.25 ± 0.02	-68.0 ± 2.7	-0.05 ± 0.01	5
FSR 0394	1	108.3181	−0.8073	2.7	nan	nan	nan	-3.72 ± 0.02	-1.24 ± 0.02	-70.6 ± 0.2	-0.12 ± 0.01	3
NGC 7789	2	115.5270	−5.3659	25.3	1.549	9.37	8.78	-0.93 ± 0.02	-2.03 ± 0.02	-53.9 ± 1.5	-0.03 ± 0.04	78
Berkeley 2	1	119.7032	−2.3156	3.2	0.589	13.16	13.06	-1.07 ± 0.02	-0.37 ± 0.04	-75.8 ± 2.5	-0.21 ± 0.02	6
FSR 0494	2	120.0868	+1.0247	6.7	0.891	10.90	11.61	-2.52 ± 0.02	-0.93 ± 0.02	-63.7 ± 1.4	-0.01 ± 0.02	5
FSR 0496	1	120.2171	+1.2691	10.9	2.042	9.07	9.00	$+2.16 \pm 0.11$	-0.62 ± 0.18	-21.2 ± 2.1	-0.15 ± 0.01	2
NGC 136	1	120.5657	−1.2745	3.2	0.257	11.75	12.59	-1.61 ± 0.01	-0.59 ± 0.01	-52.2 ± 0.1	-0.27 ± 0.01	1
King 15	1	120.7647	−0.9403	4.9	0.295	10.43	10.65	-2.36 ± 0.01	-1.04 ± 0.01	-64.6 ± 0.1	-0.13 ± 0.01	1
NGC 188	2	122.8368	+22.3730	32.6	7.079	9.22	9.66	-2.35 ± 0.02	-1.04 ± 0.01	-41.6 ± 0.9	$+0.07 \pm 0.04$	55

Continued on next page

Table A.1 – Continued

Cluster name	Qual flag	l deg	b deg	R[a] (′)	Age[a] Gyr	R_{GC}^{b} (kpc)	R_{Guide} [b] (kpc)	μ_α [c] (mas yr^{-1})	μ_δ [c] (mas yr^{-1})	RV (km s^{-1})	[Fe/H] (dex)	Num stars
King 2	1	122.8693	−4.6837	6.1	4.074	13.21	15.07	-1.48 ± 0.01	-0.65 ± 0.01	-42.4 ± 0.1	-0.18 ± 0.01	1
IC 166	2	130.0516	−0.1695	7.2	1.318	12.36	14.39	-1.46 ± 0.02	$+1.06 \pm 0.02$	-40.6 ± 1.6	-0.10 ± 0.03	20
NGC 752	1	136.9588	−23.2884	58.2	1.175	8.60	8.60	$+9.76 \pm 0.03$	-11.86 ± 0.04	$+5.4 \pm 0.3$	-0.06 ± 0.01	5
Berkeley 66	2	139.4307	+0.1759	6.5	3.090	12.29	12.71	-0.17 ± 0.05	$+0.07 \pm 0.05$	-50.0 ± 0.4	-0.23 ± 0.04	8
King 5	2	143.7685	−4.2812	10.9	1.023	10.46	10.50	-0.28 ± 0.05	-1.30 ± 0.06	-44.0 ± 0.8	-0.16 ± 0.02	4
Berkeley 9	1	146.0697	−2.8248	6.4	1.380	9.83	10.16	$+1.52 \pm 0.03$	$+0.04 \pm 0.03$	-20.1 ± 3.0	-0.18 ± 0.01	2
NGC 1245	2	146.6576	−8.9266	13.1	1.202	11.05	10.90	$+0.49 \pm 0.02$	-1.67 ± 0.01	-29.1 ± 0.8	-0.09 ± 0.03	25
NGC 1193	1	146.8143	−12.1624	3.2	5.129	12.64	12.57	-0.23 ± 0.03	-0.43 ± 0.02	-84.8 ± 0.2	-0.35 ± 0.02	4
Melotte 20	1	147.3566	−6.4040	243.2	0.051	8.42	8.40	$+23.35 \pm 0.05$	-24.97 ± 0.05	-0.2 ± 0.7	$+0.01 \pm 0.06$	16
King 7	2	149.7997	−1.0172	7.2	0.224	11.13	11.22	$+1.06 \pm 0.03$	-1.21 ± 0.03	-10.5 ± 2.2	-0.16 ± 0.04	7
FSR 0667	1	151.1527	−0.6846	8.2	0.708	9.33	9.76	$+0.90 \pm 0.01$	-3.66 ± 0.01	$+2.3 \pm 0.1$	-0.03 ± 0.01	1
NGC 1798	2	160.7043	+4.8500	4.7	1.660	13.20	14.11	$+0.80 \pm 0.02$	-0.37 ± 0.02	$+2.7 \pm 2.2$	-0.28 ± 0.02	10
NGC 1664	1	161.6705	−0.4521	13.6	0.513	9.56	9.31	$+1.66 \pm 0.01$	-5.73 ± 0.01	$+6.9 \pm 0.1$	-0.06 ± 0.01	1
FSR 0716	1	162.2526	+3.6186	6.2	0.871	11.72	12.59	-0.28 ± 0.02	-1.62 ± 0.01	$+21.0 \pm 13.9$	-0.39 ± 0.01	1
Berkeley 18	1	163.5891	+5.0296	14.0	4.365	13.75	15.04	$+0.75 \pm 0.03$	-0.09 ± 0.02	-3.0 ± 1.5	-0.37 ± 0.03	30
Melotte 22	1	166.4628	−23.6146	152.9	0.078	8.39	8.26	$+19.83 \pm 0.07$	-45.04 ± 0.05	$+6.0 \pm 1.4$	$+0.00 \pm 0.05$	52
Czernik 18	1	168.2633	−12.3085	6.1	0.525	9.55	9.63	$+1.74 \pm 0.09$	-3.05 ± 0.07	-15.5 ± 0.1	-0.06 ± 0.01	2
Czernik 20	1	168.2856	+1.4404	3.8	1.660	11.71	12.19	$+0.52 \pm 0.05$	-1.59 ± 0.04	$+32.3 \pm 1.6$	-0.18 ± 0.01	6
NGC 1857	1	168.4140	+1.2589	7.4	0.251	11.13	11.67	$+0.47 \pm 0.02$	-1.37 ± 0.02	$+0.8 \pm 0.4$	-0.18 ± 0.01	2
Czernik 21	1	171.8895	+0.4530	6.4	2.570	12.28	12.12	$+2.24 \pm 0.06$	-0.96 ± 0.04	$+45.4 \pm 0.6$	-0.33 ± 0.01	3
NGC 1912	1	172.2699	+0.6819	19.6	0.295	9.37	9.40	$+1.76 \pm 0.02$	-4.51 ± 0.05	-0.6 ± 0.5	-0.17 ± 0.01	2
NGC 1907	1	172.6207	+0.3173	9.0	0.589	9.88	10.13	-0.18 ± 0.02	-3.49 ± 0.03	$+2.7 \pm 0.2$	-0.12 ± 0.01	3

Continued on next page

Table A.1 – Continued

Cluster name	Qual flag	l deg	b deg	R[a] (′)	Age[a] Gyr	R_{GC}^{b} (kpc)	R_{Guide} [b] (kpc)	μ_α [c] (mas yr^{-1})	μ_δ [c] (mas yr^{-1})	RV (km s^{-1})	[Fe/H] (dex)	Num stars
Teutsch 1	1	175.5588	+1.2067	1.3	0.028	13.58	14.04	$+0.62 \pm 0.02$	-0.88 ± 0.01	$+2.3 \pm 0.1$	-0.31 ± 0.01	1
Berkeley 17	2	175.6578	−3.6769	8.5	7.244	11.60	11.55	$+2.55 \pm 0.03$	-0.36 ± 0.02	-73.5 ± 0.3	-0.18 ± 0.03	8
King 8	1	176.3840	+3.1006	3.0	0.832	13.78	13.15	$+0.44 \pm 0.02$	-1.72 ± 0.01	-1.0 ± 0.0	-0.24 ± 0.01	1
Berkeley 71	2	176.6315	+0.8939	4.3	0.871	11.87	11.89	$+0.67 \pm 0.03$	-1.68 ± 0.02	-8.4 ± 2.5	-0.23 ± 0.01	5
Berkeley 19	1	176.9168	−3.6100	4.4	2.188	14.82	16.00	$+0.70 \pm 0.01$	-0.30 ± 0.01	$+17.7 \pm 0.1$	-0.36 ± 0.01	1
NGC 1746	1	179.1252	−10.4756	18.0	nan	nan	nan	$+3.20 \pm 0.03$	-3.79 ± 0.02	$+4.8 \pm 0.4$	$+0.06 \pm 0.01$	1
Teutsch 10	1	179.9510	−0.2872	5.3	0.617	11.72	11.60	$+0.76 \pm 0.01$	-1.90 ± 0.01	$+5.3 \pm 7.4$	-0.35 ± 0.01	1
NGC 1647	1	180.3675	−16.7923	50.0	0.363	8.88	9.77	-1.03 ± 0.02	-1.52 ± 0.01	-12.9 ± 0.0	-0.19 ± 0.01	1
Czernik 23	1	180.5396	+0.8194	6.0	0.269	12.24	12.43	-0.06 ± 0.01	-1.78 ± 0.01	$+17.8 \pm 0.1$	-0.33 ± 0.01	1
Teutsch 51	2	182.7380	+0.4804	4.1	0.676	12.94	14.16	$+0.54 \pm 0.04$	-0.30 ± 0.04	$+17.6 \pm 0.4$	-0.34 ± 0.02	4
NGC 1817	1	186.1930	−13.0319	22.4	1.122	10.02	10.58	$+0.42 \pm 0.03$	-0.96 ± 0.03	$+66.8 \pm 1.6$	-0.16 ± 0.03	11
Kharchenko 1	1	186.6244	+2.1436	7.8	0.708	10.64	10.10	$+2.20 \pm 0.03$	-2.85 ± 0.02	-6.7 ± 1.6	-0.03 ± 0.04	66
NGC 2158	2	186.6355	+1.7881	5.3	1.549	12.55	12.37	-0.26 ± 0.02	-1.99 ± 0.02	$+27.2 \pm 1.8$	-0.25 ± 0.02	61
Berkeley 21	1	186.8174	−2.4901	3.7	2.138	14.66	14.76	$+0.46 \pm 0.03$	-1.02 ± 0.02	$+0.5 \pm 1.1$	-0.23 ± 0.05	8
FSR 0937	1	195.3114	−1.3092	7.8	1.202	15.82	17.46	$+0.38 \pm 0.08$	-0.10 ± 0.04	$+19.6 \pm 0.7$	-0.35 ± 0.03	3
NGC 2304	1	197.2133	+8.9000	4.6	0.912	11.95	11.65	$+0.00 \pm 0.02$	-1.53 ± 0.04	$+51.2 \pm 0.2$	-0.14 ± 0.01	2
Teutsch 12	1	197.9155	+0.5967	5.6	0.832	12.01	12.53	-0.74 ± 0.02	-0.95 ± 0.02	$+51.0 \pm 1.5$	-0.20 ± 0.01	4
Berkeley 29	1	197.9472	+7.9816	1.7	3.090	20.51	18.10	$+0.11 \pm 0.02$	-1.05 ± 0.02	$+25.3 \pm 0.1$	-0.53 ± 0.02	2
NGC 2420	2	198.1078	+19.6400	6.4	1.738	10.62	10.30	-1.25 ± 0.02	-1.97 ± 0.02	$+74.6 \pm 0.6$	-0.20 ± 0.04	28
Berkeley 22	1	199.8736	−8.0708	2.6	2.455	14.23	13.84	$+0.62 \pm 0.03$	-0.40 ± 0.02	$+94.9 \pm 0.8$	-0.33 ± 0.04	6
Briceno 1	1	200.9817	−18.3440	30.0	nan	nan	nan	$+1.44 \pm 0.06$	$+0.01 \pm 0.06$	$+20.8 \pm 1.3$	-0.09 ± 0.06	29
Trumpler 5	1	202.8143	+1.0211	16.1	4.266	11.15	12.12	-0.59 ± 0.03	$+0.27 \pm 0.02$	$+51.2 \pm 1.9$	-0.45 ± 0.01	10

Continued on next page

Table A.1 – Continued

Cluster name	Qual flag	l deg	b deg	R[a] (′)	Age[a] Gyr	R_{GC}^{b} (kpc)	R_{Guide} [b] (kpc)	μ_α [c] (mas yr^{-1})	μ_δ [c] (mas yr^{-1})	RV (km s^{-1})	[Fe/H] (dex)	Num stars
Berkeley 20	1	203.4853	−17.3763	1.8	4.786	16.26	15.45	$+0.91 \pm 0.01$	-0.27 ± 0.01	$+76.6 \pm 0.2$	-0.43 ± 0.01	1
NGC 2202	1	203.5978	−4.8847	4.8	nan	nan	nan	$+0.36 \pm 0.42$	$+0.62 \pm 0.25$	$+52.9 \pm 0.1$	-0.46 ± 0.01	2
NGC 2632	1	205.9525	+32.4278	118.2	0.676	8.41	8.51	-36.42 ± 0.05	-13.04 ± 0.04	$+35.3 \pm 0.6$	$+0.14 \pm 0.06$	28
Berkeley 31	1	206.2398	+5.1334	3.7	2.818	15.02	13.98	$+0.24 \pm 0.03$	-0.89 ± 0.02	$+58.8 \pm 0.9$	-0.43 ± 0.02	2
NGC 2324	1	213.4480	+3.3012	8.3	0.537	12.01	12.61	-0.36 ± 0.01	-0.05 ± 0.02	$+42.4 \pm 0.2$	-0.22 ± 0.02	4
Saurer 1	1	214.6969	+7.3830	2.7	nan	nan	nan	-0.26 ± 0.02	-0.31 ± 0.02	$+104.9 \pm 0.0$	-0.42 ± 0.01	1
NGC 2682	2	215.6912	+31.9208	19.9	4.266	8.90	8.97	-11.00 ± 0.03	-2.91 ± 0.02	$+34.3 \pm 1.0$	-0.00 ± 0.05	331
FSR 1113	1	216.2980	+3.2637	2.9	2.754	11.52	12.77	-0.47 ± 0.01	$+1.77 \pm 0.01$	$+68.9 \pm 0.0$	-0.35 ± 0.01	1
Berkeley 33	1	225.4474	−4.5998	3.8	0.234	13.05	14.57	-0.69 ± 0.01	$+1.59 \pm 0.01$	$+77.8 \pm 0.1$	-0.24 ± 0.01	1
NGC 2204	1	226.0162	−16.1134	11.8	2.089	11.28	11.63	-0.58 ± 0.01	$+1.96 \pm 0.02$	$+92.3 \pm 0.8$	-0.29 ± 0.03	23
Czernik 30	1	226.3359	+4.1585	3.6	2.884	13.72	12.88	-0.62 ± 0.01	-0.06 ± 0.01	$+81.4 \pm 0.3$	-0.39 ± 0.01	2
Haffner 4	1	227.9399	−3.6274	2.9	0.457	12.24	12.71	-0.43 ± 0.01	$+0.93 \pm 0.01$	$+59.7 \pm 0.2$	-0.18 ± 0.01	1
Melotte 71	1	228.9511	+4.5055	9.0	0.977	9.81	11.00	-2.35 ± 0.01	$+4.21 \pm 0.05$	$+50.8 \pm 0.4$	-0.15 ± 0.02	3
Tombaugh 2	1	232.8360	−6.8799	3.4	1.622	15.70	16.75	-0.53 ± 0.02	$+1.42 \pm 0.02$	$+122.0 \pm 1.6$	-0.37 ± 0.03	9
Berkeley 75	1	234.3082	−11.1909	3.8	1.698	14.61	13.84	-0.22 ± 0.01	$+1.14 \pm 0.02$	$+124.2 \pm 0.9$	-0.41 ± 0.01	3
NGC 2479	1	235.9970	+5.3590	9.0	0.977	9.24	9.44	-4.30 ± 0.01	$+1.17 \pm 0.01$	$+41.6 \pm 0.1$	-0.05 ± 0.01	1
NGC 2243	1	239.4780	−18.0111	5.5	4.365	10.52	12.79	-1.24 ± 0.01	$+5.49 \pm 0.01$	$+59.8 \pm 0.5$	-0.46 ± 0.03	11
NGC 2447	1	240.0428	+0.1491	24.2	0.575	8.83	9.20	-1.46 ± 0.16	$+1.99 \pm 0.19$	$+23.5 \pm 0.6$	-0.11 ± 0.01	3
ESO 211 03	1	269.2401	−3.7695	6.1	1.288	9.89	10.72	-4.72 ± 0.04	$+4.39 \pm 0.04$	$+64.4 \pm 1.3$	-0.16 ± 0.03	15
Ruprecht 82	1	277.7240	−0.4842	7.6	0.457	8.27	9.00	-6.41 ± 0.04	$+4.23 \pm 0.13$	$+2.0 \pm 0.1$	-0.04 ± 0.01	1
Ruprecht 85	1	280.1984	+0.0759	4.1	0.204	8.80	9.06	-4.33 ± 0.01	$+3.22 \pm 0.01$	$+21.8 \pm 0.0$	-0.25 ± 0.01	2
Collinder 220	1	284.5480	−0.3486	13.1	0.234	8.02	8.87	-5.32 ± 0.52	$+3.73 \pm 0.63$	-12.5 ± 0.1	-0.12 ± 0.01	1

Continued on next page

Table A.1 – Continued

Cluster name	Qual flag	l deg	b deg	R[a] (′)	Age[a] Gyr	R_{GC}^{b} (kpc)	R_{Guide} [b] (kpc)	μ_α [c] (mas yr^{-1})	μ_δ [c] (mas yr^{-1})	RV (km s^{-1})	[Fe/H] (dex)	Num stars
SAI 116	1	295.7623	−0.2224	5.8	0.126	7.47	7.71	-7.10 ± 0.21	$+1.23 \pm 0.06$	-14.0 ± 0.1	$+0.14 \pm 0.01$	3
NGC 4337	1	299.3160	+4.5546	6.6	1.445	7.39	7.49	-8.83 ± 0.02	$+1.55 \pm 0.02$	-18.1 ± 1.0	$+0.24 \pm 0.03$	7
BH 131	1	300.1162	−0.6800	5.0	nan	nan	nan	-6.47 ± 0.02	$+0.29 \pm 0.03$	-31.7 ± 0.6	$+0.10 \pm 0.01$	7
Trumpler 20	1	301.4714	+2.2010	13.4	1.862	7.12	7.72	-7.09 ± 0.02	$+0.17 \pm 0.02$	-40.0 ± 0.8	$+0.11 \pm 0.02$	26
Teutsch 84	1	344.4449	−0.4563	4.2	1.047	5.95	6.33	-1.74 ± 0.06	-1.17 ± 0.04	-56.3 ± 0.0	$+0.20 \pm 0.01$	1
ESO 518 03	1	355.0583	+12.4339	11.4	1.413	6.69	7.08	$+2.71 \pm 0.03$	-2.66 ± 0.02	$+22.9 \pm 0.9$	$+0.07 \pm 0.05$	10

[a] Cluster Radius and age from Cantat-Gaudin et al. (2020)

[b] Calculated with distances from Cantat-Gaudin et al. (2020), recomputed to a solar radius of $R_0 = 8.274$ kpc.

[c] μ_α and μ_δ and their 1σ uncertainties are those of the 2D Gaussian fit, as in Donor et al. (2018).

Table A.2: OCCAM DR17 Sample - Detailed Chemistry

Cluster name	[Fe/H] (dex)	[O/Fe] (dex)	[Na/Fe] (dex)	[Mg/Fe] (dex)	[Al/Fe] (dex)	[Si/Fe] (dex)	[S/Fe] (dex)	[K/Fe] (dex)
	[Ca/Fe] (dex)	[Ti/Fe] (dex)	[V/Fe] (dex)	[Cr/Fe] (dex)	[Mn/Fe] (dex)	[Co/Fe] (dex)	[Ni/Fe] (dex)	[Ce/Fe] (dex)
Ruprecht 147	0.11 ± 0.03	0.01 ± 0.07	0.01 ± 0.20	-0.03 ± 0.04	0.11 ± 0.07	0.05 ± 0.05	-0.01 ± 0.05	0.04 ± 0.16
	-0.03 ± 0.05	-0.20 ± 0.24	-0.07 ± 0.16	-0.14 ± 0.21	0.05 ± 0.03	-0.33 ± 0.53	0.01 ± 0.02	-0.43 ± 0.72
NGC 6705	0.09 ± 0.04	-0.06 ± 0.02	0.25 ± 0.06	-0.04 ± 0.02	-0.09 ± 0.04	0.01 ± 0.01	0.04 ± 0.03	-0.14 ± 0.04
	-0.04 ± 0.02	-0.01 ± 0.02	-0.21 ± 0.07	0.00 ± 0.04	0.10 ± 0.02	0.06 ± 0.04	0.03 ± 0.02	0.13 ± 0.10
Berkeley 43	-0.01 ± 0.01	-0.04 ± 0.01	0.15 ± 0.05	-0.05 ± 0.01	-0.17 ± 0.02	0.02 ± 0.01	0.13 ± 0.03	-0.17 ± 0.03
	-0.05 ± 0.01	-0.03 ± 0.02	-0.40 ± 0.06	-0.09 ± 0.03	0.11 ± 0.01	-0.02 ± 0.04	0.04 ± 0.01	0.30 ± 0.06
NGC 6791	0.31 ± 0.04	0.05 ± 0.02	0.17 ± 0.05	0.08 ± 0.02	0.02 ± 0.05	0.01 ± 0.03	-0.01 ± 0.07	0.09 ± 0.09
	-0.04 ± 0.04	0.15 ± 0.10	-0.20 ± 0.20	0.04 ± 0.06	0.05 ± 0.11	0.14 ± 0.06	0.02 ± 0.04	-0.14 ± 0.10
NGC 6819	0.03 ± 0.04	-0.00 ± 0.03	0.09 ± 0.09	0.02 ± 0.01	0.01 ± 0.04	0.01 ± 0.02	-0.01 ± 0.04	-0.03 ± 0.07
	0.00 ± 0.02	0.03 ± 0.03	-0.13 ± 0.14	0.01 ± 0.03	0.02 ± 0.03	0.04 ± 0.06	0.00 ± 0.02	-0.03 ± 0.10
Berkeley 85	0.07 ± 0.06	-0.06 ± 0.05	0.20 ± 0.12	-0.05 ± 0.03	-0.10 ± 0.06	-0.02 ± 0.03	0.05 ± 0.08	-0.02 ± 0.06
	-0.08 ± 0.04	0.02 ± 0.05	-0.22 ± 0.08	-0.09 ± 0.17	0.10 ± 0.06	-0.04 ± 0.36	0.02 ± 0.04	0.09 ± 0.43
Dolidze 41	0.06 ± 0.06	-0.04 ± 0.04	0.22 ± 0.10	-0.05 ± 0.02	-0.10 ± 0.06	-0.01 ± 0.03	0.03 ± 0.07	-0.03 ± 0.07
	-0.07 ± 0.02	0.01 ± 0.05	-0.21 ± 0.07	-0.09 ± 0.17	0.12 ± 0.03	0.07 ± 0.05	0.02 ± 0.03	0.19 ± 0.27
NGC 6811	-0.06 ± 0.01	-0.03 ± 0.04	0.08 ± 0.07	0.00 ± 0.01	-0.02 ± 0.02	0.00 ± 0.01	0.02 ± 0.03	-0.05 ± 0.04
	0.02 ± 0.02	-0.01 ± 0.03	0.12 ± 0.09	0.04 ± 0.04	-0.02 ± 0.01	-0.08 ± 0.11	-0.03 ± 0.01	0.13 ± 0.09
NGC 6866	0.00 ± 0.02	-0.06 ± 0.02	0.04 ± 0.10	0.00 ± 0.01	-0.03 ± 0.02	-0.01 ± 0.01	0.06 ± 0.03	-0.03 ± 0.03
	0.01 ± 0.02	-0.01 ± 0.02	0.14 ± 0.09	0.03 ± 0.04	0.01 ± 0.01	-0.09 ± 0.07	-0.03 ± 0.02	0.09 ± 0.09
IC 1369	-0.11 ± 0.03	-0.03 ± 0.02	0.12 ± 0.06	-0.02 ± 0.01	-0.05 ± 0.03	-0.01 ± 0.01	0.09 ± 0.08	-0.01 ± 0.04
	0.01 ± 0.02	-0.06 ± 0.02	0.17 ± 0.09	-0.01 ± 0.04	0.01 ± 0.01	-0.03 ± 0.06	-0.06 ± 0.01	0.21 ± 0.09
NGC 7062	-0.02 ± 0.01	-0.05 ± 0.02	0.16 ± 0.06	-0.04 ± 0.01	-0.00 ± 0.02	0.00 ± 0.01	0.00 ± 0.03	-0.03 ± 0.03
	-0.01 ± 0.01	-0.05 ± 0.02	0.17 ± 0.09	-0.08 ± 0.04	-0.02 ± 0.01	0.03 ± 0.06	-0.04 ± 0.01	0.14 ± 0.09

Continued on next page

Table A.2 – Continued

Cluster name	[Fe/H] (dex)	[O/Fe] (dex)	[Na/Fe] (dex)	[Mg/Fe] (dex)	[Al/Fe] (dex)	[Si/Fe] (dex)	[S/Fe] (dex)	[K/Fe] (dex)
	[Ca/Fe] (dex)	[Ti/Fe] (dex)	[V/Fe] (dex)	[Cr/Fe] (dex)	[Mn/Fe] (dex)	[Co/Fe] (dex)	[Ni/Fe] (dex)	[Ce/Fe] (dex)
Berkeley 91	0.07 ± 0.01	-0.02 ± 0.02	-0.04 ± 0.07	0.01 ± 0.01	0.06 ± 0.03	-0.05 ± 0.02	0.05 ± 0.04	0.04 ± 0.04
	0.04 ± 0.02	0.06 ± 0.03	-0.38 ± 0.09	0.03 ± 0.04	0.03 ± 0.02	-0.11 ± 0.07	-0.01 ± 0.02	0.07 ± 0.10
Berkeley 53	-0.12 ± 0.02	0.00 ± 0.02	0.10 ± 0.07	0.02 ± 0.02	0.02 ± 0.06	0.01 ± 0.02	0.03 ± 0.05	0.05 ± 0.04
	0.01 ± 0.03	-0.02 ± 0.03	-0.12 ± 0.16	-0.01 ± 0.07	-0.01 ± 0.02	-0.01 ± 0.08	-0.04 ± 0.01	0.24 ± 0.09
NGC 7058	0.01 ± 0.01	-0.03 ± 0.05	-0.01 ± 0.10	-0.07 ± 0.02	-0.06 ± 0.03	-0.02 ± 0.04	0.22 ± 0.08	0.02 ± 0.03
	-0.05 ± 0.06	-0.21 ± 0.06	$nan \pm nan$	-0.16 ± 0.06	-0.11 ± 0.04	$nan \pm nan$	0.01 ± 0.02	$nan \pm nan$
Berkeley 98	-0.05 ± 0.01	0.02 ± 0.02	0.12 ± 0.08	0.03 ± 0.01	0.07 ± 0.03	0.01 ± 0.02	0.01 ± 0.07	0.04 ± 0.05
	-0.00 ± 0.02	-0.00 ± 0.04	-0.08 ± 0.21	0.05 ± 0.05	-0.04 ± 0.03	0.06 ± 0.09	-0.02 ± 0.02	0.04 ± 0.11
FSR 0394	-0.12 ± 0.01	-0.04 ± 0.03	-0.06 ± 0.46	0.00 ± 0.01	0.07 ± 0.03	0.01 ± 0.02	0.10 ± 0.05	0.01 ± 0.05
	0.02 ± 0.02	-0.04 ± 0.03	-0.05 ± 0.19	0.02 ± 0.05	-0.05 ± 0.03	-0.02 ± 0.11	-0.05 ± 0.02	0.15 ± 0.12
NGC 7789	-0.03 ± 0.04	-0.02 ± 0.05	-0.01 ± 0.22	-0.00 ± 0.03	0.01 ± 0.05	0.01 ± 0.04	0.03 ± 0.08	0.06 ± 0.12
	-0.03 ± 0.11	-0.01 ± 0.15	-0.05 ± 0.22	-0.02 ± 0.24	-0.01 ± 0.05	-0.01 ± 0.06	-0.04 ± 0.03	0.01 ± 0.12
Berkeley 2	-0.21 ± 0.02	-0.01 ± 0.05	0.06 ± 0.66	-0.02 ± 0.04	0.02 ± 0.03	-0.01 ± 0.04	0.08 ± 0.11	0.03 ± 0.08
	0.03 ± 0.04	-0.01 ± 0.06	0.06 ± 0.27	0.04 ± 0.07	-0.06 ± 0.04	-0.52 ± 0.40	-0.02 ± 0.04	0.25 ± 0.15
FSR 0494	-0.01 ± 0.02	-0.06 ± 0.04	0.07 ± 0.19	-0.02 ± 0.02	-0.01 ± 0.04	-0.02 ± 0.02	-0.06 ± 0.10	-0.06 ± 0.12
	0.02 ± 0.02	-0.04 ± 0.04	0.24 ± 0.16	0.01 ± 0.07	-0.04 ± 0.02	-0.32 ± 0.42	-0.03 ± 0.02	0.11 ± 0.18
FSR 0496	-0.15 ± 0.01	0.01 ± 0.13	-0.56 ± 0.63	0.09 ± 0.06	0.09 ± 0.05	0.08 ± 0.08	0.07 ± 0.06	0.08 ± 0.05
	-0.19 ± 0.23	-0.22 ± 0.21	-0.12 ± 0.22	-0.16 ± 0.10	-0.18 ± 0.12	-0.03 ± 0.06	-0.06 ± 0.03	0.15 ± 0.08
NGC 136	-0.27 ± 0.01	-0.10 ± 0.03	-0.53 ± 0.08	-0.01 ± 0.01	-0.03 ± 0.02	0.00 ± 0.01	0.21 ± 0.04	0.04 ± 0.04
	0.04 ± 0.01	0.05 ± 0.02	0.50 ± 0.11	0.00 ± 0.05	-0.01 ± 0.02	-0.02 ± 0.07	-0.03 ± 0.01	0.51 ± 0.10
King 15	-0.13 ± 0.01	-0.11 ± 0.02	-0.07 ± 0.07	-0.01 ± 0.01	-0.03 ± 0.02	0.00 ± 0.01	0.13 ± 0.03	-0.20 ± 0.04
	0.00 ± 0.01	0.03 ± 0.02	0.22 ± 0.09	-0.01 ± 0.04	-0.00 ± 0.01	-0.07 ± 0.06	-0.05 ± 0.01	0.50 ± 0.08

Continued on next page

Table A.2 – Continued

Cluster name	[Fe/H] (dex)	[O/Fe] (dex)	[Na/Fe] (dex)	[Mg/Fe] (dex)	[Al/Fe] (dex)	[Si/Fe] (dex)	[S/Fe] (dex)	[K/Fe] (dex)
	[Ca/Fe] (dex)	[Ti/Fe] (dex)	[V/Fe] (dex)	[Cr/Fe] (dex)	[Mn/Fe] (dex)	[Co/Fe] (dex)	[Ni/Fe] (dex)	[Ce/Fe] (dex)
NGC 188	0.07 ± 0.04	0.04 ± 0.04	0.09 ± 0.17	0.06 ± 0.02	0.08 ± 0.07	0.03 ± 0.03	0.01 ± 0.07	0.07 ± 0.06
	0.00 ± 0.04	0.03 ± 0.09	-0.12 ± 0.19	0.08 ± 0.08	0.06 ± 0.04	0.08 ± 0.12	0.04 ± 0.03	-0.35 ± 0.41
King 2	-0.18 ± 0.01	0.09 ± 0.02	-0.01 ± 0.08	0.10 ± 0.02	0.04 ± 0.03	0.03 ± 0.02	-0.04 ± 0.06	0.11 ± 0.05
	0.02 ± 0.02	0.05 ± 0.03	-0.31 ± 0.09	-0.04 ± 0.05	-0.05 ± 0.02	0.09 ± 0.07	0.02 ± 0.02	0.22 ± 0.08
IC 166	-0.10 ± 0.03	-0.07 ± 0.06	0.10 ± 0.12	0.01 ± 0.02	0.08 ± 0.06	0.02 ± 0.03	0.05 ± 0.07	0.02 ± 0.09
	0.02 ± 0.04	-0.05 ± 0.07	0.10 ± 0.21	0.02 ± 0.10	-0.04 ± 0.04	-0.12 ± 0.21	-0.03 ± 0.04	0.15 ± 0.20
NGC 752	-0.06 ± 0.01	-0.04 ± 0.02	0.11 ± 0.19	-0.00 ± 0.02	0.02 ± 0.03	-0.01 ± 0.01	-0.01 ± 0.03	-0.10 ± 0.10
	0.04 ± 0.03	-0.04 ± 0.02	0.06 ± 0.13	0.01 ± 0.04	-0.04 ± 0.02	-0.06 ± 0.06	-0.03 ± 0.02	0.10 ± 0.10
Berkeley 66	-0.23 ± 0.04	0.05 ± 0.05	0.03 ± 0.20	0.10 ± 0.02	0.04 ± 0.04	0.04 ± 0.02	0.04 ± 0.06	0.06 ± 0.06
	0.02 ± 0.02	-0.00 ± 0.03	-0.03 ± 0.16	0.01 ± 0.06	-0.03 ± 0.03	0.05 ± 0.12	-0.04 ± 0.03	0.04 ± 0.12
King 5	-0.16 ± 0.02	0.00 ± 0.03	0.05 ± 0.08	0.02 ± 0.01	0.01 ± 0.04	0.01 ± 0.02	0.05 ± 0.04	0.04 ± 0.04
	0.01 ± 0.03	0.02 ± 0.04	0.00 ± 0.19	-0.04 ± 0.08	-0.04 ± 0.04	-0.03 ± 0.11	-0.05 ± 0.01	0.05 ± 0.09
Berkeley 9	-0.18 ± 0.01	0.00 ± 0.24	-0.18 ± 0.28	-0.01 ± 0.02	-0.25 ± 0.28	0.07 ± 0.06	0.07 ± 0.06	-0.20 ± 0.29
	0.05 ± 0.02	0.02 ± 0.02	-0.27 ± 0.30	0.02 ± 0.13	-0.03 ± 0.02	-0.12 ± 0.08	-0.08 ± 0.07	0.13 ± 0.10
NGC 1245	-0.09 ± 0.03	-0.09 ± 0.08	-0.02 ± 0.12	-0.02 ± 0.02	0.00 ± 0.03	-0.00 ± 0.02	0.00 ± 0.06	-0.02 ± 0.05
	0.01 ± 0.02	-0.01 ± 0.03	0.10 ± 0.13	-0.02 ± 0.05	-0.03 ± 0.02	-0.09 ± 0.22	-0.05 ± 0.02	0.17 ± 0.12
NGC 1193	-0.35 ± 0.02	0.11 ± 0.02	0.10 ± 0.10	0.10 ± 0.02	0.13 ± 0.08	0.05 ± 0.02	0.14 ± 0.07	0.12 ± 0.05
	0.05 ± 0.04	0.02 ± 0.04	-0.10 ± 0.13	0.02 ± 0.06	-0.02 ± 0.06	0.08 ± 0.10	0.03 ± 0.03	-0.11 ± 0.11
Melotte 20	0.01 ± 0.06	0.00 ± 0.06	-0.13 ± 0.11	-0.03 ± 0.03	-0.02 ± 0.04	0.02 ± 0.02	0.09 ± 0.13	0.03 ± 0.07
	-0.02 ± 0.13	-0.01 ± 0.20	0.03 ± 0.10	-0.07 ± 0.04	-0.01 ± 0.10	$nan \pm nan$	0.00 ± 0.05	$nan \pm nan$
King 7	-0.16 ± 0.04	-0.01 ± 0.03	0.12 ± 0.08	0.00 ± 0.01	-0.05 ± 0.04	-0.02 ± 0.02	0.06 ± 0.03	0.02 ± 0.06
	-0.01 ± 0.02	-0.05 ± 0.03	-0.23 ± 0.44	0.03 ± 0.05	0.04 ± 0.03	0.02 ± 0.05	-0.07 ± 0.03	0.24 ± 0.06

Continued on next page

Table A.2 – Continued

Cluster name	[Fe/H] (dex)	[O/Fe] (dex)	[Na/Fe] (dex)	[Mg/Fe] (dex)	[Al/Fe] (dex)	[Si/Fe] (dex)	[S/Fe] (dex)	[K/Fe] (dex)
	[Ca/Fe] (dex)	[Ti/Fe] (dex)	[V/Fe] (dex)	[Cr/Fe] (dex)	[Mn/Fe] (dex)	[Co/Fe] (dex)	[Ni/Fe] (dex)	[Ce/Fe] (dex)
FSR 0667	-0.03 ± 0.01	-0.05 ± 0.02	0.01 ± 0.06	-0.02 ± 0.01	0.02 ± 0.02	0.03 ± 0.01	0.03 ± 0.03	-0.08 ± 0.03
	0.00 ± 0.01	-0.05 ± 0.02	0.10 ± 0.09	-0.08 ± 0.04	-0.02 ± 0.01	-0.10 ± 0.06	-0.07 ± 0.01	0.10 ± 0.08
NGC 1798	-0.28 ± 0.02	0.00 ± 0.05	0.04 ± 0.19	0.02 ± 0.02	0.03 ± 0.05	0.03 ± 0.02	0.06 ± 0.08	0.02 ± 0.11
	0.03 ± 0.02	-0.01 ± 0.04	-0.09 ± 0.13	-0.03 ± 0.06	-0.04 ± 0.03	-0.15 ± 0.31	-0.04 ± 0.02	0.21 ± 0.11
NGC 1664	-0.06 ± 0.01	-0.09 ± 0.02	0.09 ± 0.07	-0.04 ± 0.01	-0.02 ± 0.02	0.03 ± 0.01	0.06 ± 0.03	-0.06 ± 0.03
	0.03 ± 0.01	-0.03 ± 0.02	0.22 ± 0.09	-0.03 ± 0.04	-0.03 ± 0.01	-0.01 ± 0.07	-0.04 ± 0.01	0.16 ± 0.09
FSR 0716	-0.39 ± 0.01	0.02 ± 0.05	-0.10 ± 0.13	-0.06 ± 0.02	0.03 ± 0.03	-0.04 ± 0.02	0.04 ± 0.06	0.02 ± 0.05
	0.01 ± 0.02	0.04 ± 0.04	0.15 ± 0.18	0.05 ± 0.08	-0.05 ± 0.02	-0.45 ± 0.14	-0.01 ± 0.02	0.48 ± 0.16
Berkeley 18	-0.37 ± 0.03	0.09 ± 0.06	0.06 ± 0.18	0.11 ± 0.02	0.09 ± 0.05	0.08 ± 0.04	0.13 ± 0.08	0.17 ± 0.13
	0.05 ± 0.07	0.03 ± 0.05	-0.08 ± 0.33	-0.05 ± 0.14	-0.02 ± 0.04	-0.04 ± 0.37	0.00 ± 0.05	0.11 ± 0.15
Melotte 22	0.00 ± 0.05	-0.02 ± 0.04	-0.29 ± 0.31	-0.04 ± 0.05	0.00 ± 0.03	-0.01 ± 0.03	0.03 ± 0.08	0.01 ± 0.07
	-0.05 ± 0.06	-0.14 ± 0.13	0.03 ± 0.12	-0.07 ± 0.17	-0.02 ± 0.09	$nan \pm nan$	-0.01 ± 0.03	$nan \pm nan$
Czernik 18	-0.06 ± 0.01	-0.10 ± 0.13	-0.78 ± 0.61	0.00 ± 0.05	-0.13 ± 0.03	0.09 ± 0.07	0.12 ± 0.09	-0.14 ± 0.06
	0.09 ± 0.05	-0.29 ± 0.11	-0.37 ± 0.28	-1.14 ± 1.10	-0.09 ± 0.04	$nan \pm nan$	-0.01 ± 0.03	$nan \pm nan$
Czernik 20	-0.18 ± 0.01	0.04 ± 0.06	0.05 ± 0.12	0.03 ± 0.02	0.03 ± 0.03	0.01 ± 0.02	0.10 ± 0.06	0.06 ± 0.08
	0.03 ± 0.03	-0.03 ± 0.04	0.18 ± 0.17	-0.02 ± 0.09	-0.06 ± 0.03	-0.31 ± 0.44	-0.05 ± 0.02	0.25 ± 0.16
NGC 1857	-0.18 ± 0.01	-0.10 ± 0.05	-0.20 ± 0.10	-0.05 ± 0.01	-0.08 ± 0.05	-0.01 ± 0.01	0.15 ± 0.03	-0.15 ± 0.04
	-0.00 ± 0.01	0.03 ± 0.06	0.33 ± 0.11	-0.14 ± 0.04	-0.01 ± 0.01	-0.19 ± 0.19	-0.04 ± 0.02	0.56 ± 0.19
Czernik 21	-0.33 ± 0.01	0.13 ± 0.04	0.00 ± 0.10	0.06 ± 0.02	0.08 ± 0.03	0.02 ± 0.02	0.04 ± 0.08	0.03 ± 0.05
	0.07 ± 0.02	0.00 ± 0.03	0.17 ± 0.15	-0.05 ± 0.06	-0.03 ± 0.02	0.02 ± 0.17	-0.01 ± 0.02	0.14 ± 0.11
NGC 1912	-0.17 ± 0.01	-0.08 ± 0.02	0.00 ± 0.07	-0.04 ± 0.01	-0.03 ± 0.02	0.00 ± 0.01	0.17 ± 0.03	-0.11 ± 0.04
	0.01 ± 0.01	0.00 ± 0.02	0.28 ± 0.09	-0.04 ± 0.04	-0.00 ± 0.01	-0.06 ± 0.07	-0.05 ± 0.01	0.41 ± 0.09

Continued on next page

Table A.2 – Continued

Cluster name	[Fe/H] (dex)	[O/Fe] (dex)	[Na/Fe] (dex)	[Mg/Fe] (dex)	[Al/Fe] (dex)	[Si/Fe] (dex)	[S/Fe] (dex)	[K/Fe] (dex)
	[Ca/Fe] (dex)	[Ti/Fe] (dex)	[V/Fe] (dex)	[Cr/Fe] (dex)	[Mn/Fe] (dex)	[Co/Fe] (dex)	[Ni/Fe] (dex)	[Ce/Fe] (dex)
NGC 1907	-0.12 ± 0.01	0.01 ± 0.03	0.14 ± 0.07	0.01 ± 0.01	-0.03 ± 0.03	0.00 ± 0.01	0.10 ± 0.04	-0.07 ± 0.06
	0.01 ± 0.01	-0.04 ± 0.02	0.17 ± 0.09	0.03 ± 0.04	-0.01 ± 0.01	-0.01 ± 0.07	-0.04 ± 0.01	0.20 ± 0.09
Teutsch 1	-0.31 ± 0.01	-0.12 ± 0.03	0.12 ± 0.09	-0.03 ± 0.01	0.00 ± 0.02	-0.00 ± 0.01	0.08 ± 0.04	0.01 ± 0.04
	0.03 ± 0.02	-0.04 ± 0.03	0.12 ± 0.12	-0.13 ± 0.05	-0.07 ± 0.02	-0.17 ± 0.08	-0.07 ± 0.01	0.23 ± 0.10
Berkeley 17	-0.18 ± 0.03	0.08 ± 0.02	0.00 ± 0.07	0.10 ± 0.02	0.10 ± 0.03	0.04 ± 0.02	0.11 ± 0.05	0.10 ± 0.04
	0.03 ± 0.03	0.04 ± 0.05	-0.12 ± 0.17	0.00 ± 0.05	-0.02 ± 0.02	0.08 ± 0.06	0.02 ± 0.01	-0.09 ± 0.08
King 8	-0.24 ± 0.01	0.04 ± 0.04	0.13 ± 0.13	-0.01 ± 0.02	0.00 ± 0.04	-0.01 ± 0.02	0.22 ± 0.07	-0.01 ± 0.06
	0.01 ± 0.03	0.00 ± 0.04	0.15 ± 0.17	0.12 ± 0.08	-0.02 ± 0.03	-0.08 ± 0.15	0.01 ± 0.02	0.23 ± 0.16
Berkeley 71	-0.23 ± 0.01	-0.01 ± 0.12	-0.04 ± 0.09	0.00 ± 0.01	-0.02 ± 0.05	0.01 ± 0.02	0.12 ± 0.05	-0.02 ± 0.04
	0.05 ± 0.02	0.04 ± 0.06	0.20 ± 0.14	-0.13 ± 0.06	-0.07 ± 0.02	-0.17 ± 0.15	-0.05 ± 0.03	0.23 ± 0.13
Berkeley 19	-0.36 ± 0.01	0.09 ± 0.02	0.02 ± 0.08	0.13 ± 0.02	0.11 ± 0.03	0.01 ± 0.02	0.06 ± 0.06	0.04 ± 0.05
	0.01 ± 0.02	0.03 ± 0.03	-0.40 ± 0.09	-0.02 ± 0.05	-0.04 ± 0.02	-0.00 ± 0.07	-0.02 ± 0.02	0.21 ± 0.07
NGC 1746	0.06 ± 0.01	-0.30 ± 0.05	-0.74 ± 0.15	-0.10 ± 0.03	0.04 ± 0.04	0.10 ± 0.03	0.24 ± 0.09	0.08 ± 0.05
	-0.09 ± 0.03	0.38 ± 0.07	-2.14 ± 0.16	-0.08 ± 0.08	0.02 ± 0.03	$nan \pm nan$	0.02 ± 0.03	$nan \pm nan$
Teutsch 10	-0.35 ± 0.01	-0.05 ± 0.03	0.17 ± 0.09	-0.04 ± 0.01	-0.11 ± 0.02	-0.10 ± 0.01	0.13 ± 0.04	0.10 ± 0.04
	0.09 ± 0.02	0.03 ± 0.03	0.34 ± 0.12	0.03 ± 0.05	0.07 ± 0.02	0.14 ± 0.09	0.00 ± 0.01	0.28 ± 0.11
NGC 1647	-0.19 ± 0.01	0.09 ± 0.39	0.83 ± 0.48	0.14 ± 0.05	0.13 ± 0.04	-0.18 ± 0.05	-0.07 ± 0.11	$nan \pm nan$
	0.45 ± 0.05	0.27 ± 0.23	$nan \pm nan$	-2.32 ± 0.21	$nan \pm nan$	$nan \pm nan$	-0.09 ± 0.03	$nan \pm nan$
Czernik 23	-0.33 ± 0.01	-0.07 ± 0.03	0.12 ± 0.09	-0.03 ± 0.01	-0.03 ± 0.02	-0.00 ± 0.01	0.13 ± 0.04	-0.06 ± 0.04
	0.03 ± 0.02	-0.10 ± 0.03	0.26 ± 0.11	-0.07 ± 0.05	-0.02 ± 0.02	-0.18 ± 0.08	-0.07 ± 0.01	0.20 ± 0.10
Teutsch 51	-0.34 ± 0.02	0.13 ± 0.06	0.03 ± 0.16	0.02 ± 0.02	0.08 ± 0.04	0.05 ± 0.03	0.02 ± 0.08	0.03 ± 0.13
	0.02 ± 0.03	-0.03 ± 0.05	0.17 ± 0.24	0.01 ± 0.10	-0.08 ± 0.05	-0.34 ± 0.32	-0.02 ± 0.02	0.25 ± 0.20

Continued on next page

Table A.2 – Continued

Cluster name	[Fe/H] (dex)	[O/Fe] (dex)	[Na/Fe] (dex)	[Mg/Fe] (dex)	[Al/Fe] (dex)	[Si/Fe] (dex)	[S/Fe] (dex)	[K/Fe] (dex)
	[Ca/Fe] (dex)	[Ti/Fe] (dex)	[V/Fe] (dex)	[Cr/Fe] (dex)	[Mn/Fe] (dex)	[Co/Fe] (dex)	[Ni/Fe] (dex)	[Ce/Fe] (dex)
NGC 1817	-0.16 ± 0.03	0.05 ± 0.31	0.06 ± 0.30	-0.01 ± 0.10	-0.08 ± 0.24	-0.03 ± 0.09	0.07 ± 0.10	-0.32 ± 0.86
	-0.01 ± 0.30	-0.01 ± 0.16	0.28 ± 0.42	-0.04 ± 0.18	-0.18 ± 0.26	-0.12 ± 0.16	-0.04 ± 0.05	0.22 ± 0.13
Kharchenko 1	-0.03 ± 0.04	0.03 ± 0.15	-0.36 ± 0.69	-0.08 ± 0.05	-0.02 ± 0.09	0.02 ± 0.04	-0.00 ± 0.11	-0.04 ± 0.19
	-0.03 ± 0.12	-0.08 ± 0.30	0.08 ± 0.28	-0.16 ± 0.34	-0.03 ± 0.10	$nan \pm nan$	-0.06 ± 0.07	$nan \pm nan$
NGC 2158	-0.25 ± 0.02	0.01 ± 0.13	0.04 ± 0.13	0.04 ± 0.04	0.04 ± 0.04	0.02 ± 0.03	0.05 ± 0.09	0.03 ± 0.07
	0.03 ± 0.03	-0.03 ± 0.04	-0.09 ± 0.37	-0.02 ± 0.11	-0.06 ± 0.03	-0.23 ± 0.35	-0.04 ± 0.02	0.14 ± 0.21
Berkeley 21	-0.23 ± 0.05	-0.00 ± 0.09	0.00 ± 0.14	0.08 ± 0.04	0.09 ± 0.04	-0.04 ± 0.04	0.02 ± 0.08	-0.01 ± 0.07
	0.02 ± 0.03	0.04 ± 0.04	0.04 ± 0.18	-0.06 ± 0.15	-0.04 ± 0.03	0.05 ± 0.18	-0.02 ± 0.03	0.25 ± 0.15
FSR 0937	-0.35 ± 0.03	0.02 ± 0.02	0.03 ± 0.10	0.06 ± 0.02	0.06 ± 0.04	0.02 ± 0.02	0.04 ± 0.06	0.14 ± 0.04
	0.03 ± 0.03	0.00 ± 0.03	0.02 ± 0.25	-0.10 ± 0.05	-0.02 ± 0.02	0.07 ± 0.08	-0.03 ± 0.02	0.15 ± 0.09
NGC 2304	-0.14 ± 0.01	0.01 ± 0.03	-0.13 ± 0.11	0.02 ± 0.01	-0.00 ± 0.05	0.01 ± 0.02	0.00 ± 0.05	0.07 ± 0.04
	0.05 ± 0.02	0.03 ± 0.03	-0.01 ± 0.13	0.05 ± 0.06	-0.04 ± 0.02	0.01 ± 0.11	-0.05 ± 0.03	0.25 ± 0.13
Teutsch 12	-0.20 ± 0.01	0.09 ± 0.05	0.02 ± 0.31	-0.00 ± 0.02	0.04 ± 0.03	0.00 ± 0.02	0.08 ± 0.06	0.01 ± 0.05
	0.01 ± 0.02	-0.06 ± 0.04	0.03 ± 0.17	-0.09 ± 0.08	-0.07 ± 0.02	-0.37 ± 0.43	-0.07 ± 0.02	0.29 ± 0.17
Berkeley 29	-0.53 ± 0.02	0.12 ± 0.01	0.13 ± 0.07	0.13 ± 0.02	0.02 ± 0.03	0.03 ± 0.02	0.15 ± 0.06	0.08 ± 0.05
	0.01 ± 0.02	0.08 ± 0.02	-0.18 ± 0.10	-0.01 ± 0.04	0.02 ± 0.02	0.15 ± 0.05	0.04 ± 0.02	0.11 ± 0.05
NGC 2420	-0.20 ± 0.04	0.07 ± 0.10	0.11 ± 0.27	0.04 ± 0.03	0.08 ± 0.09	0.03 ± 0.05	0.07 ± 0.08	0.04 ± 0.06
	0.04 ± 0.06	-0.05 ± 0.20	0.06 ± 0.17	-0.02 ± 0.24	-0.04 ± 0.08	-0.06 ± 0.17	-0.03 ± 0.03	0.16 ± 0.14
Berkeley 22	-0.33 ± 0.04	0.07 ± 0.03	0.15 ± 0.11	0.09 ± 0.02	0.16 ± 0.08	0.07 ± 0.02	0.03 ± 0.17	0.10 ± 0.11
	0.04 ± 0.03	0.02 ± 0.04	-0.03 ± 0.20	-0.11 ± 0.17	-0.01 ± 0.04	0.07 ± 0.12	-0.00 ± 0.04	0.07 ± 0.12
Briceno 1	-0.09 ± 0.06	-0.06 ± 0.03	-0.05 ± 0.47	-0.05 ± 0.04	0.13 ± 0.16	-0.03 ± 0.04	-0.04 ± 0.04	0.06 ± 0.05
	-0.05 ± 0.09	-0.22 ± 0.10	0.28 ± 0.10	-0.06 ± 0.20	-0.02 ± 0.11	$nan \pm nan$	-0.01 ± 0.02	$nan \pm nan$

Continued on next page

Table A.2 – Continued

Cluster name	[Fe/H] (dex)	[O/Fe] (dex)	[Na/Fe] (dex)	[Mg/Fe] (dex)	[Al/Fe] (dex)	[Si/Fe] (dex)	[S/Fe] (dex)	[K/Fe] (dex)
	[Ca/Fe] (dex)	[Ti/Fe] (dex)	[V/Fe] (dex)	[Cr/Fe] (dex)	[Mn/Fe] (dex)	[Co/Fe] (dex)	[Ni/Fe] (dex)	[Ce/Fe] (dex)
Trumpler 5	-0.45 ± 0.01	0.11 ± 0.03	-0.03 ± 0.44	0.10 ± 0.02	0.12 ± 0.04	0.05 ± 0.02	0.07 ± 0.06	0.13 ± 0.05
	0.05 ± 0.02	0.01 ± 0.03	0.12 ± 0.20	-0.03 ± 0.07	-0.06 ± 0.02	-0.14 ± 0.34	-0.00 ± 0.02	0.15 ± 0.10
Berkeley 20	-0.43 ± 0.01	0.10 ± 0.01	0.04 ± 0.07	0.09 ± 0.01	0.15 ± 0.02	0.09 ± 0.02	0.10 ± 0.05	0.11 ± 0.05
	0.05 ± 0.02	0.03 ± 0.02	-0.21 ± 0.07	-0.01 ± 0.04	-0.03 ± 0.02	-0.01 ± 0.05	0.03 ± 0.02	0.06 ± 0.05
NGC 2202	-0.46 ± 0.01	0.11 ± 0.06	0.37 ± 0.17	0.09 ± 0.02	0.25 ± 0.04	0.08 ± 0.03	0.05 ± 0.08	0.09 ± 0.10
	0.14 ± 0.03	0.05 ± 0.08	-0.11 ± 0.22	0.03 ± 0.10	-0.13 ± 0.05	0.08 ± 0.32	0.01 ± 0.03	0.26 ± 0.19
NGC 2632	0.14 ± 0.06	-0.03 ± 0.06	0.07 ± 0.15	-0.07 ± 0.06	0.03 ± 0.04	-0.01 ± 0.05	-0.06 ± 0.07	0.01 ± 0.09
	-0.01 ± 0.04	-0.09 ± 0.14	-0.00 ± 0.13	-0.12 ± 0.19	0.04 ± 0.03	$nan \pm nan$	0.00 ± 0.02	$nan \pm nan$
Berkeley 31	-0.43 ± 0.02	0.11 ± 0.02	0.10 ± 0.08	0.11 ± 0.02	0.05 ± 0.08	0.06 ± 0.02	0.08 ± 0.06	0.14 ± 0.05
	0.04 ± 0.02	0.05 ± 0.03	0.05 ± 0.15	-0.00 ± 0.05	-0.05 ± 0.03	0.04 ± 0.11	-0.02 ± 0.03	0.85 ± 0.10
NGC 2324	-0.22 ± 0.02	-0.03 ± 0.03	0.10 ± 0.07	0.00 ± 0.01	0.00 ± 0.03	-0.02 ± 0.01	0.11 ± 0.07	0.04 ± 0.04
	0.02 ± 0.02	0.04 ± 0.07	0.14 ± 0.19	-0.03 ± 0.04	-0.01 ± 0.01	-0.12 ± 0.19	-0.06 ± 0.02	0.39 ± 0.09
Saurer 1	-0.42 ± 0.01	0.09 ± 0.01	0.01 ± 0.07	0.09 ± 0.02	-0.02 ± 0.03	0.02 ± 0.02	0.25 ± 0.06	0.10 ± 0.05
	-0.04 ± 0.02	0.06 ± 0.02	-0.15 ± 0.07	0.03 ± 0.04	0.04 ± 0.02	0.12 ± 0.05	0.04 ± 0.02	0.04 ± 0.05
NGC 2682	-0.00 ± 0.05	0.03 ± 0.11	-0.06 ± 0.35	0.00 ± 0.06	0.06 ± 0.10	0.04 ± 0.07	0.01 ± 0.13	-0.00 ± 0.10
	-0.01 ± 0.04	-0.06 ± 0.19	-0.01 ± 0.25	-0.12 ± 0.29	0.01 ± 0.07	-0.02 ± 0.15	0.01 ± 0.05	-0.10 ± 0.12
FSR 1113	-0.35 ± 0.01	0.03 ± 0.04	0.15 ± 0.12	0.05 ± 0.02	0.05 ± 0.03	0.06 ± 0.02	0.21 ± 0.06	-0.10 ± 0.05
	0.04 ± 0.02	-0.05 ± 0.03	0.04 ± 0.15	0.03 ± 0.07	-0.10 ± 0.02	-0.68 ± 0.12	-0.05 ± 0.02	$nan \pm nan$
Berkeley 33	-0.24 ± 0.01	0.00 ± 0.01	0.13 ± 0.06	0.01 ± 0.01	0.02 ± 0.02	-0.01 ± 0.01	0.05 ± 0.04	-0.04 ± 0.04
	0.01 ± 0.01	-0.00 ± 0.02	-0.18 ± 0.06	-0.03 ± 0.03	0.01 ± 0.01	-0.01 ± 0.04	-0.05 ± 0.01	0.31 ± 0.05
NGC 2204	-0.29 ± 0.03	0.05 ± 0.05	0.01 ± 0.27	0.05 ± 0.02	0.04 ± 0.06	0.03 ± 0.02	-0.00 ± 0.14	0.05 ± 0.06
	0.02 ± 0.02	-0.05 ± 0.04	0.02 ± 0.19	-0.01 ± 0.16	-0.05 ± 0.03	0.04 ± 0.10	-0.04 ± 0.02	0.10 ± 0.24

Continued on next page

Table A.2 – Continued

Cluster name	[Fe/H] (dex)	[O/Fe] (dex)	[Na/Fe] (dex)	[Mg/Fe] (dex)	[Al/Fe] (dex)	[Si/Fe] (dex)	[S/Fe] (dex)	[K/Fe] (dex)
	[Ca/Fe] (dex)	[Ti/Fe] (dex)	[V/Fe] (dex)	[Cr/Fe] (dex)	[Mn/Fe] (dex)	[Co/Fe] (dex)	[Ni/Fe] (dex)	[Ce/Fe] (dex)
Czernik 30	-0.39 ± 0.01	0.10 ± 0.02	-0.15 ± 0.19	0.08 ± 0.02	0.13 ± 0.03	0.03 ± 0.02	0.20 ± 0.06	-0.00 ± 0.05
	0.01 ± 0.02	0.00 ± 0.03	-0.26 ± 0.10	-0.08 ± 0.06	-0.05 ± 0.02	0.07 ± 0.08	-0.00 ± 0.02	0.20 ± 0.08
Haffner 4	-0.18 ± 0.01	0.10 ± 0.05	-0.14 ± 0.13	0.01 ± 0.02	0.03 ± 0.03	-0.06 ± 0.02	0.13 ± 0.06	0.06 ± 0.05
	0.03 ± 0.02	0.01 ± 0.04	0.18 ± 0.18	-0.08 ± 0.08	-0.02 ± 0.02	-1.01 ± 0.15	-0.05 ± 0.02	0.43 ± 0.18
Melotte 71	-0.15 ± 0.02	0.03 ± 0.04	0.02 ± 0.07	-0.00 ± 0.01	0.03 ± 0.02	0.01 ± 0.01	0.07 ± 0.04	0.04 ± 0.04
	0.03 ± 0.01	0.00 ± 0.02	0.17 ± 0.10	0.05 ± 0.04	-0.02 ± 0.03	-0.17 ± 0.07	-0.03 ± 0.01	0.00 ± 0.11
Tombaugh 2	-0.37 ± 0.03	0.10 ± 0.11	0.06 ± 0.31	0.10 ± 0.02	0.05 ± 0.07	0.05 ± 0.03	0.11 ± 0.08	0.06 ± 0.06
	0.04 ± 0.03	-0.00 ± 0.04	0.01 ± 0.27	-0.04 ± 0.14	-0.02 ± 0.04	-0.16 ± 0.32	-0.01 ± 0.02	0.30 ± 0.35
Berkeley 75	-0.41 ± 0.01	0.15 ± 0.04	0.11 ± 0.13	0.14 ± 0.02	0.15 ± 0.03	0.07 ± 0.02	-0.00 ± 0.07	0.03 ± 0.06
	0.06 ± 0.03	0.01 ± 0.04	0.00 ± 0.22	-0.08 ± 0.08	-0.03 ± 0.04	0.00 ± 0.15	-0.01 ± 0.02	0.07 ± 0.13
NGC 2479	-0.05 ± 0.01	-0.05 ± 0.02	-0.01 ± 0.06	-0.01 ± 0.01	0.02 ± 0.02	0.00 ± 0.01	0.06 ± 0.03	-0.22 ± 0.03
	0.00 ± 0.01	-0.01 ± 0.02	0.14 ± 0.09	0.01 ± 0.04	0.00 ± 0.01	-0.02 ± 0.06	-0.02 ± 0.01	0.05 ± 0.09
NGC 2243	-0.46 ± 0.03	0.20 ± 0.12	-0.14 ± 0.26	0.10 ± 0.02	0.13 ± 0.05	0.08 ± 0.04	0.08 ± 0.08	0.18 ± 0.07
	0.10 ± 0.14	0.02 ± 0.04	0.06 ± 0.23	0.04 ± 0.09	-0.06 ± 0.03	-0.09 ± 0.46	0.03 ± 0.03	-0.10 ± 0.41
NGC 2447	-0.11 ± 0.01	0.01 ± 0.02	0.09 ± 0.07	0.01 ± 0.01	0.05 ± 0.02	0.02 ± 0.01	0.07 ± 0.03	-0.05 ± 0.04
	0.02 ± 0.01	-0.06 ± 0.02	0.15 ± 0.10	-0.02 ± 0.04	-0.03 ± 0.01	-0.05 ± 0.07	-0.05 ± 0.01	0.24 ± 0.09
ESO 211 03	-0.16 ± 0.03	0.05 ± 0.04	-0.02 ± 0.26	-0.00 ± 0.02	0.08 ± 0.03	-0.01 ± 0.02	0.02 ± 0.07	-0.04 ± 0.06
	0.02 ± 0.03	-0.06 ± 0.04	0.07 ± 0.16	-0.06 ± 0.07	-0.05 ± 0.02	-0.62 ± 0.50	-0.06 ± 0.02	0.23 ± 0.16
Ruprecht 82	-0.04 ± 0.01	-0.06 ± 0.02	0.20 ± 0.06	0.01 ± 0.01	0.01 ± 0.02	0.02 ± 0.01	0.07 ± 0.03	-0.05 ± 0.03
	0.01 ± 0.01	-0.05 ± 0.02	0.24 ± 0.09	-0.02 ± 0.04	0.01 ± 0.01	0.01 ± 0.06	-0.04 ± 0.01	0.18 ± 0.09
Ruprecht 85	-0.25 ± 0.01	0.04 ± 0.03	0.06 ± 0.08	0.03 ± 0.01	0.03 ± 0.03	0.03 ± 0.02	0.07 ± 0.04	-0.02 ± 0.04
	0.02 ± 0.01	-0.06 ± 0.03	0.11 ± 0.14	-0.06 ± 0.04	-0.00 ± 0.02	-0.09 ± 0.08	-0.04 ± 0.02	0.21 ± 0.07

Continued on next page

Table A.2 – Continued

Cluster name	[Fe/H] (dex)	[O/Fe] (dex)	[Na/Fe] (dex)	[Mg/Fe] (dex)	[Al/Fe] (dex)	[Si/Fe] (dex)	[S/Fe] (dex)	[K/Fe] (dex)
	[Ca/Fe] (dex)	[Ti/Fe] (dex)	[V/Fe] (dex)	[Cr/Fe] (dex)	[Mn/Fe] (dex)	[Co/Fe] (dex)	[Ni/Fe] (dex)	[Ce/Fe] (dex)
Collinder 220	-0.12 ± 0.01	0.00 ± 0.02	0.22 ± 0.06	-0.01 ± 0.01	-0.01 ± 0.02	0.01 ± 0.01	0.10 ± 0.03	-0.05 ± 0.04
	-0.01 ± 0.01	-0.03 ± 0.02	-0.06 ± 0.08	-0.05 ± 0.04	0.04 ± 0.01	0.03 ± 0.05	-0.06 ± 0.01	0.27 ± 0.07
SAI 116	0.14 ± 0.01	-0.02 ± 0.02	0.21 ± 0.08	-0.01 ± 0.02	0.00 ± 0.02	0.01 ± 0.01	-0.00 ± 0.06	-0.08 ± 0.04
	-0.04 ± 0.02	-0.00 ± 0.02	-0.29 ± 0.07	-0.06 ± 0.03	0.08 ± 0.03	0.04 ± 0.07	0.01 ± 0.01	-0.05 ± 0.08
NGC 4337	0.24 ± 0.03	-0.01 ± 0.02	0.29 ± 0.05	0.02 ± 0.01	0.04 ± 0.04	0.03 ± 0.02	-0.02 ± 0.05	-0.00 ± 0.06
	0.00 ± 0.03	0.08 ± 0.02	-0.04 ± 0.07	-0.03 ± 0.05	0.08 ± 0.04	0.08 ± 0.05	0.03 ± 0.01	-0.07 ± 0.08
BH 131	0.10 ± 0.01	-0.07 ± 0.03	0.23 ± 0.09	-0.04 ± 0.01	0.02 ± 0.06	0.01 ± 0.02	0.04 ± 0.03	-0.05 ± 0.03
	-0.03 ± 0.02	-0.00 ± 0.03	-0.17 ± 0.10	-0.04 ± 0.04	0.09 ± 0.02	0.01 ± 0.04	-0.02 ± 0.01	0.13 ± 0.08
Trumpler 20	0.11 ± 0.02	-0.03 ± 0.02	0.12 ± 0.06	-0.01 ± 0.01	0.03 ± 0.03	0.00 ± 0.01	-0.01 ± 0.05	-0.03 ± 0.04
	-0.01 ± 0.03	-0.03 ± 0.04	-0.06 ± 0.16	0.01 ± 0.04	0.02 ± 0.02	-0.02 ± 0.07	-0.03 ± 0.01	-0.05 ± 0.10
Teutsch 84	0.20 ± 0.01	-0.02 ± 0.03	0.17 ± 0.08	-0.01 ± 0.01	-0.01 ± 0.03	0.04 ± 0.02	-0.01 ± 0.04	-0.04 ± 0.04
	-0.01 ± 0.02	0.04 ± 0.03	0.03 ± 0.12	0.04 ± 0.05	0.04 ± 0.02	0.02 ± 0.10	0.03 ± 0.02	-0.29 ± 0.14
ESO 518 03	0.07 ± 0.05	0.01 ± 0.13	-0.18 ± 0.64	-0.02 ± 0.04	0.07 ± 0.05	0.06 ± 0.04	0.01 ± 0.07	-0.13 ± 0.29
	-0.04 ± 0.08	0.02 ± 0.27	-0.02 ± 0.17	-0.28 ± 0.46	0.03 ± 0.04	0.07 ± 0.04	0.00 ± 0.06	-0.10 ± 0.06

Appendix B

The APOGEE DR17 Globular Cluster Sample

This section contains the detailed tables for the APOGEE-based OCCAM DR17 sample of globular clusters presented in Chapter 5.1 .

Table B.1: Globular Cluster DR17 "High Quality" Sample Basic Parameters

Cluster name	Qual flag	l (deg)	b (deg)	R [a] (′)	Age [a] Gyr	R_{GC} [b] (kpc)	R_{Guide} [b] (kpc)	μ_α [c] (mas yr^{-1})	μ_δ [c] (mas yr^{-1})	RV (km s^{-1})	[Fe/H] (dex)	Num stars
NGC 6723	1	0.0695	−17.2987	5.0	13.493	2.59	0.03	$+0.87 \pm 0.03$	-2.44 ± 0.04	-93.3 ± 3.5	-1.02 ± 0.05	7
NGC 6569	1	0.4809	−6.6812	5.0	nan	2.85	2.28	-4.13 ± 0.04	-7.45 ± 0.04	-48.5 ± 4.9	-0.86 ± 0.38	13
NGC 6171	1	3.3733	+23.0102	5.2	13.477	3.48	0.83	-1.93 ± 0.03	-5.97 ± 0.03	-34.2 ± 2.8	-1.02 ± 0.11	60
NGC 5904	1	3.8583	+46.7967	5.3	12.007	6.32	1.81	$+4.06 \pm 0.03$	-9.86 ± 0.03	$+53.9 \pm 6.1$	-1.21 ± 0.08	110
NGC 6553	1	5.2525	−3.0296	5.0	nan	2.39	2.85	$+0.39 \pm 0.06$	-0.13 ± 0.07	$+0.3 \pm 5.8$	-0.19 ± 0.03	9
NGC 6715	1	5.6069	−14.0873	5.0	12.746	18.64	4.55	-2.69 ± 0.04	-1.36 ± 0.03	$+141.5 \pm 8.5$	-0.75 ± 0.49	82
NGC 6809	1	8.7924	−23.2719	8.5	13.498	4.06	1.11	-3.42 ± 0.02	-9.32 ± 0.02	$+175.1 \pm 3.7$	-1.76 ± 0.08	97
NGC 6642	1	9.8147	−6.4383	5.0	nan	1.68	0.02	-0.22 ± 0.08	-3.78 ± 0.09	-56.4 ± 3.5	-0.97 ± 0.40	12
NGC 6656	1	9.8921	−7.5520	10.1	13.497	5.20	4.32	$+9.77 \pm 0.03$	-5.62 ± 0.02	-147.0 ± 6.3	-1.71 ± 0.11	342
NGC 6254	1	15.1375	+23.0759	5.9	12.846	4.81	2.59	-4.79 ± 0.03	-6.61 ± 0.02	$+76.3 \pm 4.2$	-1.51 ± 0.07	85
NGC 6218	1	15.7147	+26.3131	5.3	13.496	4.79	2.49	-0.21 ± 0.03	-6.82 ± 0.03	-41.2 ± 3.1	-1.27 ± 0.06	82
NGC 6760	1	36.1073	−3.9243	5.0	nan	4.95	3.01	-1.07 ± 0.03	-3.62 ± 0.03	-0.3 ± 4.3	-0.75 ± 0.04	9
NGC 5466	1	42.1486	+73.5920	6.9	13.410	16.40	4.06	-5.33 ± 0.01	-0.81 ± 0.01	$+107.5 \pm 1.3$	-1.81 ± 0.09	17
NGC 5272	1	42.2156	+78.7072	6.9	12.585	12.17	4.57	-0.15 ± 0.02	-2.66 ± 0.01	-146.5 ± 4.1	-1.43 ± 0.10	141
NGC 7089	1	53.3714	−35.7700	5.0	13.271	10.42	0.64	$+3.38 \pm 0.04$	-2.28 ± 0.02	-3.6 ± 5.6	-1.47 ± 0.06	26
NGC 6838	1	56.7459	−4.5648	5.0	13.493	6.95	5.95	-3.41 ± 0.02	-2.68 ± 0.02	-22.6 ± 2.1	-0.75 ± 0.05	124
NGC 6205	1	59.0076	+40.9128	5.1	13.094	8.55	1.09	-3.11 ± 0.02	-2.58 ± 0.02	-245.9 ± 5.6	-1.48 ± 0.10	121
NGC 7078	1	65.0126	−27.3126	5.0	13.499	10.58	5.07	-0.65 ± 0.02	-3.83 ± 0.02	-106.8 ± 4.7	-2.29 ± 0.10	111

Continued on next page

Table B.1 – Continued

Cluster name	Qual flag	l deg	b deg	R[a] (′)	Age[b] Gyr	R_{GC}^{a} (kpc)	R_{Guide} [a] (kpc)	μ_α [c] (mas yr^{-1})	μ_δ [c] (mas yr^{-1})	RV (km s^{-1})	[Fe/H] (dex)	Num stars
NGC 6341	1	68.3385	+34.8588	5.0	13.498	9.79	0.36	-4.92 ± 0.02	-0.62 ± 0.02	-119.7 ± 4.7	-2.24 ± 0.08	67
NGC 6229	1	73.6389	+40.3065	5.0	nan	29.84	0.95	-1.16 ± 0.02	-0.47 ± 0.03	-138.0 ± 2.6	-1.24 ± 0.07	8
NGC 288	1	151.2657	−89.3810	6.7	nan	12.21	1.96	$+4.14 \pm 0.02$	-5.74 ± 0.02	-44.6 ± 2.1	-1.27 ± 0.06	43
NGC 1904	1	227.2288	−29.3515	5.0	nan	19.01	0.70	$+2.46 \pm 0.02$	-1.57 ± 0.02	$+206.2 \pm 3.8$	-1.51 ± 0.14	39
NGC 1851	1	244.5137	−35.0362	5.0	11.433	16.89	0.63	$+2.15 \pm 0.02$	-0.66 ± 0.02	$+320.1 \pm 5.9$	-1.13 ± 0.17	64
NGC 2298	1	245.6285	−16.0059	5.0	13.493	16.00	2.56	$+3.28 \pm 0.02$	-2.18 ± 0.02	$+146.6 \pm 3.1$	-1.83 ± 0.08	12
NGC 4147	1	252.8463	+77.1896	5.0	13.261	21.49	0.30	-1.69 ± 0.02	-2.10 ± 0.02	$+180.6 \pm 1.9$	-1.63 ± 0.06	3
NGC 3201	1	277.2283	+8.6406	9.3	12.836	9.08	12.35	$+8.35 \pm 0.02$	-1.97 ± 0.02	$+495.8 \pm 4.2$	-1.39 ± 0.14	172
NGC 2808	1	282.1927	−11.2522	5.0	11.092	11.30	2.12	$+0.96 \pm 0.03$	$+0.29 \pm 0.02$	$+103.3 \pm 8.6$	-1.06 ± 0.07	125
NGC 4590	1	299.6262	+36.0509	5.0	12.803	10.32	11.59	-2.76 ± 0.03	$+1.78 \pm 0.02$	-93.1 ± 2.6	-2.22 ± 0.09	35
NGC 362	1	301.5332	−46.2472	5.0	nan	9.54	0.17	$+6.73 \pm 0.02$	-2.58 ± 0.02	$+223.5 \pm 5.1$	-1.11 ± 0.06	69
NGC 104	1	305.8947	−44.8896	9.5	nan	7.60	5.90	$+5.16 \pm 0.03$	-2.65 ± 0.03	-17.6 ± 6.9	-0.74 ± 0.06	272
NGC 5139	1	309.1019	+14.9678	15.0	13.227	6.56	2.10	-3.27 ± 0.03	-6.70 ± 0.03	$+233.5 \pm 10.7$	-1.60 ± 0.25	1735
NGC 5024	1	332.9616	+79.7641	5.0	13.498	18.49	3.85	-0.15 ± 0.02	-1.32 ± 0.02	-62.4 ± 4.4	-1.90 ± 0.09	35
NGC 5053	1	335.6986	+78.9459	7.8	13.493	17.91	3.50	-0.34 ± 0.02	-1.22 ± 0.02	$+43.4 \pm 1.5$	-2.21 ± 0.11	17
NGC 6752	1	336.4924	−25.6284	5.7	13.202	5.45	4.06	-3.10 ± 0.03	-4.04 ± 0.03	-26.6 ± 4.6	-1.47 ± 0.14	119
NGC 6397	1	338.1652	−11.9592	8.7	13.496	6.26	3.26	$+3.19 \pm 0.03$	-17.65 ± 0.02	$+19.0 \pm 3.4$	-2.02 ± 0.07	166
NGC 6388	1	345.5561	−6.7381	5.0	11.240	2.99	1.12	-1.35 ± 0.04	-2.70 ± 0.04	$+81.5 \pm 7.1$	-0.48 ± 0.12	63

Continued on next page

Table B.1 – Continued

Cluster name	Qual flag	l deg	b deg	R[a] (′)	Age[b] Gyr	R_{GC}^{a} (kpc)	R_{Guide} [a] (kpc)	μ_α [c] (mas yr^{-1})	μ_δ [c] (mas yr^{-1})	RV (km s^{-1})	[Fe/H] (dex)	Num stars
NGC 6380	1	350.1818	−3.4205	5.0	nan	3.14	0.37	-2.11 ± 0.07	-3.28 ± 0.06	$+2.7 \pm 4.4$	-0.74 ± 0.18	21
Ton 2	1	350.7964	−3.4233	5.0	nan	1.41	1.44	-5.90 ± 0.07	-0.79 ± 0.05	-178.6 ± 2.9	-0.73 ± 0.26	13
NGC 6121	1	350.9729	+15.9718	13.0	12.966	6.22	0.09	-12.55 ± 0.03	-19.02 ± 0.03	$+71.1 \pm 3.4$	-1.08 ± 0.11	203
NGC 6304	1	355.8254	+5.3758	5.0	12.950	2.52	2.18	-4.08 ± 0.04	-1.04 ± 0.03	-109.0 ± 5.1	-0.49 ± 0.07	30
NGC 6273	1	356.8686	+9.3827	5.0	nan	1.56	0.76	-3.28 ± 0.03	$+1.67 \pm 0.03$	$+144.6 \pm 7.1$	-1.70 ± 0.13	78
NGC 6316	1	357.1752	+5.7649	5.0	nan	2.37	0.60	-4.91 ± 0.07	-4.66 ± 0.08	$+99.8 \pm 4.1$	-0.77 ± 0.04	19
NGC 6293	1	357.6205	+7.8340	5.0	nan	1.76	0.44	$+0.82 \pm 0.03$	-4.36 ± 0.03	-142.6 ± 5.6	-2.09 ± 0.08	20

[a] Cluster Radius and distances are from Harris (1996). Distances are recomputed to a solar radius of $R_0 = 8.274$ kpc.

[b] Ages are from Wagner-Kaiser et al. (2017).

[c] μ_α and μ_δ and their 1σ uncertainties are those of the 2D Gaussian fit, as in Donor et al. (2018).

Table B.2: Globular Cluster DR17 Sample - Detailed Chemistry

Cluster name	[Fe/H] (dex)	[O/Fe] (dex)	[Na/Fe] (dex)	[Mg/Fe] (dex)	[Al/Fe] (dex)	[Si/Fe] (dex)	[S/Fe] (dex)	[K/Fe] (dex)
	[Ca/Fe] (dex)	[Ti/Fe] (dex)	[V/Fe] (dex)	[Cr/Fe] (dex)	[Mn/Fe] (dex)	[Co/Fe] (dex)	[Ni/Fe] (dex)	[Ce/Fe] (dex)
NGC 6723	-1.02 ± 0.05	0.27 ± 0.06	0.12 ± 0.21	0.28 ± 0.04	0.20 ± 0.15	0.26 ± 0.04	0.37 ± 0.09	0.24 ± 0.07
	0.23 ± 0.05	0.07 ± 0.12	0.11 ± 0.34	-0.07 ± 0.21	-0.25 ± 0.03	-0.01 ± 0.12	0.01 ± 0.03	0.01 ± 0.11
NGC 6569	-0.86 ± 0.38	0.26 ± 0.10	0.16 ± 0.31	0.30 ± 0.08	0.29 ± 0.19	0.27 ± 0.10	0.35 ± 0.17	0.19 ± 0.15
	0.22 ± 0.14	0.14 ± 0.20	-0.22 ± 0.37	-0.03 ± 0.16	-0.18 ± 0.14	0.06 ± 0.31	0.02 ± 0.04	0.10 ± 0.23
NGC 6171	-1.02 ± 0.11	0.43 ± 0.17	-0.11 ± 0.62	0.33 ± 0.07	0.29 ± 0.13	0.33 ± 0.05	0.36 ± 0.16	0.33 ± 0.17
	0.25 ± 0.07	0.18 ± 0.19	-0.02 ± 0.36	-0.13 ± 0.31	-0.33 ± 0.15	0.02 ± 0.46	0.03 ± 0.10	0.17 ± 0.29
NGC 5904	-1.21 ± 0.08	0.21 ± 0.22	-0.10 ± 0.52	0.16 ± 0.08	0.17 ± 0.31	0.18 ± 0.05	0.34 ± 0.15	0.19 ± 0.24
	0.23 ± 0.10	0.08 ± 0.14	-0.05 ± 0.39	-0.07 ± 0.34	-0.35 ± 0.23	-0.14 ± 0.47	-0.07 ± 0.15	-0.07 ± 0.32
NGC 6553	-0.19 ± 0.03	0.17 ± 0.06	0.42 ± 0.17	0.22 ± 0.03	0.20 ± 0.06	0.10 ± 0.03	0.15 ± 0.11	0.33 ± 0.11
	0.06 ± 0.03	0.36 ± 0.16	0.08 ± 0.12	-0.05 ± 0.14	0.03 ± 0.05	0.10 ± 0.11	0.06 ± 0.02	0.13 ± 0.10
NGC 6715	-0.75 ± 0.49	0.02 ± 0.12	-0.16 ± 0.45	0.01 ± 0.12	-0.20 ± 0.41	-0.01 ± 0.13	0.14 ± 0.29	-0.03 ± 0.19
	0.04 ± 0.10	-0.08 ± 0.13	-0.28 ± 0.31	-0.02 ± 0.24	-0.20 ± 0.11	-0.18 ± 0.16	-0.13 ± 0.08	0.00 ± 0.32
NGC 6809	-1.76 ± 0.08	0.22 ± 0.18	-0.00 ± 0.53	0.29 ± 0.09	0.23 ± 0.41	0.24 ± 0.05	0.36 ± 0.26	0.40 ± 0.25
	0.14 ± 0.28	-0.01 ± 0.18	0.15 ± 0.43	0.17 ± 0.35	-0.28 ± 0.18	-0.10 ± 0.50	0.03 ± 0.09	-0.25 ± 0.27
NGC 6642	-0.97 ± 0.40	0.30 ± 0.09	0.22 ± 0.28	0.31 ± 0.08	0.21 ± 0.12	0.29 ± 0.10	0.38 ± 0.16	0.22 ± 0.09
	0.21 ± 0.08	0.11 ± 0.09	-0.11 ± 0.43	-0.04 ± 0.29	-0.26 ± 0.16	0.07 ± 0.17	0.03 ± 0.04	0.03 ± 0.16
NGC 6656	-1.71 ± 0.11	0.31 ± 0.19	0.32 ± 0.56	0.27 ± 0.09	0.32 ± 0.40	0.28 ± 0.07	0.43 ± 0.27	0.31 ± 0.35
	0.26 ± 0.26	0.06 ± 0.37	0.19 ± 0.50	0.08 ± 0.49	-0.35 ± 0.26	0.05 ± 0.56	-0.09 ± 0.17	-0.09 ± 0.40
NGC 6254	-1.51 ± 0.07	0.26 ± 0.18	-0.00 ± 0.51	0.23 ± 0.11	0.21 ± 0.47	0.25 ± 0.04	0.37 ± 0.20	-0.04 ± 0.34
	0.24 ± 0.14	-0.05 ± 0.16	0.05 ± 0.40	-0.19 ± 0.41	-0.18 ± 0.16	-0.25 ± 0.37	-0.03 ± 0.07	-0.39 ± 0.28
NGC 6218	-1.27 ± 0.06	0.30 ± 0.15	0.10 ± 0.51	0.32 ± 0.06	0.08 ± 0.17	0.27 ± 0.05	0.43 ± 0.20	0.25 ± 0.30
	0.26 ± 0.12	-0.00 ± 0.18	0.23 ± 0.53	-0.09 ± 0.42	-0.54 ± 0.25	-0.06 ± 0.46	-0.06 ± 0.18	-0.16 ± 0.39

Continued on next page

Table B.2 – Continued

Cluster name	[Fe/H] (dex)	[O/Fe] (dex)	[Na/Fe] (dex)	[Mg/Fe] (dex)	[Al/Fe] (dex)	[Si/Fe] (dex)	[S/Fe] (dex)	[K/Fe] (dex)
	[Ca/Fe] (dex)	[Ti/Fe] (dex)	[V/Fe] (dex)	[Cr/Fe] (dex)	[Mn/Fe] (dex)	[Co/Fe] (dex)	[Ni/Fe] (dex)	[Ce/Fe] (dex)
NGC 6760	-0.75 ± 0.04	0.29 ± 0.03	0.33 ± 0.07	0.31 ± 0.02	0.23 ± 0.10	0.20 ± 0.03	0.37 ± 0.07	0.34 ± 0.05
	0.18 ± 0.04	0.34 ± 0.09	0.13 ± 0.08	0.06 ± 0.05	-0.10 ± 0.03	0.27 ± 0.05	0.11 ± 0.02	0.16 ± 0.05
NGC 5466	-1.81 ± 0.09	0.16 ± 0.07	0.49 ± 0.72	0.13 ± 0.11	-0.26 ± 0.30	0.13 ± 0.08	-0.10 ± 0.50	-0.13 ± 0.39
	0.06 ± 0.20	-0.26 ± 0.14	0.21 ± 0.47	0.06 ± 0.37	-0.20 ± 0.12	0.31 ± 0.50	-0.13 ± 0.21	-0.49 ± 0.12
NGC 5272	-1.43 ± 0.10	0.21 ± 0.18	0.19 ± 0.49	0.13 ± 0.09	0.02 ± 0.36	0.20 ± 0.11	0.24 ± 0.27	0.21 ± 0.27
	0.17 ± 0.15	0.06 ± 0.33	-0.17 ± 0.46	-0.15 ± 0.41	-0.40 ± 0.17	-0.22 ± 0.55	-0.14 ± 0.12	-0.28 ± 0.35
NGC 7089	-1.47 ± 0.06	0.19 ± 0.20	-0.08 ± 0.47	0.11 ± 0.09	0.24 ± 0.40	0.18 ± 0.04	0.26 ± 0.22	-0.03 ± 0.41
	0.20 ± 0.10	0.02 ± 0.09	-0.01 ± 0.37	-0.22 ± 0.30	-0.30 ± 0.08	-0.12 ± 0.45	-0.08 ± 0.08	-0.18 ± 0.21
NGC 6838	-0.75 ± 0.05	0.34 ± 0.13	-0.13 ± 0.59	0.33 ± 0.03	0.23 ± 0.08	0.24 ± 0.06	0.35 ± 0.15	0.27 ± 0.12
	0.19 ± 0.07	0.16 ± 0.12	0.01 ± 0.36	-0.17 ± 0.37	-0.24 ± 0.09	0.04 ± 0.38	0.06 ± 0.04	0.00 ± 0.29
NGC 6205	-1.48 ± 0.10	0.13 ± 0.24	0.41 ± 0.40	0.07 ± 0.15	0.41 ± 0.43	0.19 ± 0.07	0.34 ± 0.23	0.23 ± 0.33
	0.24 ± 0.14	0.00 ± 0.20	0.16 ± 0.48	-0.00 ± 0.38	-0.33 ± 0.26	-0.03 ± 0.55	-0.03 ± 0.14	-0.12 ± 0.35
NGC 7078	-2.29 ± 0.10	0.33 ± 0.33	0.66 ± 0.62	0.19 ± 0.25	0.31 ± 0.34	0.35 ± 0.09	0.36 ± 0.44	0.65 ± 0.43
	0.31 ± 0.42	0.20 ± 0.48	0.72 ± 0.53	0.37 ± 0.51	0.31 ± 0.32	0.67 ± 0.56	0.12 ± 0.24	0.30 ± 0.46
NGC 6341	-2.24 ± 0.08	0.32 ± 0.28	0.66 ± 0.60	0.17 ± 0.21	0.36 ± 0.35	0.34 ± 0.07	0.46 ± 0.36	0.54 ± 0.36
	0.27 ± 0.42	0.27 ± 0.43	0.30 ± 0.41	0.22 ± 0.35	0.23 ± 0.20	0.53 ± 0.52	0.08 ± 0.19	0.29 ± 0.31
NGC 6229	-1.24 ± 0.07	0.18 ± 0.12	-0.13 ± 0.46	0.15 ± 0.07	-0.06 ± 0.25	0.17 ± 0.10	0.49 ± 0.25	0.26 ± 0.11
	0.23 ± 0.06	-0.04 ± 0.16	-0.34 ± 0.42	-0.37 ± 0.32	-0.28 ± 0.04	-0.09 ± 0.14	-0.12 ± 0.08	-0.03 ± 0.34
NGC 288	-1.27 ± 0.06	0.39 ± 0.11	0.13 ± 0.41	0.30 ± 0.04	0.17 ± 0.14	0.32 ± 0.04	0.42 ± 0.17	0.26 ± 0.14
	0.21 ± 0.17	0.01 ± 0.11	-0.04 ± 0.38	-0.13 ± 0.35	-0.38 ± 0.16	-0.11 ± 0.38	-0.02 ± 0.04	-0.01 ± 0.14
NGC 1904	-1.51 ± 0.14	0.14 ± 0.17	0.26 ± 0.49	0.11 ± 0.11	0.17 ± 0.47	0.16 ± 0.06	0.31 ± 0.24	0.18 ± 0.26
	0.15 ± 0.19	-0.04 ± 0.15	0.10 ± 0.39	-0.17 ± 0.39	-0.40 ± 0.20	-0.00 ± 0.42	-0.04 ± 0.26	-0.27 ± 0.18

Continued on next page

Table B.2 – Continued

Cluster name	[Fe/H] (dex)	[O/Fe] (dex)	[Na/Fe] (dex)	[Mg/Fe] (dex)	[Al/Fe] (dex)	[Si/Fe] (dex)	[S/Fe] (dex)	[K/Fe] (dex)
	[Ca/Fe] (dex)	[Ti/Fe] (dex)	[V/Fe] (dex)	[Cr/Fe] (dex)	[Mn/Fe] (dex)	[Co/Fe] (dex)	[Ni/Fe] (dex)	[Ce/Fe] (dex)
NGC 1851	-1.13 ± 0.17	0.23 ± 0.25	0.19 ± 0.60	0.23 ± 0.14	-0.03 ± 0.35	0.18 ± 0.14	0.36 ± 0.22	0.40 ± 0.47
	0.26 ± 0.14	0.09 ± 0.19	-0.02 ± 0.48	0.10 ± 0.66	-0.28 ± 0.26	-0.20 ± 0.47	0.04 ± 0.22	0.20 ± 0.50
NGC 2298	-1.83 ± 0.08	0.21 ± 0.23	0.50 ± 0.31	0.16 ± 0.13	0.05 ± 0.48	0.26 ± 0.04	0.26 ± 0.30	0.35 ± 0.28
	0.20 ± 0.23	-0.17 ± 0.14	0.29 ± 0.48	0.04 ± 0.34	-0.27 ± 0.18	-0.07 ± 0.42	-0.06 ± 0.12	-0.23 ± 0.33
NGC 4147	-1.63 ± 0.06	0.32 ± 0.05	0.33 ± 0.36	0.26 ± 0.04	0.07 ± 0.35	0.22 ± 0.04	0.37 ± 0.18	-0.08 ± 0.53
	0.15 ± 0.06	-0.11 ± 0.11	0.35 ± 0.36	-0.03 ± 0.25	-0.14 ± 0.33	0.10 ± 0.48	-0.08 ± 0.06	-0.40 ± 0.31
NGC 3201	-1.39 ± 0.14	0.16 ± 0.25	-0.03 ± 0.55	0.19 ± 0.08	-0.12 ± 0.33	0.16 ± 0.06	0.36 ± 0.22	0.37 ± 0.27
	0.21 ± 0.17	0.03 ± 0.22	0.07 ± 0.48	-0.13 ± 0.62	-0.12 ± 0.26	-0.13 ± 0.56	-0.06 ± 0.15	-0.23 ± 0.50
NGC 2808	-1.06 ± 0.07	0.14 ± 0.18	0.04 ± 0.41	0.07 ± 0.17	0.25 ± 0.47	0.17 ± 0.05	0.28 ± 0.20	0.25 ± 0.19
	0.17 ± 0.09	0.02 ± 0.13	-0.06 ± 0.39	-0.05 ± 0.28	-0.25 ± 0.13	-0.06 ± 0.31	-0.04 ± 0.08	-0.08 ± 0.29
NGC 4590	-2.22 ± 0.09	0.30 ± 0.16	0.68 ± 0.69	0.27 ± 0.09	0.21 ± 0.36	0.32 ± 0.06	0.46 ± 0.41	0.75 ± 0.31
	0.08 ± 0.38	-0.09 ± 0.30	0.66 ± 0.40	0.35 ± 0.36	0.08 ± 0.19	0.49 ± 0.42	0.13 ± 0.21	0.06 ± 0.28
NGC 362	-1.11 ± 0.06	0.16 ± 0.15	0.03 ± 0.50	0.10 ± 0.07	0.02 ± 0.25	0.13 ± 0.04	0.31 ± 0.17	0.13 ± 0.17
	0.19 ± 0.08	-0.02 ± 0.10	-0.16 ± 0.44	0.00 ± 0.24	-0.31 ± 0.13	-0.22 ± 0.33	-0.07 ± 0.09	-0.05 ± 0.26
NGC 104	-0.74 ± 0.06	0.30 ± 0.13	0.12 ± 0.39	0.35 ± 0.04	0.34 ± 0.12	0.25 ± 0.04	0.34 ± 0.10	0.26 ± 0.10
	0.19 ± 0.06	0.19 ± 0.11	0.03 ± 0.32	-0.05 ± 0.26	-0.20 ± 0.08	-0.03 ± 0.42	0.06 ± 0.05	-0.08 ± 0.25
NGC 5139	-1.60 ± 0.25	0.31 ± 0.24	0.29 ± 0.56	0.25 ± 0.20	0.29 ± 0.52	0.30 ± 0.08	0.42 ± 0.25	0.23 ± 0.33
	0.27 ± 0.21	0.01 ± 0.22	0.13 ± 0.45	0.12 ± 0.42	-0.33 ± 0.25	-0.09 ± 0.50	-0.04 ± 0.13	0.10 ± 0.48
NGC 5024	-1.90 ± 0.09	0.31 ± 0.09	0.25 ± 0.73	0.26 ± 0.09	0.13 ± 0.42	0.24 ± 0.07	0.40 ± 0.38	0.42 ± 0.40
	0.39 ± 0.16	-0.23 ± 0.21	0.22 ± 0.46	0.13 ± 0.44	-0.19 ± 0.19	0.20 ± 0.48	0.00 ± 0.14	-0.22 ± 0.19
NGC 5053	-2.21 ± 0.11	0.35 ± 0.26	0.58 ± 0.63	0.27 ± 0.13	0.29 ± 0.41	0.33 ± 0.07	0.20 ± 0.62	0.54 ± 0.41
	0.38 ± 0.34	0.10 ± 0.37	0.79 ± 0.38	0.20 ± 0.35	0.08 ± 0.26	0.59 ± 0.58	-0.07 ± 0.18	-0.03 ± 0.26

Continued on next page

Table B.2 – Continued

Cluster name	[Fe/H] (dex)	[O/Fe] (dex)	[Na/Fe] (dex)	[Mg/Fe] (dex)	[Al/Fe] (dex)	[Si/Fe] (dex)	[S/Fe] (dex)	[K/Fe] (dex)
	[Ca/Fe] (dex)	[Ti/Fe] (dex)	[V/Fe] (dex)	[Cr/Fe] (dex)	[Mn/Fe] (dex)	[Co/Fe] (dex)	[Ni/Fe] (dex)	[Ce/Fe] (dex)
NGC 6752	-1.47 ± 0.14	0.17 ± 0.28	-0.09 ± 0.67	0.21 ± 0.11	0.40 ± 0.44	0.24 ± 0.05	0.37 ± 0.18	0.09 ± 0.36
	0.23 ± 0.17	-0.03 ± 0.19	-0.02 ± 0.46	-0.09 ± 0.42	-0.41 ± 0.24	-0.07 ± 0.53	-0.00 ± 0.10	0.01 ± 0.26
NGC 6397	-2.02 ± 0.07	0.29 ± 0.23	0.49 ± 0.56	0.30 ± 0.10	0.29 ± 0.37	0.30 ± 0.06	0.40 ± 0.37	0.38 ± 0.39
	0.29 ± 0.34	0.06 ± 0.39	0.45 ± 0.48	0.30 ± 0.52	0.03 ± 0.23	0.39 ± 0.51	0.04 ± 0.20	0.05 ± 0.40
NGC 6388	-0.48 ± 0.12	0.06 ± 0.06	0.14 ± 0.35	0.08 ± 0.06	0.23 ± 0.27	0.05 ± 0.08	0.14 ± 0.20	0.06 ± 0.16
	0.03 ± 0.07	0.13 ± 0.17	-0.14 ± 0.34	-0.01 ± 0.18	-0.04 ± 0.07	0.07 ± 0.34	-0.03 ± 0.06	0.09 ± 0.25
NGC 6380	-0.74 ± 0.18	0.26 ± 0.09	0.36 ± 0.21	0.32 ± 0.06	0.45 ± 0.26	0.24 ± 0.08	0.35 ± 0.19	0.29 ± 0.10
	0.24 ± 0.09	0.33 ± 0.20	0.12 ± 0.34	-0.01 ± 0.13	-0.17 ± 0.10	0.13 ± 0.26	0.05 ± 0.03	0.11 ± 0.18
Ton 2	-0.73 ± 0.26	0.26 ± 0.09	0.27 ± 0.17	0.31 ± 0.07	0.40 ± 0.12	0.22 ± 0.09	0.32 ± 0.11	0.29 ± 0.09
	0.20 ± 0.06	0.24 ± 0.13	0.04 ± 0.28	0.07 ± 0.17	-0.20 ± 0.08	0.09 ± 0.34	0.05 ± 0.03	0.07 ± 0.11
NGC 6121	-1.08 ± 0.11	0.40 ± 0.10	0.05 ± 0.51	0.36 ± 0.05	0.43 ± 0.13	0.39 ± 0.06	0.38 ± 0.11	0.27 ± 0.13
	0.26 ± 0.13	0.10 ± 0.15	-0.01 ± 0.36	0.04 ± 0.28	-0.23 ± 0.13	-0.03 ± 0.36	0.05 ± 0.06	0.17 ± 0.29
NGC 6304	-0.49 ± 0.07	0.25 ± 0.12	0.15 ± 0.58	0.31 ± 0.05	0.32 ± 0.12	0.21 ± 0.04	0.30 ± 0.15	0.40 ± 0.11
	0.17 ± 0.05	0.22 ± 0.15	-0.01 ± 0.54	-0.27 ± 0.42	-0.12 ± 0.07	0.18 ± 0.27	0.06 ± 0.05	0.02 ± 0.17
NGC 6273	-1.70 ± 0.13	0.17 ± 0.16	0.16 ± 0.62	0.18 ± 0.11	0.37 ± 0.42	0.23 ± 0.07	0.39 ± 0.27	0.25 ± 0.35
	0.25 ± 0.23	0.01 ± 0.16	0.22 ± 0.50	-0.02 ± 0.42	-0.18 ± 0.23	-0.09 ± 0.45	0.03 ± 0.16	0.07 ± 0.43
NGC 6316	-0.77 ± 0.04	0.27 ± 0.04	0.17 ± 0.22	0.29 ± 0.05	0.24 ± 0.15	0.25 ± 0.05	0.38 ± 0.23	0.16 ± 0.14
	0.18 ± 0.05	0.17 ± 0.12	-0.13 ± 0.28	-0.03 ± 0.19	-0.07 ± 0.07	0.15 ± 0.14	0.06 ± 0.03	0.07 ± 0.14
NGC 6293	-2.09 ± 0.08	0.20 ± 0.23	0.68 ± 0.60	0.15 ± 0.16	0.40 ± 0.37	0.31 ± 0.09	0.47 ± 0.37	0.40 ± 0.43
	0.13 ± 0.56	0.31 ± 0.51	0.70 ± 0.56	0.25 ± 0.47	0.01 ± 0.21	0.25 ± 0.51	0.05 ± 0.20	-0.18 ± 0.17

Bibliography

Abdurro'uf, Accetta, K., Aerts, C., Silva Aguirre, V., Ahumada, R., Ajgaonkar, N., Filiz Ak, N., Alam, S., Allende Prieto, C., Almeida, A., Anders, F., Anderson, S. F., Andrews, B. H., Anguiano, B., Aquino-Ortíz, E., Aragón-Salamanca, A., Argudo-Fernández, M., Ata, M., Aubert, M., Avila-Reese, V., Badenes, C., Barbá, R. H., Barger, K., Barrera-Ballesteros, J. K., Beaton, R. L., Beers, T. C., Belfiore, F., Bender, C. F., Bernardi, M., Bershady, M. A., Beutler, F., Bidin, C. M., Bird, J. C., Bizyaev, D., Blanc, G. A., Blanton, M. R., Boardman, N. F., Bolton, A. S., Boquien, M., Borissova, J., Bovy, J., Brandt, W. N., Brown, J., Brownstein, J. R., Brusa, M., Buchner, J., Bundy, K., Burchett, J. N., Bureau, M., Burgasser, A., Cabang, T. K., Campbell, S., Cappellari, M., Carlberg, J. K., Wanderley, F. C., Carrera, R., Cash, J., Chen, Y.-P., Chen, W.-H., Cherinka, B., Chiappini, C., Choi, P. D., Chojnowski, S. D., Chung, H., Clerc, N., Cohen, R. E., Comerford, J. M., Comparat, J., da Costa, L., Covey, K., Crane, J. D., Cruz-Gonzalez, I., Culhane, C., Cunha, K., Dai, Y. S., Damke, G., Darling, J., Davidson, James W., J., Davies, R., Dawson, K., De Lee, N., Diamond-Stanic, A. M., Cano-Díaz, M., Sánchez, H. D., Donor, J., Duckworth, C., Dwelly, T., Eisenstein, D. J., Elsworth, Y. P., Emsellem, E., Eracleous, M., Escoffier, S., Fan, X., Farr, E., Feng, S., Fernández-Trincado, J. G., Feuillet, D., Filipp, A., Fillingham, S. P., Frinchaboy, P. M., Fromenteau, S., Galbany, L., García, R. A., García-Hernández, D. A., Ge, J., Geisler, D., Gelfand, J., Géron, T., Gibson, B. J., Goddy, J., Godoy-Rivera, D., Grabowski, K., Green, P. J., Greener, M., Grier, C. J., Griffith, E., Guo, H., Guy, J., Hadjara, M., Harding, P., Hasselquist, S., Hayes, C. R., Hearty, F., Hernández, J., Hill, L., Hogg, D. W., Holtzman, J. A., Horta, D., Hsieh, B.-C., Hsu, C.-H., Hsu, Y.-H., Huber, D., Huertas-Company, M., Hutchinson, B., Hwang, H. S., Ibarra-Medel, H. J., Chitham, J. I., Ilha, G. S., Imig, J., Jaekle, W., Jayasinghe, T., Ji, X., Johnson, J. A., Jones, A., Jönsson, H., Katkov, I., Khalatyan, Arman, D., Kinemuchi, K., Kisku, S., Knapen, J. H., Kneib, J.-P., Kollmeier, J. A., Kong, M., Kounkel, M., Kreckel, K., Krishnarao, D., Lacerna, I., Lane, R. R., Langgin, R., Lavender, R., Law, D. R., Lazarz, D., Leung, H. W., Leung, H.-H., Lewis, H. M., Li, C., Li, R., Lian, J., Liang, F.-H., Lin, L., Lin, Y.-T., Lin, S., Lintott, C., Long, D., Longa-Peña, P., López-Cobá, C., Lu, S., Lundgren, B. F., Luo, Y., Mackereth, J. T., de la Macorra, A., Mahadevan, S., Majewski, S. R., Manchado, A., Mandeville, T., Maraston, C., Margalef-Bentabol, B., Masseron, T., Masters, K. L., Mathur, S., McDermid, R. M., Mckay, M., Merloni, A., Merrifield, M., Meszaros, S., Miglio, A., Di Mille, F., Minniti, D., Minsley, R., Monachesi, A., Moon, J., Mosser, B., Mulchaey, J., Muna, D., Muñoz, R. R., Myers, A. D., Myers, N., Nadathur, S., Nair, P., Nandra, K.,

Neumann, J., Newman, J. A., Nidever, D. L., Nikakhtar, F., Nitschelm, C., O'Connell, J. E., Garma-Oehmichen, L., Luan Souza de Oliveira, G., Olney, R., Oravetz, D., Ortigoza-Urdaneta, M., Osorio, Y., Otter, J., Pace, Z. J., Padilla, N., Pan, K., Pan, H.-A., Parikh, T., Parker, J., Peirani, S., Peña Ramírez, K., Penny, S., Percival, W. J., Perez-Fournon, I., Pinsonneault, M., Poidevin, F., Poovelil, V. J., Price-Whelan, A. M., Bárbara de Andrade Queiroz, A., Raddick, M. J., Ray, A., Rembold, S. B., Riddle, N., Riffel, R. A., Riffel, R., Rix, H.-W., Robin, A. C., Rodríguez-Puebla, A., Roman-Lopes, A., Román-Zúñiga, C., Rose, B., Ross, A. J., Rossi, G., Rubin, K. H. R., Salvato, M., Sánchez, S. F., Sánchez-Gallego, J. R., Sanderson, R., Santana Rojas, F. A., Sarceno, E., Sarmiento, R., Sayres, C., Sazonova, E., Schaefer, A. L., Schiavon, R., Schlegel, D. J., Schneider, D. P., Schultheis, M., Schwope, A., Serenelli, A., Serna, J., Shao, Z., Shapiro, G., Sharma, A., Shen, Y., Shetrone, M., Shu, Y., Simon, J. D., Skrutskie, M. F., Smethurst, R., Smith, V., Sobeck, J., Spoo, T., Sprague, D., Stark, D. V., Stassun, K. G., Steinmetz, M., Stello, D., Stone-Martinez, A., Storchi-Bergmann, T., Stringfellow, G. S., Stutz, A., Su, Y.-C., Taghizadeh-Popp, M., Talbot, M. S., Tayar, J., Telles, E., Teske, J., Thakar, A., Theissen, C., Tkachenko, A., Thomas, D., Tojeiro, R., Hernandez Toledo, H., Troup, N. W., Trump, J. R., Trussler, J., Turner, J., Tuttle, S., Unda-Sanzana, E., Vázquez-Mata, J. A., Valentini, M., Valenzuela, O., Vargas-González, J., Vargas-Magaña, M., Alfaro, P. V., Villanova, S., Vincenzo, F., Wake, D., Warfield, J. T., Washington, J. D., Weaver, B. A., Weijmans, A.-M., Weinberg, D. H., Weiss, A., Westfall, K. B., Wild, V., Wilde, M. C., Wilson, J. C., Wilson, R. F., Wilson, M., Wolf, J., Wood-Vasey, W. M., Yan, R., Zamora, O., Zasowski, G., Zhang, K., Zhao, C., Zheng, Z., Zheng, Z., & Zhu, K. 2022, Astrophysical Journal Supplement, 259, 35

Ahumada, R., Prieto, C. A., Almeida, A., Anders, F., Anderson, S. F., Andrews, B. H., Anguiano, B., Arcodia, R., Armengaud, E., Aubert, M., Avila, S., Avila-Reese, V., Badenes, C., Balland, C., Barger, K., Barrera-Ballesteros, J. K., Basu, S., Bautista, J., Beaton, R. L., Beers, T. C., Benavides, B. I. T., Bender, C. F., Bernardi, M., Bershady, M., Beutler, F., Bidin, C. M., Bird, J., Bizyaev, D., Blanc, G. A., Blanton, M. R., Boquien, M., Borissova, J., Bovy, J., Brandt, W. N., Brinkmann, J., Brownstein, J. R., Bundy, K., Bureau, M., Burgasser, A., Burtin, E., Cano-Díaz, M., Capasso, R., Cappellari, M., Carrera, R., Chabanier, S., Chaplin, W., Chapman, M., Cherinka, B., Chiappini, C., Doohyun Choi, P., Chojnowski, S. D., Chung, H., Clerc, N., Coffey, D., Comerford, J. M., Comparat, J., da Costa, L., Cousinou, M.-C., Covey, K., Crane, J. D., Cunha, K., Ilha, G. d. S., Dai, Y. S., Damsted, S. B., Darling, J., Davidson, James W., J., Davies, R., Dawson, K., De, N., de la Macorra, A., De Lee, N., Queiroz, A. B. d. A., Deconto Machado, A., de la Torre, S., Dell'Agli, F., du Mas des Bourboux, H., Diamond-Stanic, A. M., Dillon, S., Donor, J., Drory, N., Duckworth, C., Dwelly, T., Ebelke, G., Eftekharzadeh, S., Davis Eigenbrot, A., Elsworth, Y. P., Eracleous, M., Erfanianfar, G., Escoffier, S., Fan, X., Farr, E., Fernández-Trincado, J. G., Feuillet, D., Finoguenov, A., Fofie, P., Fraser-McKelvie, A., Frinchaboy, P. M., Fromenteau, S., Fu, H., Galbany, L., Garcia, R. A., García-Hernández, D. A., Oehmichen, L. A. G., Ge, J., Maia, M. A. G., Geisler, D., Gelfand, J., Goddy, J., Gonzalez-Perez, V., Grabowski, K., Green, P., Grier, C. J., Guo, H., Guy, J., Harding, P., Hasselquist, S., Hawken, A. J.,

Hayes, C. R., Hearty, F., Hekker, S., Hogg, D. W., Holtzman, J. A., Horta, D., Hou, J., Hsieh, B.-C., Huber, D., Hunt, J. A. S., Chitham, J. I., Imig, J., Jaber, M., Angel, C. E. J., Johnson, J. A., Jones, A. M., Jönsson, H., Jullo, E., Kim, Y., Kinemuchi, K., Kirkpatrick, Charles C., I., Kite, G. W., Klaene, M., Kneib, J.-P., Kollmeier, J. A., Kong, H., Kounkel, M., Krishnarao, D., Lacerna, I., Lan, T.-W., Lane, R. R., Law, D. R., Le Goff, J.-M., Leung, H. W., Lewis, H., Li, C., Lian, J., Lin, L., Long, D., Longa-Peña, P., Lundgren, B., Lyke, B. W., Ted Mackereth, J., MacLeod, C. L., Majewski, S. R., Manchado, A., Maraston, C., Martini, P., Masseron, T., Masters, K. L., Mathur, S., McDermid, R. M., Merloni, A., Merrifield, M., Mészáros, S., Miglio, A., Minniti, D., Minsley, R., Miyaji, T., Mohammad, F. G., Mosser, B., Mueller, E.-M., Muna, D., Muñoz-Gutiérrez, A., Myers, A. D., Nadathur, S., Nair, P., Nandra, K., do Nascimento, J. C., Nevin, R. J., Newman, J. A., Nidever, D. L., Nitschelm, C., Noterdaeme, P., O'Connell, J. E., Olmstead, M. D., Oravetz, D., Oravetz, A., Osorio, Y., Pace, Z. J., Padilla, N., Palanque-Delabrouille, N., Palicio, P. A., Pan, H.-A., Pan, K., Parker, J., Paviot, R., Peirani, S., Ramŕez, K. P., Penny, S., Percival, W. J., Perez-Fournon, I., Pérez-Ràfols, I., Petitjean, P., Pieri, M. M., Pinsonneault, M., Poovelil, V. J., Povick, J. T., Prakash, A., Price-Whelan, A. M., Raddick, M. J., Raichoor, A., Ray, A., Rembold, S. B., Rezaie, M., Riffel, R. A., Riffel, R., Rix, H.-W., Robin, A. C., Roman-Lopes, A., Román-Zúñiga, C., Rose, B., Ross, A. J., Rossi, G., Rowlands, K., Rubin, K. H. R., Salvato, M., Sánchez, A. G., Sánchez-Menguiano, L., Sánchez-Gallego, J. R., Sayres, C., Schaefer, A., Schiavon, R. P., Schimoia, J. S., Schlafly, E., Schlegel, D., Schneider, D. P., Schultheis, M., Schwope, A., Seo, H.-J., Serenelli, A., Shafieloo, A., Shamsi, S. J., Shao, Z., Shen, S., Shetrone, M., Shirley, R., Aguirre, V. S., Simon, J. D., Skrutskie, M. F., Slosar, A., Smethurst, R., Sobeck, J., Sodi, B. C., Souto, D., Stark, D. V., Stassun, K. G., Steinmetz, M., Stello, D., Stermer, J., Storchi-Bergmann, T., Streblyanska, A., Stringfellow, G. S., Stutz, A., Suárez, G., Sun, J., Taghizadeh-Popp, M., Talbot, M. S., Tayar, J., Thakar, A. R., Theriault, R., Thomas, D., Thomas, Z. C., Tinker, J., Tojeiro, R., Toledo, H. H., Tremonti, C. A., Troup, N. W., Tuttle, S., Unda-Sanzana, E., Valentini, M., Vargas-González, J., Vargas-Magaña, M., Vázquez-Mata, J. A., Vivek, M., Wake, D., Wang, Y., Weaver, B. A., Weijmans, A.-M., Wild, V., Wilson, J. C., Wilson, R. F., Wolthuis, N., Wood-Vasey, W. M., Yan, R., Yang, M., Yèche, C., Zamora, O., Zarrouk, P., Zasowski, G., Zhang, K., Zhao, C., Zhao, G., Zheng, Z., Zheng, Z., Zhu, G., & Zou, H. 2020, Astrophysical Journal Supplement, 249, 3

Andrews, S., Fryer, C., Even, W., Jones, S., & Pignatari, M. 2020, The Astrophysical Journal, 890, 35

Baumgardt, H., Hilker, M., Sollima, A., & Bellini, A. 2019, Monthly Notices of the Royal Astronomy Society, 482, 5138

Beaton, R. L., Oelkers, R. J., Hayes, C. R., Covey, K. R., Chojnowski, S. D., De Lee, N., Sobeck, J. S., Majewski, S. R., Cohen, R. E., Fernández-Trincado, J., Longa-Peña, P., O'Connell, J. E., Santana, F. A., Stringfellow, G. S., Zasowski, G., Aerts, C., Anguiano, B., Bender, C., Cañas, C. I., Cunha, K., Donor, J., Fleming, S. W., Frinchaboy, P. M., Feuillet, D., Harding, P., Hasselquist, S., Holtzman, J. A., Johnson, J. A.,

Kollmeier, J. A., Kounkel, M., Mahadevan, S., Price-Whelan, A. M., Rojas-Arriagada, A., Román-Zúñiga, C., Schlafly, E. F., Schultheis, M., Shetrone, M., Simon, J. D., Stassun, K. G., Stutz, A. M., Tayar, J., Teske, J., Tkachenko, A., Troup, N., Albareti, F. D., Bizyaev, D., Bovy, J., Burgasser, A. J., Comparat, J., Downes, J. J., Geisler, D., Inno, L., Manchado, A., Ness, M. K., Pinsonneault, M. H., Prada, F., Roman-Lopes, A., Simonian, G. V. A., Smith, V. V., Yan, R., & Zamora, O. 2021, The Astronomical Journal, 162, 302

Benjamin, R. A., Churchwell, E., Babler, B. L., Bania, T. M., Clemens, D. P., Cohen, M., Dickey, J. M., Indebetouw, R., Jackson, J. M., Kobulnicky, H. A., Lazarian, A., Marston, A. P., Mathis, J. S., Meade, M. R., Seager, S., Stolovy, S. R., Watson, C., Whitney, B. A., Wolff, M. J., & Wolfire, M. G. 2003, Publications of the Astronomical Society of the Pacific, 115, 953

Bennett, M. & Bovy, J. 2019, Monthly Notices of the Royal Astronomy Society, 482, 1417

Binney, J. & Merrifield, M. 1998, Galactic Astronomy

Blanton, M. R., Bershady, M. A., Abolfathi, B., Albareti, F. D., Allende Prieto, C., Almeida, A., Alonso-García, J., Anders, F., Anderson, S. F., Andrews, B., & et al. 2017, The Astronomical Journal, 154, 28

Bowen, I. S. & Vaughan, A. H., J. 1973, Applied Optics, 12, 1430

Bragaglia, A., Sestito, P., Villanova, S., Carretta, E., Randich, S., & Tosi, M. 2008, Astronomy and Astrophysics, 480, 79

Burton, W. B. 1976, The Annual Review of Astronomy and Astrophysics, 14, 275

Cantat-Gaudin, T. & Anders, F. 2020, Astronomy and Astrophysics, 633, A99

Cantat-Gaudin, T., Anders, F., Castro-Ginard, A., Jordi, C., Romero-Gómez, M., Soubiran, C., Casamiquela, L., Tarricq, Y., Moitinho, A., Vallenari, A., Bragaglia, A., Krone-Martins, A., & Kounkel, M. 2020, Astronomy and Astrophysics, 640, A1

Cantat-Gaudin, T., Jordi, C., Vallenari, A., Bragaglia, A., Balaguer-Núñez, L., Soubiran, C., Bossini, D., Moitinho, A., Castro-Ginard, A., Krone-Martins, A., Casamiquela, L., Sordo, R., & Carrera, R. 2018, Astronomy and Astrophysics, 618, A93

Carrera, R. & Pancino, E. 2011, Astronomy and Astrophysics, 535, A30

Casali, G., Magrini, L., Tognelli, E., Jackson, R., Jeffries, R. D., Lagarde, N., Tautvaišienė, G., Masseron, T., Degl'Innocenti, S., Prada Moroni, P. G., Kordopatis, G., Pancino, E., Randich, S., Feltzing, S., Sahlholdt, C., Spina, L., Friel, E., Roccatagliata, V., Sanna, N., Bragaglia, A., Drazdauskas, A., Mikolaitis, Š., Minkevičiūtė, R., Stonkutė, E., Chorniy, Y., Bagdonas, V., Jimenez-Esteban, F., Martell, S., Van der Swaelmen, M., Gilmore, G., Vallenari, A., Bensby, T., Koposov, S. E., Korn, A., Worley, C., Smiljanic, R., Bergemann, M., Carraro, G., Damiani, F., Prisinzano, L.,

Bonito, R., Franciosini, E., Gonneau, A., Hourihane, A., Jofre, P., Lewis, J., Morbidelli, L., Sacco, G., Sousa, S. G., Zaggia, S., Lanzafame, A. C., Heiter, U., Frasca, A., & Bayo, A. 2019, Astronomy and Astrophysics, 629, A62

Casali, G., Spina, L., Magrini, L., Karakas, A. I., Kobayashi, C., Casey, A. R., Feltzing, S., Van der Swaelmen, M., Tsantaki, M., Jofré, P., Bragaglia, A., Feuillet, D., Bensby, T., Biazzo, K., Gonneau, A., Tautvaišienė, G., Baratella, M., Roccatagliata, V., Pancino, E., Sousa, S., Adibekyan, V., Martell, S., Bayo, A., Jackson, R. J., Jeffries, R. D., Gilmore, G., Randich, S., Alfaro, E., Koposov, S. E., Korn, A. J., Recio-Blanco, A., Smiljanic, R., Franciosini, E., Hourihane, A., Monaco, L., Morbidelli, L., Sacco, G., Worley, C., & Zaggia, S. 2020, Astronomy and Astrophysics, 639, A127

Casamiquela, L., Blanco-Cuaresma, S., Carrera, R., Balaguer-Núñez, L., Jordi, C., Anders, F., Chiappini, C., Carbajo-Hijarrubia, J., Aguado, D. S., del Pino, A., Díaz-Pérez, L., Gallart, C., & Pancino, E. 2019, Monthly Notices of the Royal Astronomy Society, 490, 1821

Casamiquela, L., Carrera, R., Blanco-Cuaresma, S., Jordi, C., Balaguer-Núñez, L., Pancino, E., Anders, F., Chiappini, C., Díaz-Pérez, L., Aguado, D. S., Aparicio, A., Garcia-Dias, R., Heiter, U., Martínez-Vázquez, C. E., Murabito, S., & del Pino, A. 2017, Monthly Notices of the Royal Astronomy Society, 470, 4363

Chiappini, C. 2009, in IAU Symposium, Vol. 254, The Galaxy Disk in Cosmological Context, ed. J. Andersen, Nordströara, B. m, & J. Bland -Hawthorn, 191–196

Cunha, K., Frinchaboy, P. M., Souto, D., Thompson, B., Zasowski, G., Allende Prieto, C., Carrera, R., Chiappini, C., Donor, J., García-Hernández, A., García Pérez, A. E., Hayden, M. R., Holtzman, J., Jackson, K. M., Johnson, J. A., Majewski, S. R., Mészáros, S., Meyer, B., Nidever, D. L., O'Connell, J., Schiavon, R. P., Schultheis, M., Shetrone, M., Simmons, A., Smith, V. V., & Zamora, O. 2016a, Astronomische Nachrichten, 337, 922

Cunha, K., Frinchaboy, P. M., Souto, D., Thompson, B., Zasowski, G., Allende Prieto, C., Carrera, R., Chiappini, C., Donor, J., García-Hernández, D. A., García Pérez, A. E., Hayden, M. R., Holtzman, J., Jackson, K. M., Johnson, J. A., Majewski, S. R., Mészáros, S., Meyer, B., Nidever, D. L., O'Connell, J., Schiavon, R. P., Schultheis, M., Shetrone, M., Simmons, A., Smith, V. V., & et al. 2016b, Astronomische Nachrichten, 337, 922

Cunha, K., Smith, V. V., Hasselquist, S., Souto, D., Shetrone, M. D., Allende Prieto, C., Bizyaev, D., Frinchaboy, P., García-Hernández, D. A., Holtzman, J., Johnson, J. A., Jőnsson, H., Majewski, S. R., Mészáros, S., Nidever, D., Pinsonneault, M., Schiavon, R. P., Sobeck, J., Skrutskie, M. F., Zamora, O., Zasowski, G., & Fernández-Trincado, J. G. 2017, The Astrophysical Journal, 844, 145

Cutri, R. M., Skrutskie, M. F., van Dyk, S., Beichman, C. A., Carpenter, J. M., Chester, T., Cambresy, L., Evans, T., Fowler, J., Gizis, J., Howard, E., Huchra, J., Jarrett, T.,

Kopan, E. L., Kirkpatrick, J. D., Light, R. M., Marsh, K. A., McCallon, H., Schneider, S., Stiening, R., Sykes, M., Weinberg, M., Wheaton, W. A., Wheelock, S., & Zacarias, N. 2003, 2MASS All Sky Catalog of point sources.

Donor, J., Frinchaboy, P. M., Cunha, K., O'Connell, J. E., Allende Prieto, C., Almeida, A., Anders, F., Beaton, R., Bizyaev, D., Brownstein, J. R., Carrera, R., Chiappini, C., Cohen, R., García-Hernández, D. A., Geisler, D., Hasselquist, S., Jönsson, H., Lane, R. R., Majewski, S. R., Minniti, D., Bidin, C. M., Pan, K., Roman-Lopes, A., Sobeck, J. S., & Zasowski, G. 2020, The Astronomical Journal, 159, 199

Donor, J., Frinchaboy, P. M., Cunha, K., Thompson, B., O'Connell, J., Zasowski, G., Jackson, K. M., Meyer McGrath, B., Almeida, A., Bizyaev, D., Carrera, R., García-Hernández, D. A., Nitschelm, C., Pan, K., & Zamora, O. 2018, The Astronomical Journal, 156, 142

Drimmel, R. & Poggio, E. 2018, Research Notes of the American Astronomical Society, 2, 210

Eisenstein, D. J., Weinberg, D. H., Agol, E., Aihara, H., Allende Prieto, C., Anderson, S. F., Arns, J. A., Aubourg, É., Bailey, S., Balbinot, E., Barkhouser, R., Beers, T. C., Berlind, A. A., Bickerton, S. J., Bizyaev, D., Blanton, M. R., Bochanski, J. J., Bolton, A. S., Bosman, C. T., Bovy, J., Brandt, W. N., Breslauer, B., Brewington, H. J., Brinkmann, J., Brown, P. J., Brownstein, J. R., Burger, D., Busca, N. G., Campbell, H., Cargile, P. A., Carithers, W. C., Carlberg, J. K., Carr, M. A., Chang, L., Chen, Y., Chiappini, C., Comparat, J., Connolly, N., Cortes, M., Croft, R. A. C., Cunha, K., da Costa, L. N., Davenport, J. R. A., Dawson, K., De Lee, N., Porto de Mello, G. F., de Simoni, F., Dean, J., Dhital, S., Ealet, A., Ebelke, G. L., Edmondson, E. M., Eiting, J. M., Escoffier, S., Esposito, M., Evans, M. L., Fan, X., Femenía Castellá, B., Dutra Ferreira, L., Fitzgerald, G., Fleming, S. W., Font-Ribera, A., Ford, E. B., Frinchaboy, P. M., García Pérez, A. E., Gaudi, B. S., Ge, J., Ghezzi, L., Gillespie, B. A., Gilmore, G., Girardi, L., Gott, J. R., Gould, A., Grebel, E. K., Gunn, J. E., Hamilton, J.-C., Harding, P., Harris, D. W., Hawley, S. L., Hearty, F. R., Hennawi, J. F., González Hernández, J. I., Ho, S., Hogg, D. W., Holtzman, J. A., Honscheid, K., Inada, N., Ivans, I. I., Jiang, L., Jiang, P., Johnson, J. A., Jordan, C., Jordan, W. P., Kauffmann, G., Kazin, E., Kirkby, D., Klaene, M. A., Knapp, G. R., Kneib, J.-P., Kochanek, C. S., Koesterke, L., Kollmeier, J. A., Kron, R. G., Lampeitl, H., Lang, D., Lawler, J. E., Le Goff, J.-M., Lee, B. L., Lee, Y. S., Leisenring, J. M., Lin, Y.-T., Liu, J., Long, D. C., Loomis, C. P., Lucatello, S., Lundgren, B., Lupton, R. H., Ma, B., Ma, Z., MacDonald, N., Mack, C., Mahadevan, S., Maia, M. A. G., Majewski, S. R., Makler, M., Malanushenko, E., Malanushenko, V., Mandelbaum, R., Maraston, C., Margala, D., Maseman, P., Masters, K. L., McBride, C. K., McDonald, P., McGreer, I. D., McMahon, R. G., Mena Requejo, O., Ménard, B., Miralda-Escudé, J., Morrison, H. L., Mullally, F., Muna, D., Murayama, H., Myers, A. D., Naugle, T., Neto, A. F., Nguyen, D. C., Nichol, R. C., Nidever, D. L., O'Connell, R. W., Ogando, R. L. C., Olmstead, M. D., Oravetz, D. J., Padmanabhan, N., Paegert, M., Palanque-Delabrouille, N., Pan, K., Pandey, P., Parejko, J. K., Pâris, I., Pellegrini, P., Pepper, J.,

Percival, W. J., Petitjean, P., Pfaffenberger, R., Pforr, J., Phleps, S., Pichon, C., Pieri, M. M., Prada, F., Price-Whelan, A. M., Raddick, M. J., Ramos, B. H. F., Reid, I. N., Reyle, C., Rich, J., Richards, G. T., Rieke, G. H., Rieke, M. J., Rix, H.-W., Robin, A. C., Rocha-Pinto, H. J., Rockosi, C. M., Roe, N. A., Rollinde, E., Ross, A. J., Ross, N. P., Rossetto, B., Sánchez, A. G., Santiago, B., Sayres, C., Schiavon, R., Schlegel, D. J., Schlesinger, K. J., Schmidt, S. J., Schneider, D. P., Sellgren, K., Shelden, A., Sheldon, E., Shetrone, M., Shu, Y., Silverman, J. D., Simmerer, J., Simmons, A. E., Sivarani, T., Skrutskie, M. F., Slosar, A., Smee, S., Smith, V. V., Snedden, S. A., Stassun, K. G., Steele, O., Steinmetz, M., Stockett, M. H., Stollberg, T., Strauss, M. A., Szalay, A. S., Tanaka, M., Thakar, A. R., Thomas, D., Tinker, J. L., Tofflemire, B. M., Tojeiro, R., Tremonti, C. A., Vargas Magaña, M., Verde, L., Vogt, N. P., Wake, D. A., Wan, X., Wang, J., Weaver, B. A., White, M., White, S. D. M., Wilson, J. C., Wisniewski, J. P., Wood-Vasey, W. M., Yanny, B., Yasuda, N., Yèche, C., York, D. G., Young, E., Zasowski, G., Zehavi, I., & Zhao, B. 2011, The Astronomical Journal, 142, 72

Foreman-Mackey, D., Hogg, D. W., Lang, D., & Goodman, J. 2013, Publications of the Astronomical Society of the Pacific, 125, 306

Friel, E. D., Jacobson, H. R., & Pilachowski, C. A. 2010, The Astronomical Journal, 139, 1942

Frinchaboy, P., Zasowski, G., Jackson, K., Johnson, J. A., Majewski, S. R., Shetrone, M., Rocha, A., & SDSS-III Collaboration. 2010, in JENAM 2010, Joint European and National Astronomy Meeting, 136

Frinchaboy, P. M. & Majewski, S. R. 2008, The Astronomical Journal, 136, 118

Frinchaboy, P. M., Thompson, B., Jackson, K. M., O'Connell, J., Meyer, B., Zasowski, G., Majewski, S. R., Chojnowksi, S. D., Johnson, J. A., Allende Prieto, C., Beers, T. C., Bizyaev, D., Brewington, H., Cunha, K., Ebelke, G., García Pérez, A. E., Hearty, F. R., Holtzman, J., Kinemuchi, K., Malanushenko, E., Malanushenko, V., Marchante, M., Mészáros, S., Muna, D., Nidever, D. L., Oravetz, D., Pan, K., Schiavon, R. P., Schneider, D. P., Shetrone, M., Simmons, A., Snedden, S., Smith, V. V., & Wilson, J. C. 2013, The Astrophysical Journal Letters, 777, L1

Fu, X., Bragaglia, A., Liu, C., Zhang, H., Xu, Y., Wang, K., Zhang, Z.-Y., Zhong, J., Chang, J., Li, L., Chen, L., Chen, Y., Wang, F., Gjergo, E., Wang, C., Yue, N., & Zhang, X. 2022, arXiv e-prints, arXiv:2207.09121

Gaia Collaboration, Brown, A. G. A., Vallenari, A., Prusti, T., de Bruijne, J. H. J., Babusiaux, C., Biermann, M., Creevey, O. L., Evans, D. W., Eyer, L., & et al. 2021, Astronomy and Astrophysics, 649, A1

Gaia Collaboration, Prusti, T., de Bruijne, J. H. J., Brown, A. G. A., Vallenari, A., Babusiaux, C., Bailer-Jones, C. A. L., Bastian, U., Biermann, M., Evans, D. W., & et al. 2016, Astronomy and Astrophysics, 595, A1

García Pérez, A. E., Allende Prieto, C., Holtzman, J. A., Shetrone, M., Mészáros, S., Bizyaev, D., Carrera, R., Cunha, K., García-Hernández, D. A., Johnson, J. A., Majewski, S. R., Nidever, D. L., Schiavon, R. P., Shane, N., Smith, V. V., Sobeck, J., Troup, N., Zamora, O., Weinberg, D. H., Bovy, J., Eisenstein, D. J., Feuillet, D., Frinchaboy, P. M., Hayden, M. R., Hearty, F. R., Nguyen, D. C., O'Connell, R. W., Pinsonneault, M. H., Wilson, J. C., & Zasowski, G. 2016, The Astronomical Journal, 151, 144

Gilmore, G., Randich, S., Asplund, M., Binney, J., Bonifacio, P., Drew, J., Feltzing, S., Ferguson, A., Jeffries, R., Micela, G., Negueruela, I., Prusti, T., Rix, H. W., Vallenari, A., Alfaro, E., Allende-Prieto, C., Babusiaux, C., Bensby, T., Blomme, R., Bragaglia, A., Flaccomio, E., François, P., Irwin, M., Koposov, S., Korn, A., Lanzafame, A., Pancino, E., Paunzen, E., Recio-Blanco, A., Sacco, G., Smiljanic, R., Van Eck, S., Walton, N., Aden, D., Aerts, C., Affer, L., Alcala, J. M., Altavilla, G., Alves, J., Antoja, T., Arenou, F., Argiroffi, C., Asensio Ramos, A., Bailer-Jones, C., Balaguer-Nunez, L., Bayo, A., Barbuy, B., Barisevicius, G., Barrado y Navascues, D., Battistini, C., Bellas Velidis, I., Bellazzini, M., Belokurov, V., Bergemann, M., Bertelli, G., Biazzo, K., Bienayme, O., Bland-Hawthorn, J., Boeche, C., Bonito, S., Boudreault, S., Bouvier, J., Brandao, I., Brown, A., de Bruijne, J., Burleigh, M., Caballero, J., Caffau, E., Calura, F., Capuzzo-Dolcetta, R., Caramazza, M., Carraro, G., Casagrande, L., Casewell, S., Chapman, S., Chiappini, C., Chorniy, Y., Christlieb, N., Cignoni, M., Cocozza, G., Colless, M., Collet, R., Collins, M., Correnti, M., Covino, E., Crnojevic, D., Cropper, M., Cunha, M., Damiani, F., David, M., Delgado, A., Duffau, S., Edvardsson, B., Eldridge, J., Enke, H., Eriksson, K., Evans, N. W., Eyer, L., Famaey, B., Fellhauer, M., Ferreras, I., Figueras, F., Fiorentino, G., Flynn, C., Folha, D., Franciosini, E., Frasca, A., Freeman, K., Fremat, Y., Friel, E., Gaensicke, B., Gameiro, J., Garzon, F., Geier, S., Geisler, D., Gerhard, O., Gibson, B., Gomboc, A., Gomez, A., Gonzalez-Fernandez, C., Gonzalez Hernandez, J., Gosset, E., Grebel, E., Greimel, R., Groenewegen, M., Grundahl, F., Guarcello, M., Gustafsson, B., Hadrava, P., Hatzidimitriou, D., Hambly, N., Hammersley, P., Hansen, C., Haywood, M., Heber, U., Heiter, U., Held, E., Helmi, A., Hensler, G., Herrero, A., Hill, V., Hodgkin, S., Huelamo, N., Huxor, A., Ibata, R., Jackson, R., de Jong, R., Jonker, P., Jordan, S., Jordi, C., Jorissen, A., Katz, D., Kawata, D., Keller, S., Kharchenko, N., Klement, R., Klutsch, A., Knude, J., Koch, A., Kochukhov, O., Kontizas, M., Koubsky, P., Lallement, R., de Laverny, P., van Leeuwen, F., Lemasle, B., Lewis, G., Lind, K., Lindstrom, H. P. E., Lobel, A., Lopez Santiago, J., Lucas, P., Ludwig, H., Lueftinger, T., Magrini, L., Maiz Apellaniz, J., Maldonado, J., Marconi, G., Marino, A., Martayan, C., Martinez-Valpuesta, I., Matijevic, G., McMahon, R., Messina, S., Meyer, M., Miglio, A., Mikolaitis, S., Minchev, I., Minniti, D., Moitinho, A., Momany, Y., Monaco, L., Montalto, M., Monteiro, M. J., Monier, R., Montes, D., Mora, A., Moraux, E., Morel, T., Mowlavi, N., Mucciarelli, A., Munari, U., Napiwotzki, R., Nardetto, N., Naylor, T., Naze, Y., Nelemans, G., Okamoto, S., Ortolani, S., Pace, G., Palla, F., Palous, J., Parker, R., Penarrubia, J., Pillitteri, I., Piotto, G., Posbic, H., Prisinzano, L., Puzeras, E., Quirrenbach, A., Ragaini, S., Read, J., Read, M., Reyle, C., De Ridder, J., Robichon, N., Robin, A., Roeser, S., Romano, D., Royer, F., Ruchti, G., Ruzicka, A., Ryan, S., Ryde, N., Santos, N., Sanz Forcada, J., Sarro Baro, L. M., Sbordone, L., Schilbach,

E., Schmeja, S., Schnurr, O., Schoenrich, R., Scholz, R. D., Seabroke, G., Sharma, S., De Silva, G., Smith, M., Solano, E., Sordo, R., Soubiran, C., Sousa, S., Spagna, A., Steffen, M., Steinmetz, M., Stelzer, B., Stempels, E., Tabernero, H., Tautvaisiene, G., Thevenin, F., Torra, J., Tosi, M., Tolstoy, E., Turon, C., Walker, M., Wambsganss, J., Worley, C., Venn, K., Vink, J., Wyse, R., Zaggia, S., Zeilinger, W., Zoccali, M., Zorec, J., Zucker, D., Zwitter, T., & Gaia-ESO Survey Team. 2012, The Messenger, 147, 25

Gravity Collaboration, Abuter, R., Amorim, A., Anugu, N., Bauböck, M., Benisty, M., Berger, J. P., Blind, N., Bonnet, H., Brandner, W., Buron, A., Collin, C., Chapron, F., Clénet, Y., Coudé Du Foresto, V., de Zeeuw, P. T., Deen, C., Delplancke-Ströbele, F., Dembet, R., Dexter, J., Duvert, G., Eckart, A., Eisenhauer, F., Finger, G., Förster Schreiber, N. M., Fédou, P., Garcia, P., Garcia Lopez, R., Gao, F., Gendron, E., Genzel, R., Gillessen, S., Gordo, P., Habibi, M., Haubois, X., Haug, M., Haußmann, F., Henning, T., Hippler, S., Horrobin, M., Hubert, Z., Hubin, N., Jimenez Rosales, A., Jochum, L., Jocou, K., Kaufer, A., Kellner, S., Kendrew, S., Kervella, P., Kok, Y., Kulas, M., Lacour, S., Lapeyrère, V., Lazareff, B., Le Bouquin, J. B., Léna, P., Lippa, M., Lenzen, R., Mérand, A., Müler, E., Neumann, U., Ott, T., Palanca, L., Paumard, T., Pasquini, L., Perraut, K., Perrin, G., Pfuhl, O., Plewa, P. M., Rabien, S., Ramírez, A., Ramos, J., Rau, C., Rodríguez-Coira, G., Rohloff, R. R., Rousset, G., Sanchez-Bermudez, J., Scheithauer, S., Schöller, M., Schuler, N., Spyromilio, J., Straub, O., Straubmeier, C., Sturm, E., Tacconi, L. J., Tristram, K. R. W., Vincent, F., von Fellenberg, S., Wank, I., Waisberg, I., Widmann, F., Wieprecht, E., Wiest, M., Wiezorrek, E., Woillez, J., Yazici, S., Ziegler, D., & Zins, G. 2018, Astronomy and Astrophysics, 615, L15

Gravity Collaboration, Abuter, R., Amorim, A., Bauböck, M., Berger, J. P., Bonnet, H., Brandner, W., Clénet, Y., Davies, R., de Zeeuw, P. T., Dexter, J., Dallilar, Y., Drescher, A., Eckart, A., Eisenhauer, F., Förster Schreiber, N. M., Garcia, P., Gao, F., Gendron, E., Genzel, R., Gillessen, S., Habibi, M., Haubois, X., Heißel, G., Henning, T., Hippler, S., Horrobin, M., Jiménez-Rosales, A., Jochum, L., Jocou, L., Kaufer, A., Kervella, P., Lacour, S., Lapeyrère, V., Le Bouquin, J. B., Léna, P., Lutz, D., Nowak, M., Ott, T., Paumard, T., Perraut, K., Perrin, G., Pfuhl, O., Rabien, S., Rodríguez-Coira, G., Shangguan, J., Shimizu, T., Scheithauer, S., Stadler, J., Straub, O., Straubmeier, C., Sturm, E., Tacconi, L. J., Vincent, F., von Fellenberg, S., Waisberg, I., Widmann, F., Wieprecht, E., Wiezorrek, E., Woillez, J., Yazici, S., Young, A., & Zins, G. 2021, Astronomy and Astrophysics, 647, A59

Gunn, J. E., Siegmund, W. A., Mannery, E. J., Owen, R. E., Hull, C. L., Leger, R. F., Carey, L. N., Knapp, G. R., York, D. G., Boroski, W. N., Kent, S. M., Lupton, R. H., Rockosi, C. M., Evans, M. L., Waddell, P., Anderson, J. E., Annis, J., Barentine, J. C., Bartoszek, L. M., Bastian, S., Bracker, S. B., Brewington, H. J., Briegel, C. I., Brinkmann, J., Brown, Y. J., Carr, M. A., Czarapata, P. C., Drennan, C. C., Dombeck, T., Federwitz, G. R., Gillespie, B. A., Gonzales, C., Hansen, S. U., Harvanek, M., Hayes, J., Jordan, W., Kinney, E., Klaene, M., Kleinman, S. J., Kron, R. G., Kresinski, J., Lee, G., Limmongkol, S., Lindenmeyer, C. W., Long, D. C., Loomis, C. L., McGehee, P. M., Mantsch, P. M., Neilsen, Jr., E. H., Neswold, R. M.,

Newman, P. R., Nitta, A., Peoples, Jr., J., Pier, J. R., Prieto, P. S., Prosapio, A., Rivetta, C., Schneider, D. P., Snedden, S., & Wang, S.-i. 2006, The Astronomical Journal, 131, 2332

Harris, W. E. 1996, The Astronomical Journal, 112, 1487

Holtzman, J. A., Hasselquist, S., Shetrone, M., Cunha, K., Allende Prieto, C., Anguiano, B., Bizyaev, D., Bovy, J., Casey, A., Edvardsson, B., Johnson, J. A., Jönsson, H., Meszaros, S., Smith, V. V., Sobeck, J., Zamora, O., Chojnowski, S. D., Fernandez-Trincado, J., Garcia-Hernandez, D. A., Majewski, S. R., Pinsonneault, M., Souto, D., Stringfellow, G. S., Tayar, J., Troup, N., & Zasowski, G. 2018, The Astronomical Journal, 156, 125

Holtzman, J. A., Shetrone, M., Johnson, J. A., Allende Prieto, C., Anders, F., Andrews, B., Beers, T. C., Bizyaev, D., Blanton, M. R., Bovy, J., Carrera, R., Chojnowski, S. D., Cunha, K., Eisenstein, D. J., Feuillet, D., Frinchaboy, P. M., Galbraith-Frew, J., García Pérez, A. E., García-Hernández, D. A., Hasselquist, S., Hayden, M. R., Hearty, F. R., Ivans, I., Majewski, S. R., Martell, S., Meszaros, S., Muna, D., Nidever, D., Nguyen, D. C., O'Connell, R. W., Pan, K., Pinsonneault, M., Robin, A. C., Schiavon, R. P., Shane, N., Sobeck, J., Smith, V. V., Troup, N., Weinberg, D. H., Wilson, J. C., Wood-Vasey, W. M., Zamora, O., & Zasowski, G. 2015, The Astronomical Journal, 150, 148

Hubeny, I., Allende Prieto, C., Osorio, Y., & Lanz, T. 2021, arXiv e-prints, arXiv:2104.02829

Hubeny, I. & Lanz, T. 2017, arXiv e-prints, arXiv:1706.01859

Jackson, R. J., Jeffries, R. D., Wright, N. J., Randich, S., Sacco, G., Bragaglia, A., Hourihane, A., Tognelli, E., Degl'Innocenti, S., Moroni, P. G. P., Gilmore, G., Bensby, T., Pancino, E., Smiljanic, R., Bergemann, M., Carraro, G., Franciosini, E., Gonneau, A., Jofré, P., Lewis, J., Magrini, L., Morbidelli, L., Prisinzano, L., Worley, C., Zaggia, S., Tautvaišiene, G., Albarrán, M. L. G., Montes, D., & Jiménez-Esteban, F. 2021, Monthly Notices of the Royal Astronomy Society

Jahandar, F., Venn, K. A., Shetrone, M. D., Irwin, M., Bovy, J., Sakari, C. M., Kielty, C. L., Digby, R. A. R., & Frinchaboy, P. M. 2017, Monthly Notices of the Royal Astronomy Society, 470, 4782

Janes, K. A. 1979, Astrophysical Journal Supplement, 39, 135

Jönsson, H., Holtzman, J. A., Allende Prieto, C., Cunha, K., García-Hernández, D. A., Hasselquist, S., Masseron, T., Osorio, Y., Shetrone, M., Smith, V., Stringfellow, G. S., Bizyaev, D., Edvardsson, B., Majewski, S. R., Mészáros, S., Souto, D., Zamora, O., Beaton, R. L., Bovy, J., Donor, J., Pinsonneault, M. H., Poovelil, V. J., & Sobeck, J. 2020, The Astronomical Journal, 160, 120

Kobayashi, C., Leung, S.-C., & Nomoto, K. 2020, The Astrophysical Journal, 895, 138

Kounkel, M., Covey, K., Suárez, G., Román-Zúñiga, C., Hernandez, J., Stassun, K., Jaehnig, K. O., Feigelson, E. D., Peña Ramírez, K., Roman-Lopes, A., Da Rio, N., Stringfellow, G. S., Kim, J. S., Borissova, J., Fernández-Trincado, J. G., Burgasser, A., García-Hernández, D. A., Zamora, O., Pan, K., & Nitschelm, C. 2018, The Astronomical Journal, 156, 84

Luo, A. L., Zhao, Y.-H., Zhao, G., Deng, L.-C., Liu, X.-W., Jing, Y.-P., Wang, G., Zhang, H.-T., Shi, J.-R., Cui, X.-Q., Chu, Y.-Q., Li, G.-P., Bai, Z.-R., Wu, Y., Cai, Y., Cao, S.-Y., Cao, Z.-H., Carlin, J. L., Chen, H.-Y., Chen, J.-J., Chen, K.-X., Chen, L., Chen, X.-L., Chen, X.-Y., Chen, Y., Christlieb, N., Chu, J.-R., Cui, C.-Z., Dong, Y.-Q., Du, B., Fan, D.-W., Feng, L., Fu, J.-N., Gao, P., Gong, X.-F., Gu, B.-Z., Guo, Y.-X., Han, Z.-W., He, B.-L., Hou, J.-L., Hou, Y.-H., Hou, W., Hu, H.-Z., Hu, N.-S., Hu, Z.-W., Huo, Z.-Y., Jia, L., Jiang, F.-H., Jiang, X., Jiang, Z.-B., Jin, G., Kong, X., Kong, X., Lei, Y.-J., Li, A.-H., Li, C.-H., Li, G.-W., Li, H.-N., Li, J., Li, Q., Li, S., Li, S.-S., Li, X.-N., Li, Y., Li, Y.-B., Li, Y.-P., Liang, Y., Lin, C.-C., Liu, C., Liu, G.-R., Liu, G.-Q., Liu, Z.-G., Lu, W.-Z., Luo, Y., Mao, Y.-D., Newberg, H., Ni, J.-J., Qi, Z.-X., Qi, Y.-J., Shen, S.-Y., Shi, H.-M., Song, J., Song, Y.-H., Su, D.-Q., Su, H.-J., Tang, Z.-H., Tao, Q.-S., Tian, Y., Wang, D., Wang, D.-Q., Wang, F.-F., Wang, G.-M., Wang, H., Wang, H.-C., Wang, J., Wang, J.-N., Wang, J.-L., Wang, J.-P., Wang, J.-X., Wang, L., Wang, M.-X., Wang, S.-G., Wang, S.-Q., Wang, X., Wang, Y.-N., Wang, Y., Wang, Y.-F., Wang, Y.-F., Wei, P., Wei, M.-Z., Wu, H., Wu, K.-F., Wu, X.-B., Wu, Y.-Z., Xing, X.-Z., Xu, L.-Z., Xu, X.-Q., Xu, Y., Yan, T.-S., Yang, D.-H., Yang, H.-F., Yang, H.-Q., Yang, M., Yao, Z.-Q., Yu, Y., Yuan, H., Yuan, H.-B., Yuan, H.-L., Yuan, W.-M., Zhai, C., Zhang, E.-P., Zhang, H.-W., Zhang, J.-N., Zhang, L.-P., Zhang, W., Zhang, Y., Zhang, Y.-X., Zhang, Z.-C., Zhao, M., Zhou, F., Zhou, X., Zhu, J., Zhu, Y.-T., Zou, S.-C., & Zuo, F. 2015, Research in Astronomy and Astrophysics, 15, 1095

Magrini, L., Randich, S., Kordopatis, G., Prantzos, N., Romano, D., Chieffi, A., Limongi, M., François, P., Pancino, E., Friel, E., Bragaglia, A., Tautvaišienė, G., Spina, L., Overbeek, J., Cantat-Gaudin, T., Donati, P., Vallenari, A., Sordo, R., Jiménez-Esteban, F. M., Tang, B., Drazdauskas, A., Sousa, S., Duffau, S., Jofré, P., Gilmore, G., Feltzing, S., Alfaro, E., Bensby, T., Flaccomio, E., Koposov, S., Lanzafame, A., Smiljanic, R., Bayo, A., Carraro, G., Casey, A. R., Costado, M. T., Damiani, F., Franciosini, E., Hourihane, A., Lardo, C., Lewis, J., Monaco, L., Morbidelli, L., Sacco, G., Sbordone, L., Worley, C. C., & Zaggia, S. 2017, Astronomy and Astrophysics, 603, A2

Majewski, S. R., Schiavon, R. P., Frinchaboy, P. M., Allende Prieto, C., Barkhouser, R., Bizyaev, D., Blank, B., Brunner, S., Burton, A., Carrera, R., Chojnowski, S. D., Cunha, K., Epstein, C., Fitzgerald, G., García Pérez, A. E., Hearty, F. R., Henderson, C., Holtzman, J. A., Johnson, J. A., Lam, C. R., Lawler, J. E., Maseman, P., Mészáros, S., Nelson, M., Nguyen, D. C., Nidever, D. L., Pinsonneault, M., Shetrone, M., Smee, S., Smith, V. V., Stolberg, T., Skrutskie, M. F., Walker, E., Wilson, J. C., Zasowski, G., Anders, F., Basu, S., Beland, S., Blanton, M. R., Bovy, J., Brownstein, J. R., Carlberg, J., Chaplin, W., Chiappini, C., Eisenstein, D. J., Elsworth, Y., Feuillet, D., Fleming, S. W., Galbraith-Frew, J., García, R. A., García-Hernández, D. A., Gillespie, B. A., Girardi, L., Gunn, J. E., Hasselquist, S., Hayden, M. R., Hekker, S., Ivans, I.,

Kinemuchi, K., Klaene, M., Mahadevan, S., Mathur, S., Mosser, B., Muna, D., Munn, J. A., Nichol, R. C., O'Connell, R. W., Parejko, J. K., Robin, A. C., Rocha-Pinto, H., Schultheis, M., Serenelli, A. M., Shane, N., Silva Aguirre, V., Sobeck, J. S., Thompson, B., Troup, N. W., Weinberg, D. H., & Zamora, O. 2017, The Astronomical Journal, 154, 94

Majewski, S. R., Zasowski, G., & Nidever, D. L. 2011, The Astrophysical Journal, 739, 25

Martell, S. L., Sharma, S., Buder, S., Duong, L., Schlesinger, K. J., Simpson, J., Lind, K., Ness, M., Marshall, J. P., Asplund, M., Bland-Hawthorn, J., Casey, A. R., De Silva, G., Freeman, K. C., Kos, J., Lin, J., Zucker, D. B., Zwitter, T., Anguiano, B., Bacigalupo, C., Carollo, D., Casagrande, L., Da Costa, G. S., Horner, J., Huber, D., Hyde, E. A., Kafle, P. R., Lewis, G. F., Nataf, D., Navin, C. A., Stello, D., Tinney, C. G., Watson, F. G., & Wittenmyer, R. 2017, Monthly Notices of the Royal Astronomy Society, 465, 3203

Minchev, I., Chiappini, C., & Martig, M. 2013, Astronomy and Astrophysics, 558, A9

—. 2014, Astronomy and Astrophysics, 572, A92

Myers, N., Donor, J., Spoo, T., Frinchaboy, P. M., Cunha, K., Price-Whelan, A. M., Majewski, S. R., Beaton, R. L., Zasowski, G., O'Connell, J., Ray, A. E., Bizyaev, D., Chiappini, C., García-Hernández, D. A., Geisler, D., Jönsson, H., Lane, R. R., Longa-Peña, P., Minchev, I., Minniti, D., Nitschelm, C., & Roman-Lopes, A. 2022, The Astronomical Journal, 164, 85

Netopil, M., Oralhan, İ. A., Çakmak, H., Michel, R., & Karataş, Y. 2022, Monthly Notices of the Royal Astronomy Society, 509, 421

Netopil, M., Paunzen, E., Heiter, U., & Soubiran, C. 2016, Astronomy and Astrophysics, 585, A150

Nidever, D. L., Holtzman, J. A., Allende Prieto, C., Beland, S., Bender, C., Bizyaev, D., Burton, A., Desphande, R., Fleming, S. W., García Pérez, A. E., Hearty, F. R., Majewski, S. R., Mészáros, S., Muna, D., Nguyen, D., Schiavon, R. P., Shetrone, M., Skrutskie, M. F., Sobeck, J. S., & Wilson, J. C. 2015, The Astronomical Journal, 150, 173

O'Connell, J. E. 2017, PhD thesis, Texas Christian University, United States

Olney, R., Kounkel, M., Schillinger, C., Scoggins, M. T., Yin, Y., Howard, E., Covey, K. R., Hutchinson, B., & Stassun, K. G. 2020, The Astronomical Journal, 159, 182

Osorio, Y., Allende Prieto, C., Hubeny, I., Mészáros, S., & Shetrone, M. 2020, Astronomy and Astrophysics, 637, A80

Piotto, G. 2009, in The Ages of Stars, ed. E. E. Mamajek, D. R. Soderblom, & R. F. G. Wyse, Vol. 258, 233–244

Price-Whelan, A. M., Hogg, D. W., Johnston, K. V., Ness, M. K., Rix, H.-W., Beaton, R. L., Brownstein, J. R., García-Hernández, D. A., Hasselquist, S., Hayes, C. R., Lane, R. R., Shetrone, M., Sobeck, J., & Zasowski, G. 2021, The Astrophysical Journal, 910, 17

Ray, A. E., Frinchaboy, P. M., Donor, J., Chojnowski, S. D., & Melendez, M. 2022, The Astronomical Journal, 163, 195

Reddy, A. B. S., Lambert, D. L., & Giridhar, S. 2016, Monthly Notices of the Royal Astronomy Society, 463, 4366

Reid, M. J. & Brunthaler, A. 2004, The Astrophysical Journal, 616, 872

Sakari, C., Venn, K., Arimoto, N., Aoki, W., & Irwin, M. 2011, in American Astronomical Society Meeting Abstracts, Vol. 217, American Astronomical Society Meeting Abstracts #217, 434.48

Sales-Silva, J. V., Daflon, S., Cunha, K., Souto, D., Smith, V. V., Chiappini, C., Donor, J., Frinchaboy, P. M., García-Hernández, D. A., Hayes, C., Majewski, S. R., Masseron, T., Schiavon, R. P., Weinberg, D. H., Beaton, R. L., Fernández-Trincado, J. G., Jönsson, H., Lane, R. R., Minniti, D., Manchado, A., Moni Bidin, C., Nitschelm, C., O'Connell, J., & Villanova, S. 2022, The Astrophysical Journal, 926, 154

Santana, F. A., Beaton, R. L., Covey, K. R., O'Connell, J. E., Longa-Peña, P., Cohen, R., Fernández-Trincado, J. G., Hayes, C. R., Zasowski, G., Sobeck, J. S., Majewski, S. R., Chojnowski, S. D., De Lee, N., Oelkers, R. J., Stringfellow, G. S., Almeida, A., Anguiano, B., Donor, J., Frinchaboy, P. M., Hasselquist, S., Johnson, J. A., Kollmeier, J. A., Nidever, D. L., Price-Whelan, A. M., Rojas-Arriagada, A., Schultheis, M., Shetrone, M., Simon, J. D., Aerts, C., Borissova, J., Drout, M. R., Geisler, D., Law, C. Y., Medina, N., Minniti, D., Monachesi, A., Muñoz, R. R., Poleski, R., Roman-Lopes, A., Schlaufman, K. C., Stutz, A. M., Teske, J., Tkachenko, A., Van Saders, J. L., Weinberger, A. J., & Zoccali, M. 2021, The Astronomical Journal, 162, 303

Seabroke, G. M., Fabricius, C., Teyssier, D., Sartoretti, P., Katz, D., Cropper, M., Antoja, T., Benson, K., Smith, M., Dolding, C., Gosset, E., Panuzzo, P., Thévenin, F., Allende Prieto, C., Blomme, R., Guerrier, A., Huckle, H., Jean-Antoine, A., Haigron, R., Marchal, O., Baker, S., Damerdji, Y., David, M., Frémat, Y., Janßen, K., Jasniewicz, G., Lobel, A., Samaras, N., Plum, G., Soubiran, C., Vanel, O., Zwitter, T., Ajaj, M., Caffau, E., Chemin, L., Royer, F., Brouillet, N., Crifo, F., Guy, L. P., Hambly, N. C., Leclerc, N., Mastrobuono-Battisti, A., & Viala, Y. 2021, Astronomy and Astrophysics, 653, A160

Sestito, P., Bragaglia, A., Randich, S., Pallavicini, R., Andrievsky, S. M., & Korotin, S. A. 2008, Astronomy and Astrophysics, 488, 943

Shetrone, M., Bizyaev, D., Lawler, J. E., Allende Prieto, C., Johnson, J. A., Smith, V. V., Cunha, K., Holtzman, J., García Pérez, A. E., Mészáros, S., Sobeck, J., Zamora, O.,

García-Hernández, D. A., Souto, D., Chojnowski, D., Koesterke, L., Majewski, S., & Zasowski, G. 2015, Astrophysical Journal Supplement, 221, 24

Smith, V. V., Bizyaev, D., Cunha, K., Shetrone, M. D., Souto, D., Allende Prieto, C., Masseron, T., Mészáros, S., Jönsson, H., Hasselquist, S., Osorio, Y., García-Hernández, D. A., Plez, B., Beaton, R. L., Holtzman, J., Majewski, S. R., Stringfellow, G. S., & Sobeck, J. 2021, The Astronomical Journal, 161, 254

Spina, L., Ting, Y. S., De Silva, G. M., Frankel, N., Sharma, S., Cantat-Gaudin, T., Joyce, M., Stello, D., Karakas, A. I., Asplund, M. B., Nordlander, T., Casagrande, L., D'Orazi, V., Casey, A. R., Cottrell, P., Tepper-García, T., Baratella, M., Kos, J., Čotar, K., Bland-Hawthorn, J., Buder, S., Freeman, K. C., Hayden, M. R., Lewis, G. F., Lin, J., Lind, K., Martell, S. L., Schlesinger, K. J., Simpson, J. D., Zucker, D. B., & Zwitter, T. 2021, Monthly Notices of the Royal Astronomy Society, 503, 3279

Spoo, T., Tayar, J., Frinchaboy, P. M., Cunha, K., Myers, N., Donor, J., Majewski, S. R., Bizyaev, D., García-Hernández, D. A., Jönsson, H., Lane, R. R., Pan, K., Longa-Peña, P., & Roman-Lopes, A. 2022, The Astronomical Journal, 163, 229

Vasiliev, E. & Baumgardt, H. 2021, Monthly Notices of the Royal Astronomy Society, 505, 5978

Viscasillas Vázquez, C., Magrini, L., Casali, G., Tautvaišienė, G., Spina, L., Van der Swaelmen, M., Randich, S., Bensby, T., Bragaglia, A., Friel, E., Feltzing, S., Sacco, G. G., Turchi, A., Jiménez-Esteban, F., D'Orazi, V., Delgado-Mena, E., Mikolaitis, Š., Drazdauskas, A., Minkevičiūtė, R., Stonkutė, E., Bagdonas, V., Montes, D., Guiglion, G., Baratella, M., Tabernero, H. M., Gilmore, G., Alfaro, E., Francois, P., Korn, A., Smiljanic, R., Bergemann, M., Franciosini, E., Gonneau, A., Hourihane, A., Worley, C. C., & Zaggia, S. 2022, arXiv e-prints, arXiv:2202.04863

Wagner-Kaiser, R., Sarajedini, A., von Hippel, T., Stenning, D. C., van Dyk, D. A., Jeffery, E., Robinson, E., Stein, N., Anderson, J., & Jefferys, W. H. 2017, Monthly Notices of the Royal Astronomy Society, 468, 1038

Wilson, J. C., Hearty, F. R., Skrutskie, M. F., Majewski, S. R., Holtzman, J. A., Eisenstein, D., Gunn, J., Blank, B., Henderson, C., Smee, S., Nelson, M., Nidever, D., Arns, J., Barkhouser, R., Barr, J., Beland, S., Bershady, M. A., Blanton, M. R., Brunner, S., Burton, A., Carey, L., Carr, M., Colque, J. P., Crane, J., Damke, G. J., Davidson, J. W., J., Dean, J., Di Mille, F., Don, K. W., Ebelke, G., Evans, M., Fitzgerald, G., Gillespie, B., Hall, M., Harding, A., Harding, P., Hammond, R., Hancock, D., Harrison, C., Hope, S., Horne, T., Karakla, J., Lam, C., Leger, F., MacDonald, N., Maseman, P., Matsunari, J., Melton, S., Mitcheltree, T., O'Brien, T., O'Connell, R. W., Patten, A., Richardson, W., Rieke, G., Rieke, M., Roman-Lopes, A., Schiavon, R. P., Sobeck, J. S., Stolberg, T., Stoll, R., Tembe, M., Trujillo, J. D., Uomoto, A., Vernieri, M., Walker, E., Weinberg, D. H., Young, E., Anthony-Brumfield, B., Bizyaev, D., Breslauer, B., De Lee, N., Downey, J., Halverson, S., Huehnerhoff, J., Klaene, M., Leon, E., Long, D., Mahadevan, S., Malanushenko, E., Nguyen, D. C., Owen, R., Sánchez-Gallego,

J. R., Sayres, C., Shane, N., Shectman, S. A., Shetrone, M., Skinner, D., Stauffer, F., & Zhao, B. 2019, Publications of the Astronomical Society of the Pacific, 131, 055001

Wright, E. L., Eisenhardt, P. R. M., Mainzer, A. K., Ressler, M. E., Cutri, R. M., Jarrett, T., Kirkpatrick, J. D., Padgett, D., McMillan, R. S., Skrutskie, M., Stanford, S. A., Cohen, M., Walker, R. G., Mather, J. C., Leisawitz, D., Gautier, III, T. N., McLean, I., Benford, D., Lonsdale, C. J., Blain, A., Mendez, B., Irace, W. R., Duval, V., Liu, F., Royer, D., Heinrichsen, I., Howard, J., Shannon, M., Kendall, M., Walsh, A. L., Larsen, M., Cardon, J. G., Schick, S., Schwalm, M., Abid, M., Fabinsky, B., Naes, L., & Tsai, C.-W. 2010, The Astronomical Journal, 140, 1868

Yong, D., Carney, B. W., & Friel, E. D. 2012, The Astronomical Journal, 144, 95

Zasowski, G., Cohen, R. E., Chojnowski, S. D., Santana, F., Oelkers, R. J., Andrews, B., Beaton, R. L., Bender, C., Bird, J. C., Bovy, J., Carlberg, J. K., Covey, K., Cunha, K., Dell'Agli, F., Fleming, S. W., Frinchaboy, P. M., García-Hernández, D. A., Harding, P., Holtzman, J., Johnson, J. A., Kollmeier, J. A., Majewski, S. R., Mészáros, S., Munn, J., Muñoz, R. R., Ness, M. K., Nidever, D. L., Poleski, R., Román-Zúñiga, C., Shetrone, M., Simon, J. D., Smith, V. V., Sobeck, J. S., Stringfellow, G. S., Szigetiáros, L., Tayar, J., & Troup, N. 2017, The Astronomical Journal, 154, 198

Zasowski, G., Johnson, J. A., Frinchaboy, P. M., Majewski, S. R., Nidever, D. L., Rocha Pinto, H. J., Girardi, L., Andrews, B., Chojnowski, S. D., Cudworth, K. M., Jackson, K., Munn, J., Skrutskie, M. F., Beaton, R. L., Blake, C. H., Covey, K., Deshpande, R., Epstein, C., Fabbian, D., Fleming, S. W., Garcia Hernandez, D. A., Herrero, A., Mahadevan, S., Mészáros, S., Schultheis, M., Sellgren, K., Terrien, R., van Saders, J., Allende Prieto, C., Bizyaev, D., Burton, A., Cunha, K., da Costa, L. N., Hasselquist, S., Hearty, F., Holtzman, J., García Pérez, A. E., Maia, M. A. G., O'Connell, R. W., O'Donnell, C., Pinsonneault, M., Santiago, B. X., Schiavon, R. P., Shetrone, M., Smith, V., & Wilson, J. C. 2013, The Astronomical Journal, 146, 81

Zhang, H., Chen, Y., & Zhao, G. 2021, The Astrophysical Journal, 919, 52

Zhao, G., Zhao, Y.-H., Chu, Y.-Q., Jing, Y.-P., & Deng, L.-C. 2012, Research in Astronomy and Astrophysics, 12, 723

VITA

Personal Background	Natalie Myers Madison, WI Daughter of Robert and Monica Myers
Education	Diploma, Edgewood High School, Madison, WI, 2016 Bachelor of Science, Physics, University of St. Thomas, St. Paul, MN, 2020
Experience	Summer research assistant, University of St. Thomas, St. Paul, MN, 2019 Teaching assistantship, Texas Christian University, Fort Worth, TX, 2020-2021 Research assistantship, Texas Christian University, Fort Worth, TX, 2021-2022
Professional Memberships	American Astronomical Society

ABSTRACT

MEASURING GALACTIC CHEMICAL ABUNDANCE TRENDS IN OPEN AND GLOBULAR CLUSTERS USING SDSS/APOGEE

by Natalie Myers, MS, 2022
Department of Physics and Astronomy
Texas Christian University

Research Advisor: Peter M. Frinchaboy III, Professor of Physics

Star clusters are key tracers for chemical and dynamical evolution in the Milky Way. As such, constructing and analyzing a large, comprehensive, uniform dataset of clusters can provide needed constraints for Galactic dynamic and chemical evolution parameters. The Open Cluster Chemical Abundance and Mapping (OCCAM) survey aims to do just that. This latest contribution to the OCCAM survey presents the analysis of SDSS/APOGEE Data Release 17 (DR17), where we find a sample of 150 open clusters, 94 of which are designated as high-quality. We find the APOGEE DR17-derived [Fe/H] values to be in good agreement with those from previous studies, and by using a subset of the high-quality sample, the Galactic abundance gradients were measured for 15 other elements. In addition to the open cluster sample, we also use the OCCAM pipeline to define membership probabilities for 72 globular clusters to explore their properties in a homogeneous sample.